Universidade
Estadual de Londrina

JOÃO GABRIEL VICENTE

A LINE-OF-SIGHT INTEGRATOR FOR NEARLY ISOTROPIC BIANCHI MODELS

Londrina
2025

JOÃO GABRIEL VICENTE

A LINE-OF-SIGHT INTEGRATOR FOR NEARLY ISOTROPIC BIANCHI MODELS

Dissertação apresentada ao Departamento de Física da Universidade Estadual de Londrina, como requisito parcial à obtenção do título de Mestre. Área de concentração: Física.
Orientador: Prof. Dr. Thiago dos Santos Pereira.

Londrina
2025

Ficha de identificação da obra elaborada pelo autor, através do Programa de Geração Automática do Sistema de Bibliotecas da UEL

Vicente, João Gabriel.
A Line-of-Sight integrator for nearly isotropic Bianchi models / João Gabriel Vicente. - Londrina, 2025.
101 f. : il.

Orientador: Thiago dos Santos Pereira.
Dissertação (Mestrado em Física) - Universidade Estadual de Londrina, Centro de Ciências Exatas, Programa de Pós-Graduação em Física, 2025.
Inclui bibliografia.

1. Cosmologia - Tese. 2. Testes de isotropia - Tese. 3. Modelos de Bianchi - Tese. 4. Radiação Cósmica de Fundo - Tese. I. Pereira, Thiago dos Santos. II. Universidade Estadual de Londrina. Centro de Ciências Exatas. Programa de Pós-Graduação em Física. III. Título.

CDU 53

JOÃO GABRIEL VICENTE

A LINE-OF-SIGHT INTEGRATOR FOR NEARLY ISOTROPIC BIANCHI MODELS

Dissertação apresentada ao Departamento de Física da Universidade Estadual de Londrina, como requisito parcial à obtenção do título de Mestre. Área de concentração: Física.

BANCA EXAMINADORA

Orientador: Prof. Dr. Thiago dos Santos Pereira
Universidade Estadual de Londrina

Prof. Dr. Sandro Dias Pinto Vitenti
Universidade Estadual de Londrina

Dr. Felipe Tovar Falciano
Centro Brasileiro de Pesquisas Físicas

Londrina, _____ de ____________ de 2025.

Agradecimentos

Sou grato à minha família por todo o apoio durante estes dois anos. Em especial, ao meu pai, pela companhia, e aos meus tios, pelo suporte durante meu primeiro ano de mestrado.

Em seguida, agradeço às minhas amigas mais próximas, Alana e Barbara, por me manterem são durante esse processo. Agradeço à Alana por todas as tardes de quarta-feira em que tomamos café juntos na UEL e à Barbara pela incrível hospitalidade e pelas roupas que ela me presenteou todas as vezes em que dormi na sua casa.

Agradeço ao meu orientador, Thiago Pereira, por todas as conversas e discussões que tivemos acerca do projeto. Muitos dos meus interesses de pesquisa e meu perfil como cientista foram herdados dele. Também gostaria de agradecer ao nosso colaborador, Cyril Pitrou, pela ajuda na construção dos programas e na caça aos bugs. *Merci beaucoup*, Cyril!

Agradeço também aos meus colegas de sala e aos meus colegas de grupo (e de viagem!).

Por fim, agradeço o suporte financeiro da CAPES e ao programa de pós-graduação em Física da UEL pela ajuda de custos na minha viagem a Trieste.

A distância mais curta entre dois pontos pode ser a linha reta, mas é nos caminhos curvos que se encontram as melhores coisas.

— Lygia Fagundes Telles, *Ciranda de Pedra*

Resumo

VICENTE, João Gabriel. **Integrador na linha de visada para modelos de Bianchi quase isotrópicos**. 2025. 101 f. Dissertação (Mestrado em Física) – Universidade Estadual de Londrina, 2025.

Nas últimas décadas, a hipótese de isotropia cósmica vem sendo sujeita a escrutínio. Dados observacionais favorecem-na, mas pequenos graus de anisotropias intrínsecas da geometria ainda não podem ser descartados. Conforme os experimentos se tornam mais precisos, novas ferramentas se fazem necessárias para esse tipo de análise. Neste contexto, introduzimos dois programas, `AniCLASS` e `AniLoS`, que calculam, utilizando método da integral na Linha-de-visada, os efeitos deixados na Radiação Cósmica de Fundo por uma classe de modelos cosmológicos homogeneos. O software é baseado na correspondência entre modelos de Bianchi e perturbações homogêneas da métrica FLRW. Neste trabalho, apresentamos um resumo sobre todos os métodos nos quais os programas são baseados: a física da teoria de perturbações em FLRW, a dinâmica de modelos de Bianchi linearizados e suas conexões com perturbações em FLRW, e a evolução dos fótons da Radiação Cósmica de Fundo. Também analisamos suas estruturas e produtos. As ferramentas aqui propostas pavimentam a busca pela geometria do universo a partir de dados da próxima geração de sondas da Radiação Cósmica de Fundo.

Palavras–Chave: Cosmologia, Testes de isotropia, Modelos de Bianchi, Radiação Cósmica de Fundo, Equação de Boltzmann, Integral na linha-de-visada.

Abstract

VICENTE, João Gabriel. **A Line-of-Sight integrator for nearly isotropic Bianchi models.** 2025. 101 p. Dissertation (Master's in Physics) – State University of Londrina, 2025.

The cosmic isotropy hypothesis has been subjected to scrutiny in the past few decades. Observational data favors it, but small levels of intrinsic geometric anisotropies cannot be ruled out yet. As probes become more precise, new tools are required to perform this analysis. In this context, we introduce two programs, `AniCLASS` and `AniLoS`, that compute the effects of a class of homogeneous cosmological models in the Cosmic Microwave Background through the Line-of-sight integral approach. The software is based on the matching of Bianchi models with homogeneous FLRW metric perturbations. In this work, we review all the methods on which the programs are based: the physics of perturbation theory in FLRW, the dynamics of linearized Bianchi models and their connection to FLRW perturbations, and the evolution of the Cosmic Microwave Background photons. We also provide a summary of their structure and outputs. The tools proposed here pave the way for exploring the universe's geometry using data from the next generation of Cosmic Microwave Background probes.

Key–words: Cosmology, Isotropy testing, Bianchi models, Cosmic Microwave Background (CMB), Boltzmann equation, Line-of-sight integral.

Contents

Introduction

The Cosmological Principle is a cornerstone of physical cosmology. The idea that the universe is spatially homogeneous and isotropic at large scales was first motivated by our intuition, but new data has progressively opened the doors to observational inquiries. In the past few decades, Cosmic Microwave Background (CMB) probes, especially the Planck satellite [1], have provided the greatest observational support for the Cosmological Principle. The tiny CMB temperature fluctuations are expected in an almost FLRW universe and, even if the CMB alone cannot prove the Cosmological Principle, it is highly consistent with it [2, 3].

Despite this success, models where the Cosmological Principle is relaxed have been long studied by the community [4]. A class of these models, the Bianchi models, relaxes the isotropy condition. Bianchi models are the simplest generalization of FLRW models, which they contain as limit [5]. WMAP and Planck temperature data allowed for a thorough statistical analysis of some of these models [6, 7, 8, 9], mostly in favor of FLRW over Bianchi – although small levels of intrinsic anisotropy cannot be ruled out. Moreover, Big Bang Nucleosynthesis has also provided tight constraints in the levels of anisotropy [10].

However, current unresolved problems, like the Hubble tension and the kinematical dipole tension [11, 12, 13], together with recent indications that the universe might not be flat [14] motivate the search for simple solutions in the context of geometrical extensions. Nonetheless, all the previous statistical developments cannot be neglected. Any study of Bianchi cosmologies must take into account the small levels of anisotropy required by the CMB. This simplifies the task since it enables the anisotropies to be treated perturbatively, which, in turn, introduces a link between Bianchi models and the theory of linear perturbations in FLRW [15]. This is achieved by matching the shear and other anisotropic-related quantities to the usual metric perturbations in a suitably defined homogeneous limit [16].

This work builds on top of all previous developments to provide additional tools for the investigation of Bianchi cosmologies. We develop two software applications, `AniCLASS` and `AniLoS` (Anisotropic Line-of-Sight integrator), that compute the large-scale effects of the Bianchi models with FLRW limit in the CMB (in the context of small anisotropies), making use of standard perturbation theory. These fast and reliable algorithms calculate the deterministic patterns that Bianchi cosmologies imprint in the CMB multipoles.

These programs compute the temperature and polarization multipoles by solving the Boltzmann equation using the Line-of-sight integral approach, introduced by U. Seljak and M. Zaldarriaga [17]. `AniCLASS` is a modification of `CLASS`, which means it is extremely efficient. `AniLoS` is an easy-to-modify `Python` package, so any user can modify it to perform any calculation in the context of Bianchi cosmologies.

This dissertation has two main goals: introducing the equations that are numerically implemented and discussing the programs and their outputs. The theoretical framework consists of Bianchi models, CMB physics, and the initial conditions. Although this dissertation mainly focuses on the theoretical basis upon which the programs are built, the majority of effort in this project was dedicated to the development of the software in tasks such as: efficiency tests, comparisons between both programs, figuring out what were the bottlenecks and how to improve them, documenting, rewriting sections of code for readability, and debugging.

In chapter 1, we dedicate some words to exploring the physical intuition behind the concept of anisotropic expansion by examining how it affects the movement of massive particles. We will revisit the issue of anisotropies in chapter 4, where we will formally introduce Bianchi models. In this chapter, we will illustrate the idea of matching Bianchi models with perturbations in FLRW, but we will not rigorously derive this result. In chapters 2 and 3, we discuss the perturbed FLRW model and CMB physics. In particular, the evolution equations for the CMB temperature fluctuations will be derived in a flat universe, for simplicity. Throughout chapters 3 and 4, we will introduce the initial conditions we employ in our implementation, focusing on the neutrino isocurvature velocity initial condition. Finally, in chapter 5, we present some details and the outputs of `AniLoS` and `AniCLASS`. We conclude with some perspectives and open issues.

In this work, we use the natural unit system, where $c = 1$. We represent tensors as $T_{\mu\nu}$ and, occasionally, we use boldface $\boldsymbol{T}$ in situations where the index notation would be confusing — sets of vectors $\{\boldsymbol{\xi}_a\}$, for example. Greek indices run from 0 to 3 and Latin indices run from 1 to 3.

1 COSMIC EXPANSION AND SHEAR

This work is concerned with a class of spatially homogeneous cosmological models that present anisotropic expansion, known as Bianchi models. In simple terms, anisotropic expansion means that different directions in space expand at different rates. Although this concept is intuitively easy to grasp, the details around it are not. The mathematics necessary to construct Bianchi models is involved, obscuring the physical interpretation of the shear tensor, the object that describes anisotropy. As such, instead of jumping directly into the theoretical formalism of Bianchi models, exploring the concept of anisotropic expansion in a simpler approach is beneficial.

To this end, in this chapter, we will explore the concepts of *cosmic expansion* and *cosmic shear* in the context of congruences of timelike geodesics. In section 1.1 we cover the kinematic properties of timelike geodesics, and in section 1.2 we briefly introduce some concepts in General Relativity. We follow the notation of [18] to derive the kinematic quantities and their evolution equations.

1.1 KINEMATICS

Without non-gravitational forces, all observers freely fall. A family of free-falling observers is defined as a congruence of timelike curves[1]. We will restrict ourselves to the case where these curves are geodesics. Each curve is the world line of an observer, so each event in spacetime lies in a single world line. The geodesics are parametrized by the observers' proper time τ. The family's four-velocity field u^μ, normalized as $u^\mu u_\mu = -1$, is tangent to the congruence.

In general, different observers do not share the same proper time. Hence, it is not possible (in general) to find a coordinate system where the time coordinate is the proper time of all observers in a region. Then, instead of introducing a coordinate system, we project vectors into parallel and orthogonal components to the geodesic flow. The perpendicular projector is defined by the four-velocity field as $-u^\mu u_\nu$. The orthogonal projector is thus $\gamma^\mu{}_\nu \equiv \delta^\mu{}_\nu + u^\mu u_\nu$.

The tensor $\nabla_\mu u_\nu$ (∇_μ is the covariant derivative compatible with the metric $g_{\mu\nu}$) is particularly important, as it carries the kinematic properties of the world lines. The assumption that the observers move in geodesics implies that one of the kinematic parameters, the four-acceleration $a_\mu \equiv u^\alpha \nabla_\alpha u_\mu$, is zero. The tensor $\nabla_\mu u_\nu$ can be decomposed into symmetric and antisymmetric parts:

$$\nabla_\mu u_\nu = \theta_{\mu\nu} + \omega_{\mu\nu}, \tag{1.1}$$

---

[1] A congruence of curves is a set of curves such that each point in the manifold is in the image set of a single curve. For a formal definition, see [19]

$\theta_{\mu\nu} \equiv \nabla_{(\mu}u_{\nu)}$, and $\omega_{\mu\nu} \equiv \nabla_{[\mu}u_{\nu]}$. The symmetric part can be further written as

$$\theta_{\mu\nu} = \frac{\theta^{\lambda}{}_{\lambda}}{3}\gamma_{\mu\nu} + \theta_{\langle\mu\nu\rangle}, \tag{1.2}$$

where

$$S_{\langle\mu\nu\rangle} \equiv S_{(\mu\nu)} - \frac{S^{\lambda}{}_{\lambda}}{3}\gamma_{\mu\nu} \tag{1.3}$$

is the symmetric trace-free (STF) part of the tensor $S_{\mu\nu}$.

The trace $\theta \equiv \theta^{\lambda}{}_{\lambda} = \nabla^{\lambda}u_{\lambda}$ measures the divergence of the world lines. Physically, it describes an isotropic volume expansion/contraction of the congruence. The STF part, $\sigma_{\mu\nu} \equiv \theta_{\langle\mu\nu\rangle}$, is the shear. It measures volume-preserving deformations in the form enclosed by nearby world lines. Finally, the antisymmetric part $\omega_{\mu\nu}$ is the vorticity and it describes the rotation of the world lines.

Let us explore the physical meaning of the expansion scalar and the shear tensor. Consider a light source S, at rest with the family u^{μ}, that emits a photon with energy E_s. The photon follows a null geodesic parameterized by an affine parameter λ. The tangent vector to the geodesic is $k^{\mu} = E(u^{\mu} - n^{\mu})$, where $E = -k^{\mu}u_{\mu}$, $u^{\mu}n_{\mu} = 0$, and $n^{\mu}n_{\mu} = 1$. An observer at $\lambda = \lambda_O$ measures the photon blueshifted or redshifted with energy E_O. The redshift is defined as

$$1 + z \equiv \frac{E_S}{E_O}. \tag{1.4}$$

Suppose that the source and the observer are nearby, so the redshift may be expressed as

$$z(\lambda, n^{\mu}) = \left.\frac{\mathrm{d}z}{\mathrm{d}\lambda}\right|_0 (\lambda - \lambda_O), \tag{1.5}$$

where $\mathrm{d}/\mathrm{d}\lambda = k^{\mu}\nabla_{\mu}$. Using (1.1) and (1.4) leads to

$$z(\lambda, n^{\mu}) = \left.\left(\frac{\theta}{3} + n^{\mu}n^{\nu}\sigma_{\mu\nu}\right)\right|_0 E_O(\lambda - \lambda_O). \tag{1.6}$$

This has a multipolar structure in n^{μ}, where the scalar θ is the monopole and the shear is the quadrupole coefficient [20]. In a universe where $\theta > 0$ and there is no shear, all sources at the same distance to the observer have the same redshift; the volume enclosed by these sources around the observer expands isotropically. In a universe where only $\sigma_{\mu\nu}$ is non-zero, different sources at the same distance have different redshifts (see Figure 1). Moreover, the sky-average redshift is zero, meaning that the volume enclosed by the sources is preserved, although its shape is deformed.

To visualize the deformation better, let us explore a qualitative example. Take the distance $E_O(\lambda - \lambda_O) = 1$ and consider z small, such that the radial velocity v of the objects is $v = z$. Introducing a coordinate system where the shear tensor has components $\mathrm{diag}(0, 1, 0, -1)$, we

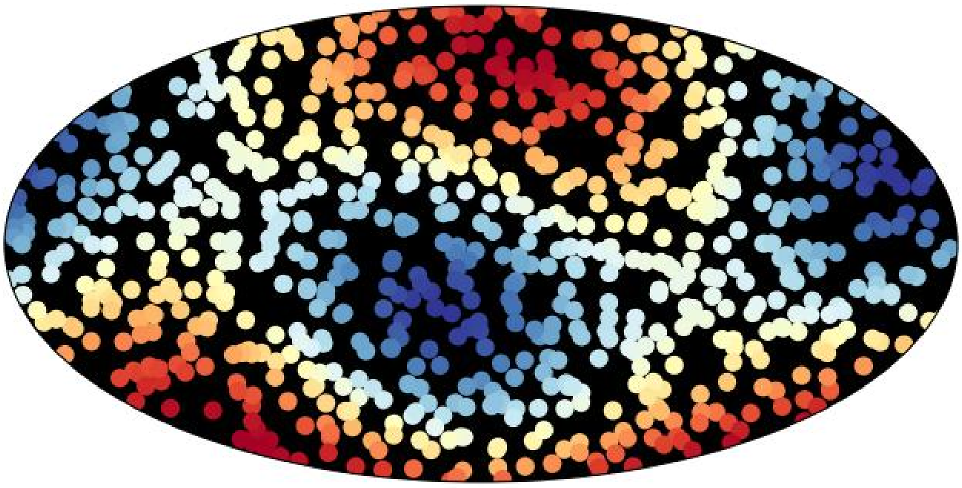

Figure 1: Sources in a universe with shear. Blue and red dots represent blueshifted and redshifted light respectively.

have

$$v(\vartheta, \varphi) = \sin\vartheta \cos\varphi - \cos\vartheta. \tag{1.7}$$

For a small amount of time δt, the distance changes[2] $d(\vartheta, \varphi) = 1 + v(\vartheta, \varphi)\delta t$. This change in distance induces a deformation in the initial spherical volume, as shown in Figure 2. We see that there is an expansion in the x-direction, which is compensated by a contraction in the z-direction.

From now on, we assume that vorticity is zero, as the data suggests this [21]. The kinematic tensor reduces to

$$\nabla_\mu u_\nu = \theta_{\mu\nu} = \frac{\theta}{3}\gamma_{\mu\nu} + \sigma_{\mu\nu}. \tag{1.8}$$

The vanishing of vorticity implies that u^μ is a closed one-form, so it is (locally) an exact one-form [22],

$$\omega_{\mu\nu} = 0 \Rightarrow u_\mu = -(\mathrm{d}t)_\mu. \tag{1.9}$$

The scalar function t is the *cosmic time*. We see that there is a coordinate system where the time component $x^0 = t$ is such that $\mathrm{d}t/\mathrm{d}\tau = 1$, so, if all observers synchronize their clocks in some instant t_0, they will remain synchronized. In other words, the observers share the same proper time if vorticity is zero.

Taking the directional derivative $\mathrm{d}/\mathrm{d}\tau \equiv u^\mu \nabla_\mu$ of equation (1.8) leads to evolution equations for the kinematic quantities

$$\frac{\mathrm{d}\theta}{\mathrm{d}\tau} = -\frac{\theta^2}{3} - 2\sigma^2 - R_{\mu\nu}u^\mu u^\nu, \tag{1.10}$$

$$\frac{\mathrm{d}\sigma_{\mu\nu}}{\mathrm{d}\tau} = -\frac{2}{3}\theta\sigma_{\mu\nu} - \sigma_{\mu\alpha}\sigma^{\alpha}{}_{\nu} + \frac{2}{3}\sigma^2\gamma_{\mu\nu} + R_{\alpha\langle\nu\mu\rangle\beta}u^\alpha u^\beta, \tag{1.11}$$

---

[2] It is important to notice that the shear induces a rotation in each light source but in such a way that the surface they form does not rotate [18].

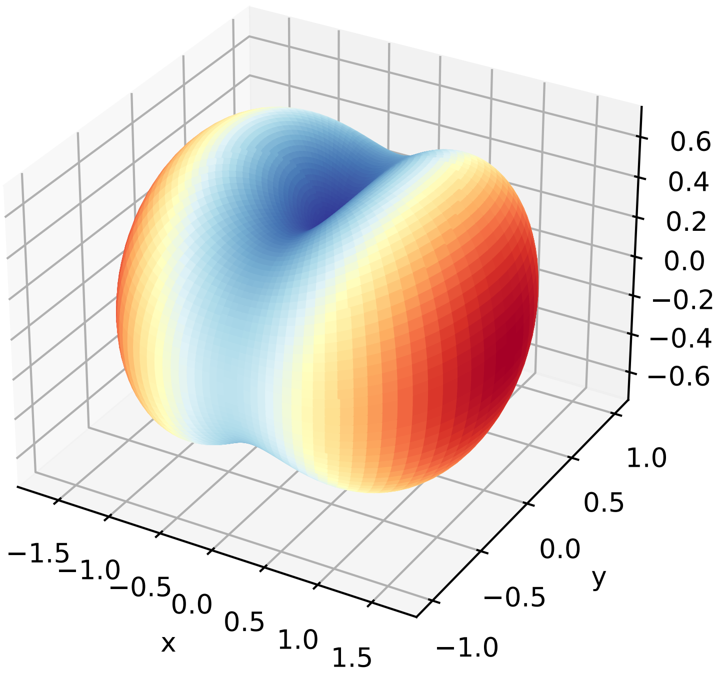

Figure 2: Deformed sphere. Effects are out of proportion for visualization purposes.

where $R_{\mu\nu}$ is the Ricci curvature tensor, $R_{\mu\nu\alpha\beta}$ is the Riemann curvature tensor, and $2\sigma^2 \equiv \sigma_{\mu\nu}\sigma^{\mu\nu}$.

We see that the expansion and the shear depend on the spacetime geometry through the Riemann and Ricci tensors. If the spacetime were flat, the two equations above would be a closed system. But energy is dynamically linked to the spacetime curvature. Therefore, we need to include a theory of gravity to understand how the kinematic parameters evolve.

1.2 DYNAMICS

We assume that the General Theory of Relativity is the correct theory of gravity. The relation between energy, momentum, and curvature is given by Einstein's Field Equation (EFEs)

$$R_{\mu\nu} - \frac{1}{2} g_{\mu\nu} R + g_{\mu\nu}\Lambda = 8\pi G T_{\mu\nu}, \tag{1.12}$$

where R is the Ricci scalar, Λ is the cosmological constant, and $T_{\mu\nu}$ is the energy-momentum tensor.

In the right-hand side of the equation (1.12), we have the energy-momentum tensor, which, for a general fluid, has the form

$$T_{\mu\nu} = \rho u_\mu u_\nu + P\gamma_{\mu\nu} + j_\mu u_\nu + j_\nu u_\mu + \Pi_{\mu\nu}, \tag{1.13}$$

where ρ is de energy density, P is the pressure, j_μ is the momentum flux, and $\Pi_{\mu\nu}$ is the anisotropic stress tensor, all measured by an observer with four-velocity u^μ. The momentum flux and the anisotropic stress tensor do not have components in the u^μ direction, $j_\mu u^\mu = 0$, $\Pi^\mu{}_\nu u^\nu = 0$. Moreover, the trace of $\Pi_{\mu\nu}$ is zero, $\Pi^\mu{}_\mu = 0$.

The energy-momentum tensor is subjected to the energy conservation equation

$$\nabla_\mu T^\mu{}_\nu = 0, \tag{1.14}$$

which leads to the Continuity Equation and the Euler Equation:

$$\frac{\mathrm{d}\rho}{\mathrm{d}\tau} + (\rho + P)\theta + \Pi^{\mu\nu}\sigma_{\mu\nu} + \gamma^\mu{}_\nu \nabla_\mu j^\nu = 0, \tag{1.15}$$

$$\frac{\mathrm{d}j^\mu}{\mathrm{d}\tau} + \frac{4}{3}\theta j^\mu + \gamma^\mu{}_\nu \nabla^\nu P + \gamma^\alpha{}_\beta \nabla_\alpha \Pi^{\beta\mu} + j_\alpha \sigma^{\alpha\mu} = 0. \tag{1.16}$$

The cosmological constant is often described as a fluid. Its energy-momentum tensor is

$$T^\Lambda_{\mu\nu} = \frac{\Lambda}{8\pi G} u_\mu u_\nu - \frac{\Lambda}{8\pi G}\gamma_{\mu\nu}, \tag{1.17}$$

so its energy density is $\Lambda/(8\pi G)$ and its pressure is $P = -\rho$.

Meaningful choices of observers can be made considering the fluid distribution. For example, the family at rest with the fluid will measure no momentum flux. This uniquely defines the four-velocity u^μ by the equation

$$T^\mu{}_\nu u_\mu = -\rho u_\nu. \tag{1.18}$$

Then the energy-momentum tensor is simply

$$T_{\mu\nu} = \rho u_\mu u_\nu + P\gamma_{\mu\nu} + \Pi_{\mu\nu}. \tag{1.19}$$

In this context, the quantities θ and $\sigma_{\mu\nu}$ describe the motion of the fluid content. Any other family of observers will detect a momentum flux, and thus a preferred direction (see Figure 3).

Now, we move to the left-hand side of equation (1.12). The spacetime geometry determines the Ricci curvature tensor. We assume that spacetime can be decomposed into three-dimensional spacelike hypersurfaces. A spacelike hypersurface Σ_t, where t is a function $t : \mathcal{M} \to \mathbb{R}$, is a submanifold defined by the condition $\Sigma_{t_0} = \{p \in \mathcal{M}, t(p) = t_0\}$. The spatial slicing is such that $\Sigma_{t_1} \cap \Sigma_{t_2} = \emptyset$ if $t_1 \neq t_2$ and $\mathcal{M} = \bigcup_{t\in\mathbb{R}} \Sigma_t$.[3]

Since t is constant in each surface, its gradient is orthogonal to the surfaces. Thus, dt generates a congruence of timelike geodesics that fills the spacetime. Hence, we can associate this orthogonal (to the hypersurface) vector field with a family of non-rotating free-falling observers. In this context, the orthogonal projector (to the world lines) $\gamma_{\mu\nu}$ is both the projector

---

[3] For a precise defition see [24].

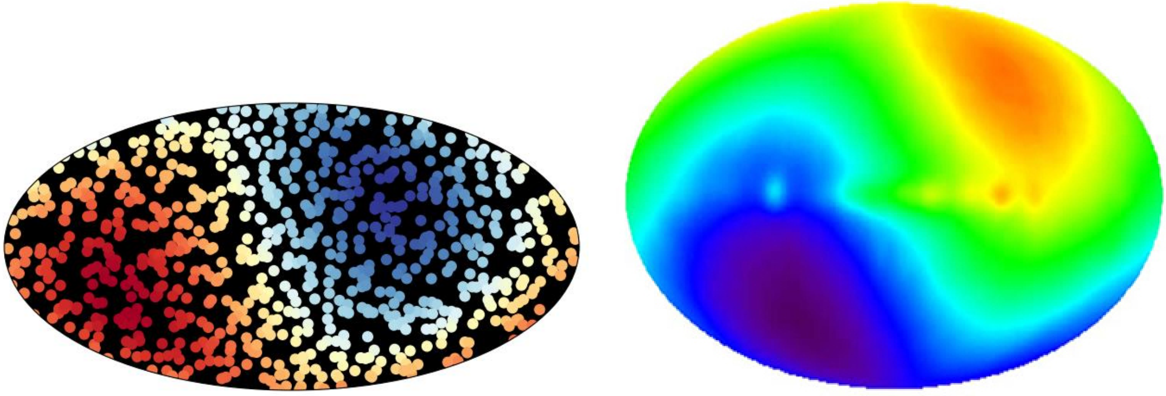
(a) (b)

Figure 3: a) Light sources with $\theta = 0$ and $\sigma_{\mu\nu} = 0$ as measured by a boosted observer. The blueshifted region is the direction of motion of the observer. b) CMB dipole measured by the COBE satellite. It is assumed that the CMB dipole is dominated by the Local Group's peculiar motion. Our velocity with respect to the CMB frame is around 300 km/s in the direction $l = 264°$, $b = 48°$ (l and b being the longitude and latitude in the galactic frame) [23]. **Credits:** NASA.

into the hypersurface and the spatial metric[4].

In these conditions, the spatial metric $\gamma_{\mu\nu}$ defines a covariant derivative compatible with it, D_μ. Associated with it, we can define the Riemann curvature tensor in the spatial section as

$$\mathcal{R}_{\mu\nu\alpha}{}^{\beta}\gamma_\beta{}^\kappa\xi_\kappa \equiv (D_\mu D_\nu - D_\nu D_\mu)\gamma_\alpha{}^\kappa\xi_\kappa, \tag{1.20}$$

where ξ_κ is any co-vector. The definitions of the Ricci tensor and the Ricci scalar follow from this.

Another important tensor in the hypersurfaces is the extrinsic curvature tensor. It accounts for the embedding of the hypersurface in a higher dimensional space. It is defined as

$$\kappa_{\mu\nu} \equiv \frac{1}{2}\mathcal{L}_{\boldsymbol{u}}\gamma_{\mu\nu}, \tag{1.21}$$

where $\mathcal{L}_{\boldsymbol{u}}$ is the Lie derivative[5]; using the fact that u^μ generates geodesics, we find

$$\kappa_{\mu\nu} = \nabla_\mu u_\nu = \theta_{\mu\nu}. \tag{1.22}$$

We now have all the ingredients to compute the EFEs and obtain the evolution of θ and $\sigma_{\mu\nu}$. The EFEs are a system of ten partial differential equations. Analytical solutions do not exist for arbitrary energy distributions and geometries. Thus it is necessary to make simplifying (but physically meaningful) hypotheses. More precisely, we will impose symmetries in the spatial

---

[4] Note that $\gamma_{\mu\nu}$ is defined for any congruence of timelike curves. Thus, generally, $\gamma_{\mu\nu}$ is not a spatial metric because a general congruence is not hypersurface orthogonal.

[5] For a definition, see [25].

sections, which will fix the spatial curvature and reduce some degrees of freedom in the energy-momentum tensor and $\theta_{\mu\nu}$.

2 HOMOGENEOUS AND ISOTROPIC MODELS

In the previous chapter, we introduced the kinematic quantities that give a general description of the motion of fluids and observers in the universe. In this chapter, we will specialize in the case of comoving observers in a spatially homogenous and isotropic universe. We will see that homogeneity and isotropy are related to symmetries in the spatial sections, which will be the basis for the construction of Bianchi models later. In section 2.1, we give an elementary description of the Cosmological Principle. In section 2.2, we formally introduce the concepts of homogeneity and isotropy in terms of isometries. This section is based on [26]. In sections 2.3 and 2.4, we give a brief description of FLRW models and the ΛCDM model.

2.1 Cosmological Principle

We pointed out in the previous chapter that the EFEs are notoriously difficult to solve, so assumptions must be made in order to study the cosmic dynamics. We expect that our location in the universe is not special, a “prejudice” formally named *Copernican Principle*. Furthermore, if all observers in the universe are unable to distinguish directions in space (or, equivalently, if the Copernican Principle is valid and two observers cannot detect differences in directions), then the space is homogeneous and isotropic [3]. This assumption is the *Cosmological Principle*. It states that the universe is, on average, homogeneous and isotropic in sufficiently large volumes. At first, we can understand the Cosmological Principle as a purely philosophical assumption based on our intuition. According to Peebles [27], the discussion about homogeneity and isotropy in the context of physical cosmology goes back to the beginning of the 20th century, and the name “Cosmological Principle” was introduced by Milne as an axiom for the theory.

The precise definitions of homogeneity and isotropy will be explored later. The subtlety here lies in the words “average” and “large volumes”. Homogeneity must be understood in a statistical sense as an average over large-scales, where the deviations from the average are small. This implies the existence of a homogeneity scale, which defines the transition between a clumpy to a smooth universe, and an averaging process over the physical quantities in this scale (see Figure 4). This scale is roughly of order 100 Mpc [28, 29].

Direct measurement of spatial homogeneity is not possible because all cosmological data is in the observer’s past light cone. Instead, what can be observed is isotropy along the light cone, and the best probe for this task is the Cosmic Microwave Background. The tiny fluctuations of about 10μK in the CMB temperature are consistent with the Cosmological Principle and are the most compelling observation in favor of it, but they do not automatically imply spatial isotropy [3]. However, it is important to note that CMB probes isotropy mostly at $z \approx 1000$, and that much less is known about isotropy of the late-time universe [11].

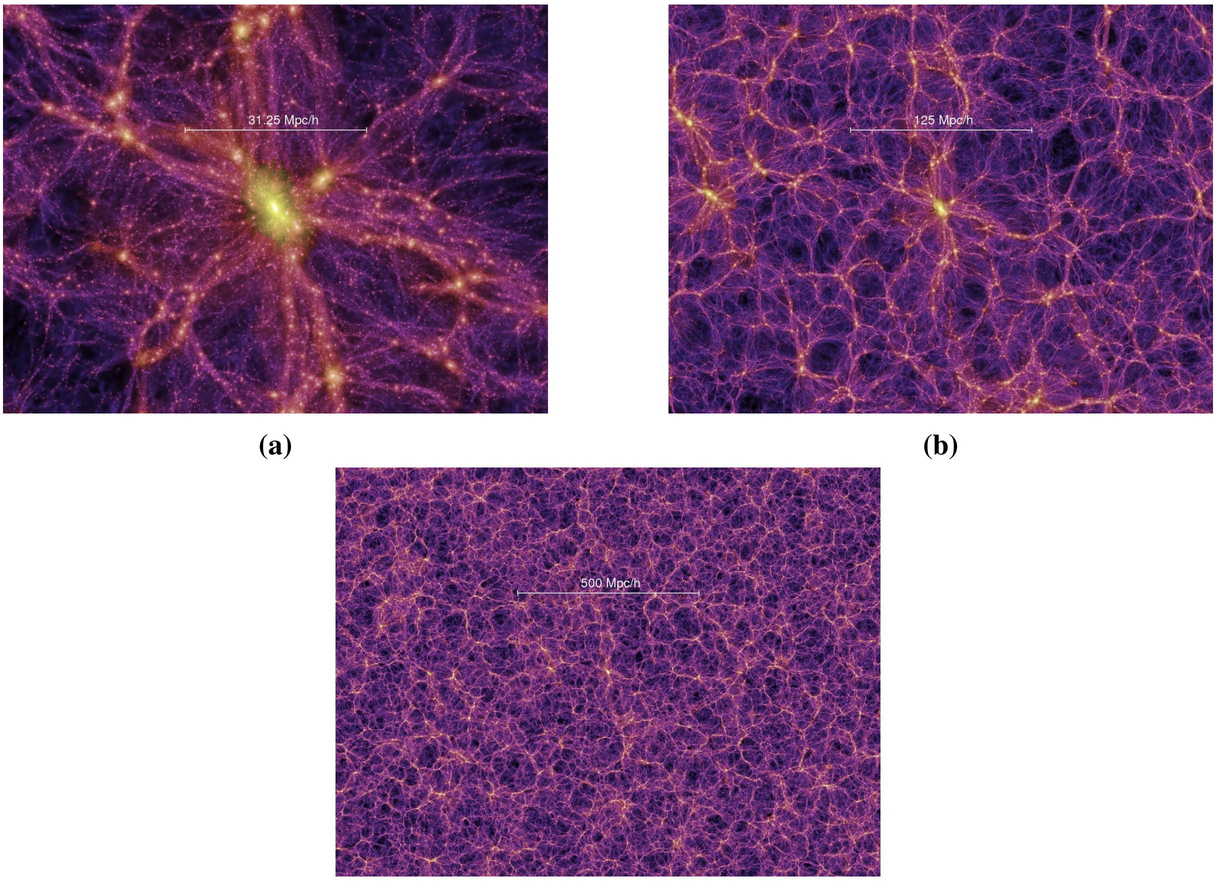

(a) (b) (c)

Figure 4: Distribution of cold dark matter in the universe from an N-body simulation. Each slice is ~ 10 Mpc thick. These figures illustrate the "clumpy-to-homogeneous" transition. **Credits:** Springel et al [30] and Max-Planck-Institute for Astrophysics.

2.2 Homogeneity and isotropy

The concepts of spatial homogeneity and isotropy are fundamentally related to the presence of symmetries. A physical system is homogeneous (isotropic) if it has symmetries by translation (rotation). A symmetry, in the context of general relativity, is defined as a transformation that preserves the metric, that is, an isometry. Isometries are defined by the condition

$$\mathcal{L}_{\boldsymbol{\xi}} g_{\mu\nu} = 0, \tag{2.1}$$

where $\mathcal{L}_{\boldsymbol{\xi}}$ is the Lie derivative, ξ^{μ} is the infinitesimal generator of isometries, called Killing vector, and $g_{\mu\nu}$ is the metric tensor.

From the definition (2.1), we get the Killing equation,

$$\nabla_{\mu}\xi_{\nu} + \nabla_{\nu}\xi_{\mu} = 0, \tag{2.2}$$

where ∇_{μ} is the covariant derivative compatible with $g_{\mu\nu}$. In order to study the symmetries in the manifold, we need to study the Killing vector fields (KVFs). A KVF has the important property that its value in the neighborhood of a point p is completely determined by its value and the value of its first derivative at p. To see this, note that, from the definition of the Riemann tensor,

$$(\nabla_\mu \nabla_\nu - \nabla_\nu \nabla_\mu)\xi_\lambda = R_{\mu\nu\lambda}{}^{\alpha}\xi_\alpha, \tag{2.3}$$

using the cyclic permutation rule of the Riemann tensor [26],

$$R_{\mu\nu\lambda}{}^{\alpha} + R_{\lambda\mu\nu}{}^{\alpha} + R_{\nu\lambda\mu}{}^{\alpha} = 0, \tag{2.4}$$

and the Killing equation, we get

$$\nabla_\mu \nabla_\nu \xi_\lambda = R_{\mu\nu\lambda}{}^{\alpha}\xi_\alpha. \tag{2.5}$$

Hence, the second derivative of ξ_λ linearly depends on ξ_α. Taking the derivative of the equation above results in

$$\nabla_\beta \nabla_\mu \nabla_\nu \xi_\lambda = (\nabla_\beta R_{\mu\nu\lambda}{}^{\alpha})\xi_\alpha + R_{\mu\nu\lambda}{}^{\alpha}\nabla_\beta \xi_\alpha, \tag{2.6}$$

showing that the third derivative of ξ_λ linearly depends on ξ_α and $\nabla_\beta \xi_\alpha$. As such, taking successive derivatives of the equation (2.5) yields higher derivatives of ξ_λ in terms of ξ_α and $\nabla_\beta \xi_\alpha$. Consequently, Taylor expanding ξ_λ at a point q on the neighborhood of the point p, we obtain

$$\xi_\lambda|_q = A_\lambda{}^{\mu}\xi_\mu|_p + B_\lambda{}^{\mu\nu}\nabla_\mu \xi_\nu|_p, \tag{2.7}$$

where $A_\lambda{}^{\mu}$ and $B_\lambda{}^{\mu\nu}$ are the coupling coefficients. Note that they depend on p and q, as different choices of points will lead to different coupling coefficients.

In turn, since a Killing vector computed at q requires 4 values of $\xi_\mu|_p$ and $16 - 10 = 6$ values[6] of $\nabla_\mu \xi_\nu|_p$, they have, at maximum, 10 degrees of freedom. However, if there are Killing vector fields orthogonal to the spatial hypersurfaces, then the metric has no time evolution and the universe is static. Therefore, assuming non-trivial time evolution, $u^\mu \xi_\mu = 0$, where u^μ is the vector field orthogonal to the spatial hypersurface, we get

$$\frac{\mathrm{d}\xi_\mu}{\mathrm{d}\tau} = 0, \tag{2.8}$$

thus reducing the maximum number of independent KVFs from 10 to 6.

The 6 independent KVFs describe the spatial symmetries in the manifold, and the concepts of homogeneity and isotropy are defined in terms of them. A space Σ_t is said *homogeneous* if it is possible to link any two nearby points through an isometry. Fixing a point p, let $\phi_s(p) : \mathbb{R} \to \Sigma_t$, $s \mapsto \phi_s(p)$ be the integral curve of a KVF such that $\phi_0(p) = p$. Introducing a coordinate system x^i in the neighborhood of p (we stress that latin indices run from 1 to 3), we have

$$\xi^i|_p = \left.\frac{\mathrm{d}x^i(\phi_s(p))}{\mathrm{d}s}\right|_0, \tag{2.9}$$

---

[6] The Killing equation places 10 constraints on the derivatives of the KVFs.

such that the coordinates of the point $q = \phi_\epsilon(p)$ are

$$\begin{aligned} x^i(q) &= x^i(p) + \epsilon \left. \frac{\mathrm{d}x^i(\phi_s(p))}{\mathrm{d}s} \right|_0 \\ &= x^i(p) + \epsilon \xi^i|_p. \end{aligned} \tag{2.10}$$

Thus, to connect any arbitrary point q with p, $\xi^i|_p$ must be arbitrary. Therefore, the space is homogeneous if, at each point, there is a set of independent KVFs that can take any value. Since the tangent vector space at each point has dimension 3, these sets contain a maximum of three KVFs. We define translations as the transformations generated by these KVFs, and we label these vectors as "translation vectors". It is important to stress that each point has a different set of translation vectors.

The space Σ_t is said isotropic everywhere, or simply *isotropic*, if there are six independent KVFs at every point. Therefore, it is necessarily homogeneous. Moreover, the three non-translation KVFs at p must vanish at this point, as they are independent of the translation vectors. However, their first derivative cannot be zero at p, otherwise the field is zero everywhere (by equation (2.7)). We define rotations as being the transformations generated by these KVFs, and label them as "rotation vectors". Note that, since $\xi_i|_p = 0$, the isometry generated by this KVF maps p to itself and maps points in the neighborhood of p to other points. To see this, consider nearby points q and q' such that

$$x^i(q') = x^i(q) + \epsilon \xi^i|_q, \tag{2.11}$$

but, from equation (2.7),

$$x^i(q') = x^i(q) + \epsilon B^{ijk} \nabla_j \xi_k|_p, \tag{2.12}$$

where $B^{ijk} = g^{ia} B_a{}^{jk}$.

We now focus on spacetimes with spatial sections that present translation and rotation symmetries. The presence of homogeneity and isotropy sets tight constraints in the geometry and fluid content of these spacetimes. First, the family of observers that detects homogeneity and isotropy (the privileged or special family) must be at rest with the fluid content of the universe. Furthermore, still to maintain isotropy, the anisotropic stress tensor must be zero for these privileged observers, so the energy-momentum tensor must be of the form

$$T_{\mu\nu} = \rho u_\mu u_\nu + P \gamma_{\mu\nu}. \tag{2.13}$$

Secondly, the family of observers that detect homogeneity and isotropy has zero shear, otherwise they would be able to find preferred directions. This means that, from equation (1.8),

$$\kappa_{\mu\nu} = \theta_{\mu\nu} = \frac{\theta}{3} \gamma_{\mu\nu}. \tag{2.14}$$

Hence, the only non-zero kinematic property for these observers is an isotropic expansion/contraction.

Lastly, the existence of six independent KVFs in each hypersurface causes the spatial Riemann curvature tensor to be of form [26]

$$\mathcal{R}_{\mu\nu\alpha\beta} = K(\gamma_{\mu\alpha}\gamma_{\nu\beta} - \gamma_{\mu\beta}\gamma_{\nu\alpha}). \tag{2.15}$$

Spaces where the Riemann curvature tensor satisfies the equation above are called maximally symmetric. They are fully characterized by the curvature constant K and the signature of the metric [26].

2.3 FLRW MODELS

The FLRW (Friedmann - Lemaître - Robertson - Walker) models are cosmological models with maximally symmetric spatial sections and non-trivial time evolution. They are defined by the sign of the curvature constant. To obtain the metric of these spacetimes, we first find the spatial metric.

3-spheres are maximally symmetric spaces with $K > 0$ (closed spaces). These spaces can be treated as spherical hypersurfaces of radius ℓ_c embedded into a four-dimensional Euclidean space. Such hypersurfaces are defined by the equation

$$x^2 + y^2 + z^2 + w^2 = \ell_c^2. \tag{2.16}$$

Because of this constraint, the variable w can be eliminated in favor of x, y, and z. Using spherical coordinates, $x = r\sin\vartheta\cos\varphi$, $y = r\sin\vartheta\cos\varphi$, and $z = r\cos\vartheta$, we can write w in terms of r as

$$w = \pm\sqrt{\ell_c^2 - r^2}, \tag{2.17}$$

and thus the differential of w is

$$\mathrm{d}w = \frac{\mathrm{d}w}{\mathrm{d}r}\mathrm{d}r = -\frac{r}{w}\mathrm{d}r. \tag{2.18}$$

The metric then can be written as

$$\begin{aligned}\mathrm{d}\ell^2 &= \mathrm{d}r^2 + r^2(\mathrm{d}\vartheta^2 + \sin^2\vartheta\mathrm{d}\varphi^2) + \frac{r^2}{\ell_c^2 - r^2}\mathrm{d}r^2 \\ &= \frac{\mathrm{d}r^2}{1 - r^2/\ell_c^2} + r^2(\mathrm{d}\vartheta^2 + \sin^2\vartheta\mathrm{d}\varphi^2).\end{aligned} \tag{2.19}$$

Performing a second change of coordinates $r \to \chi$ such that

$$\frac{\mathrm{d}r^2}{1 - r^2/\ell_c^2} = \mathrm{d}\chi^2$$

results in the metric of the 3-sphere in terms of $(\chi, \vartheta, \varphi)$,

$$\mathrm{d}s^2 = \mathrm{d}\chi^2 + \sin^2\chi \mathrm{d}\Omega^2. \tag{2.20}$$

Analogously, a maximally symmetric space with $K < 0$ can be seen as a hypersurface embedded in the Minkowski space defined by the equation

$$w^2 - x^2 - y^2 - z^2 = \ell_c^2. \tag{2.21}$$

Repeating the same steps performed for the closed case, we find

$$\mathrm{d}s^2 = \frac{\mathrm{d}r^2}{1 + r^2/\ell_c^2} + r^2(\mathrm{d}\theta^2 + \sin^2\theta \mathrm{d}\varphi^2), \tag{2.22}$$

or

$$\mathrm{d}s^2 = \mathrm{d}\chi^2 + \sinh^2\chi \mathrm{d}\Omega^2, \tag{2.23}$$

which is the metric of the 3-pseudo sphere.

Finally, the case $K = 0$ is easily derived in the Euclidean space with metric

$$\mathrm{d}s^2 = \mathrm{d}\chi^2 + \chi^2 \mathrm{d}\Omega^2. \tag{2.24}$$

The metrics (2.20), (2.22), and (2.24) exhaust the possible geometries of three-dimensional maximally symmetric spaces. In the curved cases, ℓ_c is a natural distance scale. Since the Riemann tensor $\mathcal{R}_{ijkl}$ is given by second spatial derivatives of the metric and $\gamma_{\mu\nu}$ is dimensionless, the spatial curvature K must have dimensions of lenght^{-2}, which means that we can rescale the curvature radius such that $K = \pm 1/\ell_c^2$. We further define a normalized spatial curvature $\mathcal{K} \equiv K\ell_c^2$, $\mathcal{K} = \pm 1, 0$.

Now that we have the metric in an arbitrary spatial section Σ_{t_0}, the next step is to find the metric everywhere. Since each point in Σ_{t_0} is in a single timelike geodesic, we can extend the coordinate system chosen in Σ_{t_0} by demanding that all the other points in the same geodesic have the same spatial coordinate. Since $u_\mu = -(\mathrm{d}t)_\mu$ and the clocks of all members of this family are always synchronized, t is a natural choice of time coordinate. In this context, the metric of spacetimes with maximally symmetric spatial sections can be written as

$$\mathrm{d}s^2 = -\mathrm{d}t^2 + a^2(t)(\mathrm{d}\chi^2 + r^2(\chi)\mathrm{d}\Omega^2), \tag{2.25}$$

where

$$r(\chi) = \begin{cases} \ell_c \sinh \chi/\ell_c, & K < 0, \\ \ell_c, & K = 0, \\ \ell_c \sin \chi/\ell_c, & K > 0, \end{cases} \tag{2.26}$$

and a is the scale factor, which accounts for the isotropic expansion/contraction of the worldlines. From the definition of the extrinsic curvature tensor, equation (1.21), and using that, in the coordinate system defined in (2.25), $\gamma_{00} = \gamma_{0i} = 0$ and $\gamma_{ij} = g_{ij}$, we find

$$H \equiv \frac{\theta}{3} = \frac{\dot{a}}{a}, \tag{2.27}$$

where H is the Hubble parameter and

$$\dot{a} \equiv \frac{\mathrm{d}a}{\mathrm{d}t}. \tag{2.28}$$

With the spacetime geometry, we can compute the dynamics in an expanding universe. Calculating the EFEs using the metric above and the perfect fluid energy-momentum tensor (equation (2.13)) yields the Friedmann Equations,

$$H^2 = \frac{8\pi G}{3}\rho - \frac{K_0}{a^2}, \tag{2.29}$$

$$\frac{\ddot{a}}{a} = -\frac{4\pi G}{3}(\rho + 3P), \tag{2.30}$$

where $K_0 = K(t_0)$, $a(t_0) = 1$. Note that, since the curvature radius grows with a, the spatial curvature falls with a^2. Computing the Continuity Equation, equation (1.15), leads to

$$\dot{\rho} + 3H(\rho + P) = 0. \tag{2.31}$$

These equations describe the cosmic dynamics in FLRW models. It is convenient, however, to perform a coordinate transformation from cosmic time t to conformal time η, defined as

$$\eta \equiv \int_0^t a(t')\mathrm{d}t'. \tag{2.32}$$

The metric then reads

$$\mathrm{d}s^2 = a^2(\eta)(-\mathrm{d}\eta^2 + \mathrm{d}\chi^2 + r^2(\chi)\mathrm{d}\Omega^2) \tag{2.33}$$

and the Friedmann and the Continuity Equations become

$$\mathcal{H}^2 = \frac{8\pi G a^2}{3}\rho - K_0, \tag{2.34}$$

$$\frac{a''}{a} = \frac{4\pi G a^2}{3}(\rho - 3P) - K_0, \tag{2.35}$$

$$\rho' = -3\mathcal{H}(\rho + P), \tag{2.36}$$

where the prime denotes a derivative with respect to η and $\mathcal{H} \equiv a'/a$.

The Friedmann Equations can be solved once an equation of state for the pressure in terms of the other variables is introduced. We assume that the fluids are barotropic, in which case the pressure is a linear function of the density, $P = w\rho$. Dust is described by an equation of state $w = 0$, and relativistic particles have $w = 1/3$.

Solving the Continuity Equation using the parametrization above for each fluid yields their evolution in terms of the scale factor. Dust evolves inversely proportional to the volume a^3; relativistic species evolve as $\sim a^{-4}$, where the extra a^{-1} comes from the gravitational shift that expansion induces.

The Friedmann Equations are the basis for the standard model of cosmology, the ΛCDM model. Under this framework, the observed expansion of the universe and the abundance of hydrogen and helium have a simple explanation. However, there are additional hypotheses beyond the Cosmological Principle at the foundations of the ΛCDM model that we will explore in the next section.

2.4 ΛCDM MODEL

The ΛCDM model, also called the concordance model, is the current standard model of cosmology. It assumes the Cosmological Principle, so on large scales the metric is FLRW and the fluids are, on average, perfect. The small deviations from the average are treated perturbatively and their origin is set in the context of inflation theory.

The concordance model is highly successful in explaining the observational data. As we mentioned in the previous section, the expansion of the universe and the abundance of light elements are explained just by assuming an FLRW model and employing general relativity, kinetic theory, and nuclear physics in the early universe. Other observational phenomena, which we will discuss in this section, require additional elements.

Beyond the Cosmological Principle, a fundamental hypothesis of the theory is the existence of *Cold Dark Matter*, the CDM in ΛCDM. The majority of visible matter in the universe is in the form of hydrogen gas. The remaining atoms compose objects like stars, planets, and humans. This visible matter is called baryonic matter[7]. However, there is plenty of evidence spanning several scales for an “invisible” matter that only interacts gravitationally with other species. On the galactic scale, stars in the outskirts of galaxies rotate faster than they should in the presence of the observed baryonic matter. On the galaxy clusters scale, weak lensing missions show that almost all the mass in these objects is invisible. Finally, on the cosmological scale, a non-relativistic species is required to account for structure formation. This invisible, non-relativistic matter is called Cold Dark Matter. Both dark and baryonic matter move at a speed much slower than the speed of light, so they behave like dust and thus have negligible pressure. Together, they constitute the matter content of the universe, with energy density $\rho_m = \rho_{\text{CDM}} + \rho_b$.

Another fundamental hypothesis is the presence of a positive cosmological constant. The motivation for this hypothesis is the accelerated expansion of the universe, detected in the late 20th century from observations of Type Ia Supernovae [31, 32]. The cosmological constant is the Λ in ΛCDM.

---

[7] Note that electrons are included in this category, even though they are leptons.

Besides Type Ia Supernovae, another observational probe for cosmology is the Cosmic Microwave Background. The CMB contains the largest fraction of electromagnetic radiation energy in the universe. Its energy density is related to the CMB temperature T through the equation [33]

$$\rho_\gamma = \frac{8\pi^5}{15} T^4. \tag{2.37}$$

However, the total radiation energy density must also include neutrinos. The neutrino energy density can be calculated from ρ_γ by the equation [34]

$$\rho_\nu = N_{\text{eff}} \times \frac{7}{8} \left(\frac{4}{11} \right)^{4/3} \rho_\gamma, \tag{2.38}$$

where $N_{\text{eff}} = 3.045$ is the effective number of relativistic species. It represents the number of neutrino flavors if the neutrino decoupling from the primordial plasma were instantaneous. In this context, the total energy density of the universe is

$$\rho(a) = \rho_{\text{CDM}}(a_0) \left(\frac{a_0}{a} \right)^3 + \rho_b(a_0) \left(\frac{a_0}{a} \right)^3 + \rho_\gamma(a_0) \left(\frac{a_0}{a} \right)^4 + \rho_\nu(a_0) \left(\frac{a_0}{a} \right)^4 + \rho_\Lambda(a_0). \tag{2.39}$$

Note, however, that instead of working with ρ, it is more convenient to introduce a fractional energy density parameter Ω_i, which describes the proportion of each species to the *critial density* ρ_{cr}, the energy density necessary to make the universe spatially flat,

$$\rho_{cr} \equiv \frac{3H_0^2}{8\pi G}, \tag{2.40}$$

where H_0 is the Hubble parameter today. Thus, the fractional energy density of each species can be defined as

$$\Omega_i \equiv \frac{\rho_i}{\rho_{cr}}. \tag{2.41}$$

We also define a curvature density parameter

$$\Omega_K \equiv -\frac{K}{H_0^2}, \tag{2.42}$$

such that

$$\Omega_{\text{CDM}} + \Omega_b + \Omega_\gamma + \Omega_\nu + \Omega_\Lambda + \Omega_K = 1 \tag{2.43}$$

and equation (2.29) reads

$$H^2 = H_0^2(\Omega + \Omega_K), \tag{2.44}$$

where $\Omega \equiv \sum_i \Omega_i$ is the sum of the fractional energy density of all species.

The last piece of theoretical framework that fundaments the standard model of cosmology is inflation. Cosmic inflation is a theory of initial conditions in which, very early time, the universe passed through an accelerated expansion phase. This theory accounts for the origins of the perturbations in the universe, which seed the CMB and structure formation. According to inflation, these perturbations, originated from quantum fluctuations in the early universe, are a realization of a Gaussian random field. This theory adds two free parameters, $\mathcal{A}_s$, the amplitude of the primordial power spectrum, and n_s, the scalar spectral index [35].

Thus, the theoretical basis for the ΛCDM model introduces some free parameters that need to be constrained from data. From the geometry and energy content of the universe, we have the expansion rate H_0, the curvature parameter Ω_K, and the fractional energy density parameters Ω_i. From inflation, we have $\mathcal{A}_s$ and n_s.[8] Some of the cosmological parameters of the concordance model, as measured by the Planck team, are found in Table 1, based on Tables 2 and 4 from [36].

Parameter	Planck Best fit
Ω_b	0.049
Ω_c	0.26
Ω_Λ	0.69
$\ln(10^{10}\mathcal{A}_s)$	3.0
n_s	0.97
Ω_K	7×10^{-4}
H_0 [km s^{-1} Mpc^{-1}]	68

Table 1: Cosmological parameters obtained by the Planck team [36]. The first six entries in the table are some of the free parameters in the Planck analysis, whereas the Hubble parameter is derived from other parameters.

Despite the great success of the ΛCDM model, there are some open problems that, currently, cannot be addressed under this framework. The most famous one is the Hubble tension, a 5σ difference on the measured value of H_0 from probes in the early (CMB, Planck) and late (Type Ia Supernovae, SH0ES) universe [13, 37]. Simple solutions in the form of extensions of the ΛCDM model are being tested against data. The community searches for this type of solution because, even if the concordance model turns out to be wrong, it is believed that a more refined model will not stray much from it. For instance, exploring the nature of dark energy by evaluating evolving dark energy models — the simplest of these models being a parametrization of the dark energy equation of state using two parameters, $w(z) = w_0 + w_a(1 - a)$ — is one of the priorities of this generation of surveys [38, 39, 40]. In this work, we look for simple geometric extensions of the ΛCDM model. To understand how these modifications generate observational imprints, we must study the CMB. The description of CMB physics in the ΛCDM model is based on perturbations on top of an FLRW background, subjects we cover in the next chapter.

---

[8] Note that other free parameters exist, such as the sum of neutrino masses and the optical depth at reionization.

3 LINE-OF-SIGHT INTEGRATION

Having developed the theory that describes an idealized homogeneous and isotropic universe, we now account for the deviations from this picture. A pure FLRW model cannot describe the large structure of the universe or the anisotropy in the CMB because, as we discussed in previous chapters, the physical universe is only homogeneous and isotropic in large scales. To link it with an FLRW cosmology, we argued that the average metric in scales around $100h^{-1}$ Mpc is that of an FLRW universe. Linear perturbation theory in cosmology accounts for the small deviations from the average that give rise to the CMB and the Large Scale Structure. Light from the Cosmic Microwave Background is subjected to a series of phenomena as it travels through the universe. In particular, the geometry of spacetime can be probed using it, allowing, among other things, for isotropy to be tested in the early universe. Thus, CMB offers a pristine probe for testing intrinsic deviations from isotropy.

In this chapter, we will explore some details of linear perturbation theory and the physics of the CMB. In sections 3.1 – 3.5 we introduce the fundamental concepts of the theory: perturbations in geometry and matter, the gauge problem, the Scalar – Vector – Tensor decomposition of perturbations, the Einstein's Field Equations in synchronous gauge, and the harmonic decomposition of perturbations. In section 3.6 we cover some aspects of CMB theory.

3.1 METRIC PERTURBATIONS

We assume that, in large scales, the difference between the real universe and an FLRW background is small. This is because, as we discussed in the previous chapter, data favors the homogeneity and isotropy hypothesis. Thus, in scales just below the homogeneity scale, it is reasonable to describe the deviations from the average as small perturbations.

Let us express mathematically what we mean by "small difference". Consider two manifolds, $\mathcal{M}_0$ and $\mathcal{M}$. The latter is the physical manifold representing the real universe with metric $g^{(\mathrm{R})}_{\mu\nu}$, and the former is a homogeneous and isotropic universe with metric $\bar{g}_{\mu\nu}$. Saying that the difference between these manifolds is small only makes sense if there is a method to identify points in $\mathcal{M}_0$ with points in $\mathcal{M}$ such that two points in different manifolds are said to be "the same".

One method to achieve this identification is to introduce a diffeomorphism[9] $\phi : \mathcal{M}_0 \to \mathcal{M}$ that maps $p \mapsto \phi(p)$. This allows us to say that p and $\phi(p)$ are "the same" point. In this context, we can "bring" the metric $g^{(\mathrm{R})}_{\mu\nu}$ to the background manifold using the pull-back map[10] ϕ^*, $g_{\mu\nu} \equiv (\phi^* g^{(\mathrm{R})})_{\mu\nu}$. Then the difference in the metric between the pulled-back physical universe

---

[9] Diffeomorphisms are invertible and differentiable maps between manifolds.

[10] The pull-back $\phi^* : T^*_{\phi(p)}\mathcal{N} \to T^*_p\mathcal{M}$ is a map between dual tangent spaces induced by a map $\phi : \mathcal{M} \to \mathcal{N}$. If ϕ is a diffeomorphism between the manifolds, ϕ^* can be extended to act on tensors. For a formal definition of the pull-back and the push-forward maps, see [22].

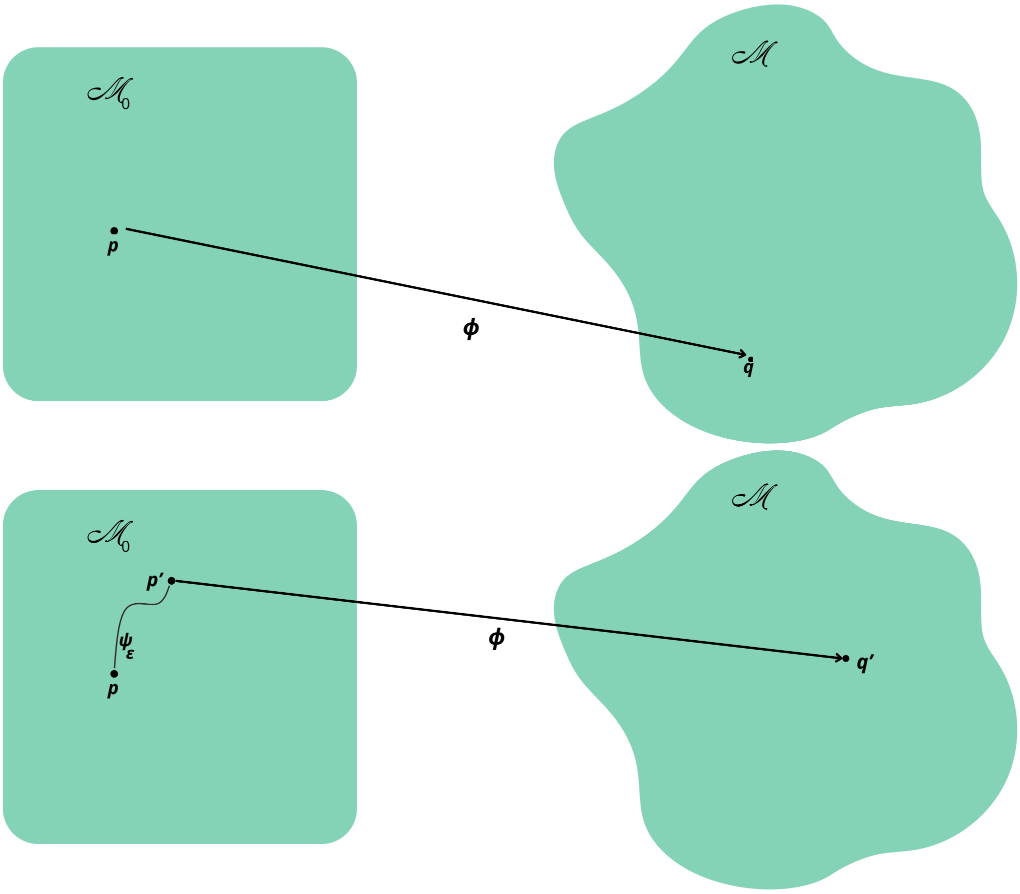

Figure 5: Different ways to identify the background manifold with the physical manifold. In the first image, the point p is connected with q by the diffeomorphism $\phi(p) = q$. In the second image, $q' = (\phi \circ \psi_\epsilon)(p)$.

and the background is

$$\delta g_{\mu\nu} = g_{\mu\nu} - \bar{g}_{\mu\nu}. \tag{3.1}$$

However, many diffeomorphisms relate the two manifolds, so this choice is not unique. Consider a one-parameter group of diffeomorphisms $\psi : \mathcal{M}_0 \times \mathbb{R} \to \mathcal{M}_0$, $(p, s) \mapsto \psi_s(p)$. Taking the parameter s as a small fixed value ϵ, the diffeomorphism $(\phi \circ \psi_\epsilon) : \mathcal{M}_0 \to \mathcal{M}$ will map $p \in \mathcal{M}_0$ into the point $\phi(\psi_\epsilon(p))$, which is different from $\phi(p)$ (see Figure 5). This new map introduces $\tilde{g}_{\mu\nu} = (\psi^*_{-\epsilon} g)_{\mu\nu}$, where $\psi_{-\epsilon} = \psi_\epsilon^{-1}$, such that

$$\delta \tilde{g}_{\mu\nu} = \tilde{g}_{\mu\nu} - \bar{g}_{\mu\nu}. \tag{3.2}$$

If ϵ is small, then the difference between $\tilde{g}_{\mu\nu}$ and $g_{\mu\nu}$ is $\epsilon \mathcal{L}_\zeta \bar{g}_{\mu\nu}$, where ζ^μ is $\mathrm{d}/\mathrm{d}\epsilon$, and hence

$$\delta \tilde{g}_{\mu\nu} = \delta g_{\mu\nu} - \epsilon \mathcal{L}_\zeta \bar{g}_{\mu\nu}. \tag{3.3}$$

The different possible ways to identify the two manifolds is the gauge freedom of the theory. For any tensor of type (n, m), $Q^{\mu_1 \cdots \mu_n}{}_{\nu_1 \ldots \nu_m}$, the difference between its background and physical forms is

$$\delta Q^{\mu_1\dots\mu_n}{}_{\nu_1\dots\nu_m} = Q^{\mu_1\dots\mu_n}{}_{\nu_1\dots\nu_m} - \bar{Q}^{\mu_1\dots\mu_n}{}_{\nu_1\dots\nu_m}. \tag{3.4}$$

Moreover, under a gauge transformation, it changes as

$$\delta\tilde{Q}^{\mu_1\dots\mu_n}{}_{\nu_1\dots\nu_m} = \delta Q^{\mu_1\dots\mu_n}{}_{\nu_1\dots\nu_m} - \epsilon\mathcal{L}_\zeta Q^{\mu_1\dots\mu_n}{}_{\nu_1\dots\nu_m}. \tag{3.5}$$

3.2 SVT DECOMPOSITION

Now that we have defined the meaning of the perturbed metric $g_{\mu\nu}$, we can explore its degrees of freedom. The perturbations can be decomposed into scalar, vector, and tensor parts (irreducible representations of the rotation group in the spatial sections). Setting $\delta g_{\mu\nu} = a^2 h_{\mu\nu}$ and defining $\tilde{\gamma}_{\mu\nu} \equiv a^{-2}\bar{\gamma}_{\mu\nu}$, the conformal metric of the background spatial sections, the components of the perturbation $h_{\mu\nu}$ can be written as

$$h_{00} = -2A, \qquad h_{0i} = B_i, \qquad h_{ij} = 2C\tilde{\gamma}_{ij} + 2E_{ij}, \tag{3.6}$$

where A and C are scalars, and B_i and E_{ij} are respectively a 3-vector and a traceless 3-tensor defined in the homogeneous and isotropic space. Thus their indices are raised and lowered with the metric of the maximally symmetric space $\tilde{\gamma}_{ij}$. We introduce the covariant derivative D_i, compatible with $\tilde{\gamma}_{ij}$.

The perturbations can be further decomposed. Reference [41] provides a formal proof for the decompositions theorems for vector and traceless tensor fields. Explicitly,

$$B_i = \partial_i B + \hat{B}_i, \tag{3.7}$$

where B is the scalar part and $\hat{B}_i$ is the vector part. The scalar part of B_i is manifestly irrotational while the vector part is divergenceless by definition, $D^i\hat{B}_i \equiv 0$. There is a similar construction for traceless tensor fields,

$$E_{ij} = \mathcal{D}_{ij}E + D_{(i}\hat{E}_{j)} + \hat{E}_{ij}, \tag{3.8}$$

where $\hat{E}_i$ is divergenceless, $\hat{E}_{ij}$ is a transverse ($D_i\hat{E}^i{}_j = 0$) and traceless tensor, and

$$\mathcal{D}_{ij} \equiv D_i D_j - \frac{1}{3}\tilde{\gamma}_{ij}D^2.$$

Note that the hats on $\hat{B}_i$, $\hat{E}_i$, and $\hat{E}_{ij}$ are just to distinguish them from B_i and E_{ij}. In conclusion, we have four scalar quantities (A, B, C, and E), two vector quantities (with two degrees of freedom each, $\hat{B}_i$ and $\hat{E}_i$) and one traceless, transverse, and symmetric tensor with two degrees of freedom ($\hat{E}_{ij}$). Thus this decomposition fulfills all degrees of freedom of the metric. The metric for each mode is

- Scalar

$$\mathrm{d}s^2 = a^2(\eta)\left[-(1+2A)\mathrm{d}\eta^2 + 2\partial_i B\mathrm{d}\eta\mathrm{d}x^i + (\tilde{\gamma}_{ij} + 2(C\tilde{\gamma}_{ij} + \mathcal{D}_{ij}E))\mathrm{d}x^i\mathrm{d}x^j\right]$$

- Vector

$$\mathrm{d}s^2 = a^2(\eta)\left[-d\eta^2 + 2\hat{B}_i\mathrm{d}\eta\mathrm{d}x^i + \left(\tilde{\gamma}_{ij} + D_i\hat{E}_j + D_j\hat{E}_i\right)\mathrm{d}x^i\mathrm{d}x^j\right]$$

- Tensor

$$\mathrm{d}s^2 = a^2(\eta)\left[-\mathrm{d}\eta^2 + (\tilde{\gamma}_{ij} + 2\hat{E}_{ij})\mathrm{d}x^i\mathrm{d}x^j\right].$$

The SVT decomposition is useful because, when plugged into the linearized Einstein's Field Equations, each mode will evolve independently from the others. A proof of this is found in Appendix B of [42]. Another major simplification comes from realizing that some degrees of freedom of the metric perturbations (3.6) are non-physical. Equation (3.3) shows how the metric perturbation changes under a change of gauge. Writing

$$\boldsymbol{\zeta} = T\partial_0 + (\partial^i L + \hat{L}^i)\partial_i,$$

we see that

$$\begin{aligned}\mathcal{L}_{\zeta}\bar{g}_{\mu\nu} = -2a(aT)'d\eta^2 + 2a^2\left[\hat{L}_i' + \partial_i(L' - T)\right]dx^i d\eta \\ + a^2\left[2\mathcal{H}T\tilde{\gamma}_{ij} + 2D_iD_jL + D_j\hat{L}_i + D_i\hat{L}_j\right]dx^i dx^j.\end{aligned}$$

Thus we see that the perturbation variables transform as

Scalar	Vector	Tensor
$A \to A - \frac{1}{a}(aT)'$	$\hat{B}_i \to \hat{B}_i - \hat{L}_i'$	$\hat{E}_{ij} \to \hat{E}_{ij}.$
$B \to B - L' + T$	$\hat{E}_i \to \hat{E}_i - \hat{L}_i$	
$C \to C - \mathcal{H}T - \frac{1}{3}D^2L$		
$E \to E - L$		

This gauge freedom can be exploited to eliminate some degrees of freedom. This means that the physical interpretation of the perturbations is gauge-dependent. However, physical observables are gauge-independent. In this context, it is possible to write the perturbations using gauge-independent variables. The tensor modes are explicitly gauge-invariant, and the other modes can be set into gauge-independent variables by the following combinations:

Scalar

$$\Psi = A + \frac{1}{a}\left[a(B-E')\right]'$$
$$\Phi = -C + \frac{1}{3}D^2E - \mathcal{H}(B-E')$$

Vector

$$\hat{\Phi}_i = \hat{B}_i - \hat{E}_i'.$$

Instead of working with gauge-independent variables, we will work in a fixed gauge, the synchronous gauge. This is because the dynamics of Bianchi models, to which FLRW perturbations will be compared to, are more simply written in the synchronous gauge. This gauge sets $A = 0$ and $B_i = 0$, such that there are no perturbations in the time coordinate. Writing $C = -\phi$ and $E = \psi$, the metric perturbations in the synchronous gauge are

- Scalar
$$\mathrm{d}s^2 = a^2(\eta)\left[-\mathrm{d}\eta^2 + (\tilde{\gamma}_{ij} + 2(-\phi\tilde{\gamma}_{ij} + \mathcal{D}_{ij}\psi))\mathrm{d}x^i\mathrm{d}x^j\right] \tag{3.9}$$

- Vector
$$\mathrm{d}s^2 = a^2(\eta)\left[-d\eta^2 + \left(\tilde{\gamma}_{ij} + D_i\hat{E}_j + D_j\hat{E}_i\right)\mathrm{d}x^i\mathrm{d}x^j\right] \tag{3.10}$$

- Tensor
$$\mathrm{d}s^2 = a^2(\eta)\left[-\mathrm{d}\eta^2 + (\tilde{\gamma}_{ij} + 2\hat{E}_{ij})\mathrm{d}x^i\mathrm{d}x^j\right]. \tag{3.11}$$

Hence, all perturbations in the synchronous gauge are in the spatial components. This gauge can be interpreted as a choice of coordinate system where comoving free-falling observers carry clocks measuring the conformal time η, instead of measuring local variations of the time coordinate due to the perturbation A. The freedom to choose the initial coordinate labels gives rise to spurious degrees of freedom in this gauge; if we initially choose the synchronous gauge and then perform a transformation, we get

$$A = -\mathcal{H}T - T' \qquad B = L' - T \qquad \hat{B}_i = -\hat{L}_i'. \tag{3.12}$$

If this transformation is such that $A = 0$ and $B_i = 0$, that is, we do not change the gauge despite performing an infinitesimal transformation, we obtain

$$T = \frac{C_1(\boldsymbol{x})}{a} \qquad L = C_2(\boldsymbol{x}) + C_1(\boldsymbol{x})\int\frac{\mathrm{d}\eta}{a} \qquad \hat{L}^i = C_3^i(\boldsymbol{x}), \tag{3.13}$$

where $C_1(\boldsymbol{x})$, $C_2(\boldsymbol{x})$ and $C_3^i(\boldsymbol{x})$ are functions of the spatial coordinates and $C_3^i(\boldsymbol{x})$ is a divergenceless vector. Thus, the transformation generated by ζ^μ maps the point with coordinates x^μ to the point with coordinates $\tilde{x}^\mu$:

$$\tilde{x}^0 = \tilde{\eta} = \eta + \frac{C_1}{a} \qquad \tilde{x}^i = x^i + C_3^i + \partial^i C_2 + \partial^i C_1\int\frac{\mathrm{d}\eta}{a}, \tag{3.14}$$

showing why the choice $A = 0$ and $B_i = 0$ does not completely fix the gauge freedom. Note, however, that the functions C_2 and C_3^i only relabel the initial spatial coordinates while the function C_1 affects all spatial surfaces, so we only need to worry about C_1. In spite of this, we can fully fix this gauge by imposing comoving conditions on the cold dark matter fluid during radiation era [43], as we will do in the next section.

3.3 Matter Perturbations

The perturbations arise not only in the geometry but also in the matter content of the universe. Recall that the most general energy-momentum tensor for a family of observers comoving with the fluid content (equation (1.19)) is

$$T^{\mu}{}_{\nu} = (\rho + P)u^{\mu}u_{\nu} + P\delta^{\mu}{}_{\nu} + \Pi^{\mu}{}_{\nu}. \tag{3.15}$$

For instance, in contrast to the FLRW case, the fluids have a small bulk velocity v^i,

$$v^i = \frac{\mathrm{d}x^i}{\mathrm{d}\eta} = \frac{u^i}{u^0}, \tag{3.16}$$

such that $|v| \ll 1$. The normalization condition $u^{\mu}u_{\mu} = -1$ yields

$$u^0 = \frac{1}{a} \qquad \text{and} \qquad u^i = \frac{v^i}{a}. \tag{3.17}$$

This induces a momentum flux $q^i = (\bar{\rho} + \bar{P})v^i$, related to the momentum flux introduced in chapter 1 as $q^i = -j^i u_0 = aj^i$. Note that the fluids' four-velocity is not orthogonal to the spatial hypersurfaces, as it has spatial components. This means that the orthogonal vectors $n_{\mu} \equiv -(\mathrm{d}t)_{\mu}$ are not equal to u^{μ}, in contrast to the homogeneous and isotropic case.

Besides the four-velocity, the other energy-related variables are also perturbed: $\rho = \bar{\rho} + \delta\rho$ and $P = \bar{P} + \delta P$. The anisotropic stress Π_{ij} must be already of first order, as perfect fluids do not have this property. In this context, the components of the energy-momentum tensor are

$$\begin{aligned} T^{0}{}_{0} &= -\rho \\ T^{i}{}_{0} &= -q^i \\ T^{i}{}_{j} &= P\delta^{i}{}_{j} + \Pi^{i}{}_{j}. \end{aligned}$$

We can further parametrize $\rho = \bar{\rho}(1 + \delta)$, where $\bar{\rho}\delta = \delta\rho$. The pressure P is a function of both the energy density and the entropy density s, but we will assume that the perturbations are adiabatic, such that $(\partial P/\partial s)|_{\rho} = 0$; then the pressure perturbation is related with the energy density perturbation by the speed of sound in the fluid, $c_s^2 \equiv (\partial P/\partial\rho)$,

$$\delta P = c_s^2 \delta\rho. \tag{3.18}$$

With the components of the perturbed energy-momentum tensor, we can, in an analogous manner to the geometry perturbations, decompose the energy perturbations into scalars, vectors, and tensors. The pressure and the energy density are explicitly scalars. The bulk velocity and the anisotropic stress are decomposed as

$$v_i = \partial_i v + \hat{v}_i \tag{3.19}$$

and

$$\Pi_{ij} = \bar{P}(\mathcal{D}_{ij}\Pi + D_{(i}\hat{\Pi}_{j)} + \hat{\Pi}_{ij}). \tag{3.20}$$

We can now calculate how the perturbations change under a gauge transformation. We see that

$$\begin{aligned}
\mathcal{L}_\varsigma \bar{\rho} &= T\bar{\rho}' = -3\mathcal{H}T\bar{\rho}(1+w),\\
\mathcal{L}_\varsigma \bar{P} &= T\bar{P}',\\
\mathcal{L}_\varsigma \bar{u}^\mu &= -\frac{1}{a^2}[(Ta)'\delta^\mu{}_0 + a(L^i)'\delta^\mu{}_i],
\end{aligned}$$

then

$$\begin{aligned}
&\delta \to \delta + 3\mathcal{H}T(1+w),\\
&\delta P \to \delta P - \bar{P}'T,\\
&v^i \to v^i + (L^i)',\\
&\Pi^i{}_j \to \Pi^i{}_j.
\end{aligned}$$

We see that the anisotropic stress is already gauge invariant.

Having derived how the energy-momentum tensor changes under gauge transformations, we will now fix the synchronous gauge degrees of freedom. From the scalar part of the Euler Equation, equation (3.29) in the next section, we find that, for cold dark matter during radiation era ($a = \eta$), $v_{\text{CDM}} = v_0\eta^{-1}$. Under a gauge transformation, we saw that the scalar part of the velocity transforms as

$$\begin{aligned}
\tilde{v}_{\text{CDM}} &= v_{\text{CDM}} + L'\\
&= v_{\text{CDM}} + T,
\end{aligned} \tag{3.21}$$

where the last equality stems from the synchronous gauge condition. If we initially choose

$\tilde{v}_{\text{CDM}} = 0$, then we fix the function C_1,

$$C_1 = -v_0, \tag{3.22}$$

eliminating the remaining degree of freedom.

3.4 DYNAMICS OF PERTURBATIONS

Geometry and matter perturbations evolve according to the theory of General Relativity. The Einstein's Field Equations and the conservation condition for the energy-momentum tensor form a closed system of equations as long as the fluid approximation is valid. In this approximation, the hydrodynamics equations are enough to describe the evolution of the matter perturbations. This approximation is valid if the rate of interaction between particles is smaller than the expansion rate or in scales much larger than the mean free path of the particles. The conservation condition for the energy-momentum tensor adds four equations to the system, the Continuity Equation (one equation) and the Euler Equation (three equations).

Noticing that, in the synchronous gauge, $n^\mu \nabla_\mu n_\nu = 0$, the easiest way to compute these equations is to start from (1.15) and (1.16). Keeping only the first order terms in the synchronous gauge,

$$a^{-1}\bar{\rho}' + a^{-1}\delta\rho' + (\delta\rho + \delta P)\bar{\theta} + (\bar{\rho} + \bar{P})\delta\theta + a^{-1}D_i q^i = 0, \tag{3.23}$$

$$q_i' + \frac{4}{3}\bar{\theta} a q_i + D_i \delta P + D_j \Pi^j{}_i = 0 \tag{3.24}$$

and the perturbed expansion is

$$\begin{aligned} \theta &= \nabla_\mu n^\mu & (3.25)\\ &= (n^0)' + \Gamma^\mu_{\mu\nu} n^\nu & (3.26)\\ &= 3\frac{\mathcal{H}}{a} - 3\frac{\mathcal{H}}{a}\phi'. & (3.27) \end{aligned}$$

As mentioned earlier, each perturbation mode decouples and evolves independently from one another in the linear regime. In the following, we list the dynamics equations [18].

- Scalar

  The Continuity Equation is a pure scalar equation:

$$\delta' = -(1 + w)(D^2 v - 3\phi') - 3\mathcal{H}(c_s^2 - w)\delta. \tag{3.28}$$

  The Euler Equation has a scalar and a vector component. The scalar component is

$$q' + 4\mathcal{H}q + \delta P + 2\bar{P}\left(\frac{1}{3}D^2 + K\right)\Pi = 0. \tag{3.29}$$

The EFEs are:

$$(D^2 + 3K)\phi - 3\mathcal{H}\phi' + \mathcal{H}D^2\psi' = 4\pi Ga^2\bar{\rho}\delta \tag{3.30}$$

$$\phi' + K\psi' = -4\pi Ga^2 q \tag{3.31}$$

$$\phi'' + 2\mathcal{H}\phi' - K\phi = 4\pi Ga^2\bar{P}\left(\frac{\delta P}{\bar{P}} + \frac{2}{3}D^2\Pi\right) \tag{3.32}$$

$$\psi'' + 2\mathcal{H}\psi' + \phi = 8\pi Ga^2\bar{P}\Pi. \tag{3.33}$$

- Vector

  The vector mode of the Euler Equation is

  $$\hat{q}_i' + 4\mathcal{H}\hat{q}_i = -\bar{P}\left(D^2 + 2K\right)\hat{\Pi}_i. \tag{3.34}$$

  The EFEs are

  $$\left(D^2 + 2K\right)\hat{\Phi}^i = 16\pi Ga^2\hat{q}^i \tag{3.35}$$

  $$\hat{\Phi}_j' + 2\mathcal{H}\hat{\Phi}_j = -8\pi Ga^2\bar{P}\hat{\Pi}_j, \tag{3.36}$$

  where $\hat{\Phi}_i = -\hat{E}_i'$.

- Tensor

  Finally, the only tensor equation comes from the EFEs:

  $$\hat{E}_{ij}'' + 2\mathcal{H}\hat{E}_{ij}' + \left(2K - D^2\right)\hat{E}_{ij} = 8\pi Ga^2\bar{P}\hat{\Pi}_{ij}. \tag{3.37}$$

Cold Dark Matter and the tightly coupled photon-baryon fluid are well described in the fluid approximation (in scales larger than the mean free path). Neutrinos and photons (after recombination) are free streaming particles sourcing anisotropic stress, and thus, on small scales, their physics is not contained in the hydrodynamics equations in this section.

3.5 HARMONIC DECOMPOSITION

The system of equations in the previous section has the disadvantage of being a system of partial differential equations in space and time. Luckily, in the context of linear perturbation theory, the perturbations can be expanded into (properly defined) harmonics such that partial differential equations can be converted into ordinary differential equations. In flat space, these harmonics are derived from a Fourier transform, where the functions are expanded into a basis of plane waves $e^{i\boldsymbol{k}\cdot\boldsymbol{x}}$. In general maximally symmetric spaces, the eigenfunctions of the Laplacian operator, which we call *tensor harmonics*, take the role of basis. The scalar, vector, and tensor harmonics are solutions of

$$(D^2 + k^2)Q^{(0)} = 0, \tag{3.38}$$

$$(D^2 + k^2)Q_i^{(\pm 1)} = 0, \tag{3.39}$$

$$(D^2 + k^2)Q_{ij}^{(\pm 2)} = 0, \tag{3.40}$$

where $Q_i^{(\pm 1)}$ is divergenceless and $Q_{ij}^{(\pm 2)}$ is a symmetric transverse-traceless tensor. Thus, quite generally, the scalar perturbations are written in terms of $Q^{(0)}$, the vector perturbations are expanded in $Q_i^{(\pm 1)}$, and the tensor perturbations are expanded in terms of $Q_{ij}^{(\pm 2)}$. Other perturbations can appear as spatial derivatives of scalars and vectors, so, to account for them, we introduce the *derived* harmonics

$$Q_i^{(1,0)} \equiv -k^{-1} D_i Q^{(0)} \tag{3.41}$$

$$Q_{ij}^{(2,0)} \equiv k^{-2} D_i D_j Q^{(0)} + \frac{1}{3}\tilde{\gamma}_{ij} Q^{(0)} \tag{3.42}$$

$$Q_{ij}^{(2,\pm 1)} \equiv -k^{-1} D_{(i} Q_{j)}^{(\pm 1)}, \tag{3.43}$$

then $Q_i^{(1,0)}$ is the basis for $D_i q$, $Q_{ij}^{(2,0)}$ is the basis for $\mathcal{D}_{ij}\psi$ and $\mathcal{D}_{ij}\Pi$, and $Q_{ij}^{(2,\pm 1)}$ is the basis for $D_{(i}\hat{E}_{j)}$ and $D_{(i}\hat{\Pi}_{j)}$.

To illustrate how this decomposition simplifies the EFEs, consider vector and tensor modes. This will be important in the next chapter. We have, for the vector modes,

$$\hat{q}_i = \sum_{a=\pm 1} q_{(a)} Q_i^{(a)}, \qquad \hat{\Phi}_i = \sum_{a=\pm 1} \Phi_{(a)} Q_i^{(a)}, \qquad \hat{\Pi}_i = -\frac{1}{k} \sum_{a=\pm 1} \Pi_{(a)} Q_i^{(a)}, \tag{3.44}$$

where the last term stems from

$$\begin{aligned} D_{(i}\hat{\Pi}_{j)} &= \sum_{a=\pm 1} \Pi_{(a)} Q_{ij}^{(2,a)} \\ &= -\frac{1}{k} \sum_{a=\pm 1} \Pi_{(a)} D_{(i} Q_{j)}^{(a)}. \end{aligned} \tag{3.45}$$

Thus the equations for these modes become

$$k(q'_{(a)} + 4\mathcal{H} q_{(a)}) = \bar{P}\left(-k^2 + 2K\right)\Pi_{(a)} \tag{3.46}$$

$$-\left(k^2 - 2K\right)\Phi_{(a)} = 16\pi G a^2 q_{(a)} \tag{3.47}$$

$$k(\Phi'_{(a)} + 2\mathcal{H}\Phi_{(a)}) = 8\pi G a^2 \bar{P}\Pi_{(a)}. \tag{3.48}$$

For tensor modes, $\hat{E}_{ij} = \sum_{\lambda=\pm 2} E_{(\lambda)} Q_{ij}^{(\lambda)}$ and $\hat{\Pi}_{ij} = \sum_{\lambda=\pm 2} \Pi_{(\lambda)} Q_{ij}^{(\lambda)}$ such that

$$E''_{(\lambda)} + 2\mathcal{H} E_{(\lambda)} + (k^2 + 2K)E_{(\lambda)} = 8\pi G a^2 \bar{P}\Pi_{(\lambda)}. \tag{3.49}$$

As a consequence, equations (3.46) – (3.49) are simple ODEs in time.

To gain some intuition, let us consider the solution to these equations during the radiation era, while curvature can be neglected and $\mathcal{H} = \eta^{-1}$. Without a source, the vector modes decay:

$$q'_{(a)} + \frac{4}{\eta} q_{(a)} = 0 \Rightarrow q_{(a)} \propto \eta^{-4}, \tag{3.50}$$

$$\Phi_{(a)} + \frac{2}{\eta} \Phi_{(a)} = 0 \Rightarrow \Phi_{(a)} \propto \eta^{-2}. \tag{3.51}$$

Thus, they become singular at $\eta = 0$. Unless there is a mechanism acting as the anisotropic stress, the vector modes do not significantly affect the evolution of the CMB and structures, and are set to zero initially.

Similarly, for tensor modes,

$$E''_{(\lambda)} + \frac{2}{\eta} E_{(\lambda)} + k^2 E_{(\lambda)} = 0 \Rightarrow E_{(\lambda)} = A_1 \frac{\cos(k\eta)}{\eta} + A_2 \frac{\sin(k\eta)}{\eta}. \tag{3.52}$$

As $\eta \to 0$, we see that the first solution for $E_{(\pm 2)}$ diverges while the other goes to a constant. Thus, even without some physical source of anisotropic stress, there is a non-decaying tensor mode. This is a very important result and lies at the heart of the identification between Bianchi and FLRW.

These sections comprise the fundamental aspects of perturbation theory. With these tools, we can move forward to study the Cosmic Microwave Background.

3.6 Cosmic Microwave Background

The Cosmic Microwave Background is a remnant from the early universe. It is a thermal radiation with temperature fluctuations Θ of order 10^{-5} K. In standard cosmology, these fluctuations have their origin in the primordial quantum fluctuations produced during inflation. The CMB photons are also polarized, due to the coupling with electrons through Thomson scattering. There are two polarization fields, E and B, which are linear combinations of two of the four Stokes parameters. Figure 6 shows the temperature fluctuations of the CMB for three recent missions.

According to inflation, the temperature fluctuation and polarization fields are Gaussian random fields with zero mean, so all the information is contained in the two point function of these fields. In the context of Bianchi cosmologies, the non-standard geometry induces a deterministic effect in the statistics of photons of the CMB, and this information is also contained in the two point correlation function.

In the following, we will explore the evolution of temperature fluctuations in a flat universe. As we mentioned in the previous section, the fluid approximation cannot fully describe the physics of the CMB. To describe the evolution of Θ, we must use kinetic theory. Kinetic theory asserts that all the information regarding the state of a species is in its distribution function

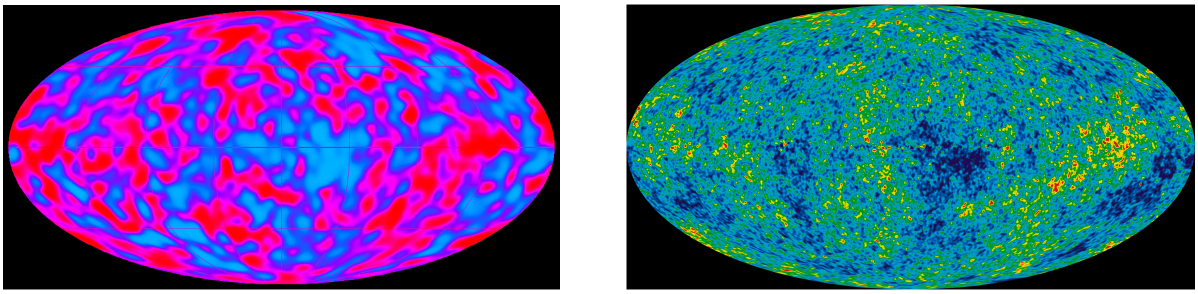

(a) COBE **(b)** WMAP

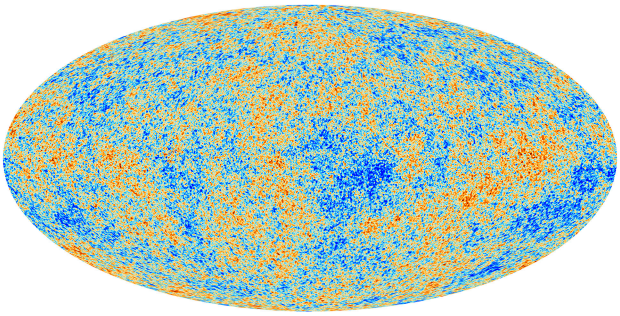

(c) Planck

Figure 6: CMB temperature fluctuation maps. a) COBE telescope, launched in 1989 with an angular resolution of about $6°$. b) WMAP missions, launched in 2001 with angular resolution $\sim 0,3°$. c) Planck satellite, launched in 2009 with angular resolution around $0,07°$.
Source: NASA

$f(x^\mu, p^\mu)$. The phase space in this context is an eight-dimensional space with points determined by the position in spacetime and the four-momentum, but we are interested in interactions localized in spacetime, so the position x^μ is usually fixed. Also, in general, there is a constraint in the four-momentum, as we require that $p^\mu p_\mu = 0$ for photons, called the on-shell condition. Imposing this condition allows p^0 to be written in terms of the other components, thus reducing the number of degrees of freedom.

In the kinetic theory description, the energy-momentum tensor is defined as [44]

$$T^\mu_{\ \nu}(x^\alpha) = \frac{1}{\sqrt{-g}} \int f(x^\alpha, p^\alpha) \frac{p^\mu p_\nu}{p^0} \mathrm{d}^3 p \tag{3.53}$$

and it is called the second moment of the distribution $f(x^\alpha, p^\alpha)$. Since we can take higher moments from the distribution, we see that, in general, the energy-momentum tensor does not contain all the information about a particle species.

3.6.1 Boltzmann Equation

The evolution of $\Theta(\eta, \boldsymbol{x}, \hat{\boldsymbol{n}})$, where $\boldsymbol{x}$ is the spatial position and $\hat{\boldsymbol{n}}$ is the direction of the incoming photon, is fully described by the evolution of the photon distribution function, $f(\eta, \boldsymbol{x}, E, \hat{\boldsymbol{p}})$, where $E = -p^\mu n_\mu$ is the photon energy measured by an observer with four-velocity n_μ and $\hat{\boldsymbol{p}} = -\hat{\boldsymbol{n}}$ is the photon propagation direction. For a homogeneously distributed photon gas at temperature T, the distribution function takes the form of the Bose-Einstein distribution

$$f\left(\frac{E}{T}\right) = \left[\exp\left(\frac{E}{T}\right) - 1\right]^{-1}. \tag{3.54}$$

In a perturbed universe, the temperature can be written in terms of its small perturbations δT as

$$T = \bar{T}\left(1 + \frac{\delta T}{\bar{T}}\right) = \bar{T}(1+\Theta), \tag{3.55}$$

where $\Theta \equiv \delta T/T$. The background temperature $\bar{T}$ falls with a, so we can write

$$f(\eta, \boldsymbol{x}, E, \hat{\boldsymbol{p}}) = \left[\exp\left(\frac{aE}{\bar{T}_0(1+\Theta)}\right) - 1\right]^{-1}, \tag{3.56}$$

where $\bar{T}_0$ is the average temperature of the radiation measured today. Next, we can Taylor expand the distribution function to first order in the perturbations, obtaining

$$f(\eta, \boldsymbol{x}, \mathcal{E}, \hat{\boldsymbol{p}}) = \bar{f}(\mathcal{E}) - \Theta(\eta, \boldsymbol{x}, \hat{\boldsymbol{n}})\frac{\mathrm{d}\bar{f}}{\mathrm{d}\ln\mathcal{E}}, \tag{3.57}$$

where $\mathcal{E} \equiv aE$.

The evolution of the distribution function is determined by the Boltzmann equation,

$$\frac{\mathrm{d}f}{\mathrm{d}\eta} = C[f], \tag{3.58}$$

where $C[f]$ is a functional called “collision term”, which takes into account the interaction of the photons with the electrons. The time derivative of the distribution function can be further written as

$$\frac{\mathrm{d}f}{\mathrm{d}\eta} = \frac{\partial f}{\partial\eta} + \frac{\partial f}{\partial x^i}\frac{\mathrm{d}x^i}{\mathrm{d}\eta} + \frac{\partial f}{\partial\mathcal{E}}\frac{\mathrm{d}\mathcal{E}}{\mathrm{d}\eta} + \frac{\partial f}{\partial\hat{p}^i}\frac{\mathrm{d}\hat{p}^i}{\mathrm{d}\eta}. \tag{3.59}$$

Moving forward, photons follow a null-geodesic parametrized by an affine parameter λ. The photon four-momentum is given by

$$p^\mu \equiv \frac{\mathrm{d}x^\mu}{\mathrm{d}\lambda} = \frac{\mathrm{d}x^\mu}{\mathrm{d}\eta}p^0. \tag{3.60}$$

With this, equation (3.59) can be written as

$$\frac{\mathrm{d}f}{\mathrm{d}\eta} = \frac{\partial f}{\partial\eta} + \frac{\partial f}{\partial x^i}\frac{\bar{p}^i}{\bar{p}^0} + \frac{\partial f}{\partial\ln\mathcal{E}}\frac{\mathrm{d}\ln\mathcal{E}}{\mathrm{d}\eta} + \frac{\partial f}{\partial\hat{p}^i}\frac{\mathrm{d}\hat{p}^i}{\mathrm{d}\eta}. \tag{3.61}$$

Since any change in the photon propagation direction is already of first order and any dependency of f on $\hat{p}^i$ is also of first order, the last term is of second order and thus negligible. Substituting

(3.57) and keeping only first order terms, we find

$$\frac{\mathrm{d}\delta f}{\mathrm{d}\eta} = -\frac{\mathrm{d}\bar{f}}{\mathrm{d}\ln\mathcal{E}}\left(\Theta' + \hat{p}^i\partial_i\Theta - \frac{\mathrm{d}\ln\mathcal{E}}{\mathrm{d}\eta}\right). \tag{3.62}$$

The energy-shift induced by gravitational effects is called the Sachs-Wolfe term, and we can use the geodesic equation to compute it. From the equation $E = -p^\mu n_\mu$, we see that the time component of the photon four-momentum relates with the energy in the synchronous gauge as

$$p^0 = \frac{E}{a}. \tag{3.63}$$

We now exploit the fact that null geodesics are conformally invariant, meaning that spacetimes with metrics $\tilde{g}_{\mu\nu}$ and $g_{\mu\nu} = a^2\tilde{g}_{\mu\nu}$ have the same null geodesics, provided that the affine parameters parametrizing them have the following relation [22]

$$\frac{\mathrm{d}\lambda}{\mathrm{d}\tilde{\lambda}} = a^2. \tag{3.64}$$

Defining a new four-momentum

$$\tilde{p}^\mu = \frac{\mathrm{d}x^\mu}{\mathrm{d}\tilde{\lambda}} = a^2 p^\mu, \tag{3.65}$$

we have the geodesic equation

$$\frac{\mathrm{d}\tilde{p}^\mu}{\mathrm{d}\tilde{\lambda}} = -\tilde{\Gamma}^\mu_{\alpha\beta}\tilde{p}^\alpha\tilde{p}^\beta, \tag{3.66}$$

where $\tilde{\Gamma}^\mu_{\alpha\beta}$ is the Christoffel symbol calculate with the metric $\tilde{g}_{\mu\nu} = \eta_{\mu\nu} + h_{\mu\nu}$, $\eta_{00} = -1$, $\eta_{0i} = 0$, and $\eta_{ij} = \delta_{ij}$. Since we are only interested in the $\mu = 0$ component of the geodesic equation, we only need $\tilde{\Gamma}^0_{\alpha\beta}$, but this term is already of first order:

$$\tilde{\Gamma}^0_{\alpha\beta} = -\frac{1}{2}(\partial_\alpha h_{0\beta} + \partial_\beta h_{0\alpha} - h'_{\alpha\beta}) \tag{3.67}$$

$$= \frac{1}{2}h'_{\alpha\beta}. \tag{3.68}$$

Thus, noting that

$$\frac{\mathrm{d}\tilde{p}^\mu}{\mathrm{d}\tilde{\lambda}} = a^2\frac{\mathrm{d}}{\mathrm{d}\lambda}\left(a^2 p^\mu\right), \tag{3.69}$$

the geodesic equation becomes

$$\frac{\mathrm{d}}{\mathrm{d}\eta}\left(a^2 p^0\right) = -a^2 h'_{\alpha\beta}\frac{p^\alpha p^\beta}{2p^0}, \tag{3.70}$$

from where we get the Sachs-Wolfe term in the synchronous gauge

$$\frac{\mathrm{d}\ln\mathcal{E}}{\mathrm{d}\eta} = -\frac{1}{2}h'_{ij}\hat{p}^i\hat{p}^j. \tag{3.71}$$

It is usual to write the energy-shift term as $\mathcal{G}$ since it is the gravitational "source" in the Boltzmann equation, which we rewrite now as

$$\Theta' + \hat{p}^i \partial_i \Theta = -\left(\frac{\mathrm{d}\bar{f}}{\mathrm{d}\ln\mathcal{E}}\right)^{-1} C[f] + \mathcal{G}. \tag{3.72}$$

Before decoupling, photons interact via Thomson scattering with electrons. This phenomenon is taken into account through the collision term in the Boltzmann equation. The collision term $C[f(\boldsymbol{p})]$ is proportional to the net change of photons from momentum $\boldsymbol{p}$ to any possible momentum $\boldsymbol{p}'$ and the inverse process, marginalizing over all the possible electron momenta and weighted by the interaction rate $\Gamma \equiv a n_e \sigma_T [1 + (\boldsymbol{p}' \cdot \boldsymbol{p})^2]$, where n_e is the free electron number density and σ_T is the Thomson scattering cross-section. Explicitly, we have [45]

$$C[f(\boldsymbol{p})] = -\tau' \frac{\mathrm{d}\bar{f}}{\mathrm{d}\ln\mathcal{E}} \left(\Theta - \hat{\boldsymbol{p}} \cdot \boldsymbol{v}_b - \int \frac{\mathrm{d}^2\hat{\boldsymbol{n}}}{4\pi} \Theta(\eta, \boldsymbol{x}, \hat{\boldsymbol{n}})\right) + \text{Polarization terms}, \tag{3.73}$$

where we introduced the quantity

$$\tau \equiv \int_{\eta}^{\eta_0} \mathrm{d}\eta' a n_e \sigma_T, \tag{3.74}$$

known as the optical depth. The quantity $\boldsymbol{v}_b$ is the baryon bulk velocity. In this development, we are going to ignore polarization, as our intention here is to provide an overview of the derivation of the Boltzmann equation. However, we stress that, in `AniCLASS` and `AniLoS`, polarization is included.

Finally, plugging the collision term in the Boltzmann equation,

$$\Theta' + \hat{p}^i \partial_i \Theta = \tau' \left(\Theta - \hat{\boldsymbol{p}} \cdot \boldsymbol{v}_b - \int \frac{\mathrm{d}^2\hat{\boldsymbol{n}}}{4\pi} \Theta(\eta, \boldsymbol{x}, \hat{\boldsymbol{n}})\right) + \mathcal{G}. \tag{3.75}$$

3.6.2 Boltzmann hierarchy

To move further, we will expand the quantities in the Boltzmann equation into the harmonics introduced in equations (3.38) – (3.40). As we are dealing only with flat space[11], the scalar eigenfunction of the Laplacian is $Q^{(0)} = e^{i\boldsymbol{k}\cdot\boldsymbol{x}}$. The vector and tensor functions are readily given in terms of plane waves once we choose a convenient basis $\boldsymbol{m}^{\pm}$ satisfying $k^i m_i^{\pm} = 0$ (divergenceless condition) and $(m^{\pm})^i m_i^{\pm} = 0$ (traceless condition). Setting $\boldsymbol{k} = k\partial_3$, a good basis is the polarization basis

$$\boldsymbol{m}^{\pm} = \partial_1 \pm i\partial_2. \tag{3.76}$$

---

[11] Note that we are assuming a flat space for simplification purposes. In the programs, the CMB equations are implemented for arbitrary curved spaces.

Thus, the vector and tensor harmonics become

$$Q_i^{(\pm 1)} = -\frac{i}{\sqrt{2}} e^{i\boldsymbol{k}\cdot\boldsymbol{x}} m_i^{\pm}, \tag{3.77}$$

$$Q_{ij}^{(\pm 2)} = -\sqrt{\frac{3}{8}} e^{i\boldsymbol{k}\cdot\boldsymbol{x}} m_i^{\pm} m_j^{\pm}. \tag{3.78}$$

The choice of numerical factors will be made clear in a bit.

The CMB temperature fluctuation is a function of both the position $\boldsymbol{x} = -\chi\hat{\boldsymbol{p}}$ and the photon propagation direction $\hat{\boldsymbol{p}}$. The description of its dynamics depends on the dynamics of the perturbations. The angular dependency of this observable may be written in terms of spherical harmonics, whereas the spatial dependency may be decomposed into plane waves. Hence, a convenient basis for this observable is the total angular momentum basis [46]

$$G_\ell^m(\boldsymbol{x}, \hat{\boldsymbol{p}}, \boldsymbol{k}) \equiv (-i)^\ell \sqrt{\frac{4\pi}{2\ell+1}} Y_\ell^m(\hat{\boldsymbol{p}}) \exp(i\boldsymbol{k}\cdot\boldsymbol{x}). \tag{3.79}$$

However, plane waves also carry an angular dependency. Recalling that $\boldsymbol{k} = k\partial_3$, we can expand $\exp(i\boldsymbol{k}\cdot\boldsymbol{x})$ as [47]

$$\exp(i\boldsymbol{k}\cdot\boldsymbol{x}) = \sum_n (-i)^n \sqrt{4\pi(2n+1)} j_n(k\chi) Y_n^0(\hat{\boldsymbol{p}}), \tag{3.80}$$

where $j_n(k\chi)$ is the spherical Bessel function and we used $\boldsymbol{k}\cdot\boldsymbol{x} = -\chi\boldsymbol{k}\cdot\hat{\boldsymbol{p}} = -k\chi\cos\vartheta$. The total angular dependency of the basis G_ℓ^m can now be written explicitly using the Clebsch-Gordan relations, which show that $Y_n^0(\hat{\boldsymbol{p}})Y_\ell^m(\hat{\boldsymbol{p}})$ is a linear combination of spherical harmonics $Y_{\ell'}^{m'}(\hat{\boldsymbol{p}})$ with $m' = m$ and multipoles ranging from $|\ell - n|$ to $|\ell + n|$. Thus,

$$G_\ell^m = \sum_n (-i)^n \sqrt{4\pi(2n+1)} j_n^{(\ell m)}(k\chi) Y_n^m(\hat{\boldsymbol{p}}). \tag{3.81}$$

As we can see, these functions have a close connection with the harmonics, which makes them very useful. The function $j_n^{(\ell m)}(k\chi)$ contain the coefficients appearing in the Clebsch-Gordan relation [46]. For instance, some expressions for the radial functions in flat space are

$$j_n^{(00)} = j_n \tag{3.82}$$

$$j_n^{(10)} = \frac{\mathrm{d}j_n(k\chi)}{\mathrm{d}k\chi} \tag{3.83}$$

$$j_n^{(11)} = \sqrt{\frac{n(n+1)}{2}} \frac{j_n}{k\chi}. \tag{3.84}$$

See Figure 7 for an illustration of $j_n^{(00)}$.

The harmonics can be cast in terms of G_ℓ^m. From the definition (3.79) we see that $Q^{(0)} =$

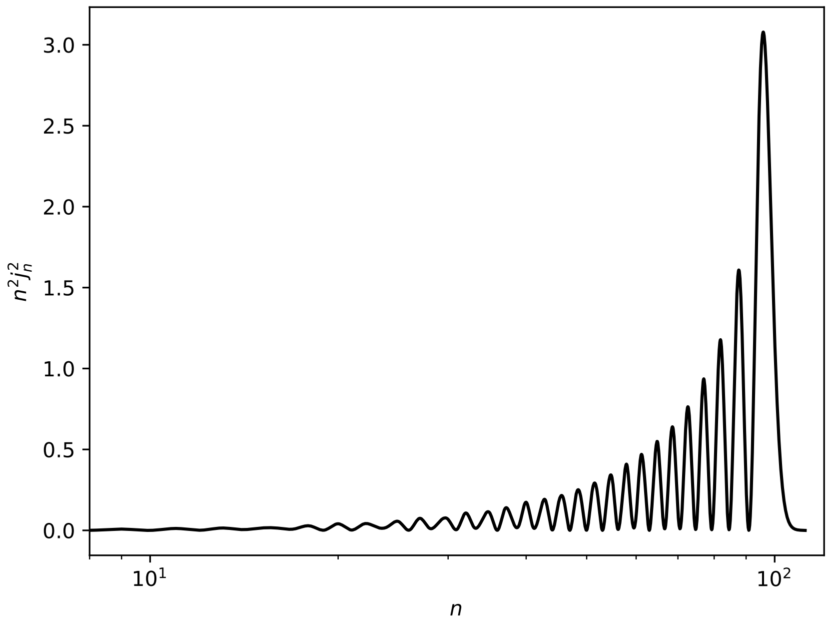

Figure 7: The function $n^2 j_n^2$ for several values of n. This figure was made using the routines that compute the hyperspherical Bessel functions in `AniLoS`. Compare it with Figure 3 in ref [46].

$e^{i\boldsymbol{k}\cdot\boldsymbol{x}} = G_0^0$ so that

$$\begin{aligned}\hat{p}^i \partial_i Q^{(0)} &= i\hat{p}^i k_i e^{i\boldsymbol{k}\cdot\boldsymbol{x}} \\ &= ik\sqrt{\frac{4\pi}{3}} Y_1^0(\hat{\boldsymbol{p}}) e^{i\boldsymbol{k}\cdot\boldsymbol{x}} \\ &= -kG_1^0. \end{aligned} \tag{3.85}$$

Therefore, recalling the definition of the derived harmonics (equations (3.41) – (3.43)), we find

$$\hat{p}^i Q_i^{(1,0)} = G_1^0,$$

and

$$\hat{p}^i \hat{p}^j Q_{ij}^{(2,0)} = \frac{2}{3} G_2^0.$$

This shows that they only source modes $m = 0$. Analogously, vector and tensor perturbations have

$$\begin{aligned}\hat{p}^i Q_i^{(\pm 1)} &= \pm G_1^{\pm 1}, \\ \hat{p}^i \hat{p}^j Q_{ij}^{(2,\pm 1)} &= \mp \frac{1}{\sqrt{3}} G_2^{\pm 1}, \\ \hat{p}^i \hat{p}^j Q_{ij}^{(\pm 2)} &= G_2^{\pm 2}. \end{aligned}$$

Hence, vector and tensor perturbations only source modes $m = \pm 1$ and $m = \pm 2$, respectively.

The next step in the derivation is to expand the temperature fluctuations into the basis (3.79),

$$\Theta(\eta, \boldsymbol{x}, \hat{\boldsymbol{p}}) = \int \frac{\mathrm{d}^3\boldsymbol{k}}{(2\pi)^3} \sum_{\ell=0}^{\infty} \sum_{m=-2}^{2} \Theta_\ell^{(m)}(\eta, \boldsymbol{k}) G_\ell^m(\boldsymbol{x}, \hat{\boldsymbol{p}}, \boldsymbol{k}), \tag{3.86}$$

such that

$$\int \frac{\mathrm{d}^2\hat{\boldsymbol{n}}}{4\pi} \Theta(\hat{\boldsymbol{n}}) = \int \frac{\mathrm{d}^3\boldsymbol{k}}{(2\pi)^3} \Theta_0^{(0)} G_0^0. \tag{3.87}$$

Setting $\mathcal{G}$ and $C[f]$ into this format is straightforward. The only non-trivial term is the free streaming $\hat{p}^i\partial_i\Theta$. We saw in equation (3.85) that

$$\hat{p}^i\partial_i \to ik\sqrt{\frac{4\pi}{3}} Y_1^0(\hat{\boldsymbol{p}}),$$

so the free streaming term becomes

$$\hat{p}^i\partial_i\Theta = \int \frac{\mathrm{d}^3\boldsymbol{k}}{(2\pi)^3} k e^{i\boldsymbol{k}\cdot\boldsymbol{x}} \sum_{\ell=0}^{\infty} \sum_{m=-2}^{2} (-i)^{\ell-1} \frac{4\pi}{\sqrt{3(2\ell+1)}} \Theta_\ell^{(m)}(\eta, \boldsymbol{k}) Y_1^0(\hat{\boldsymbol{p}}) Y_\ell^m(\hat{\boldsymbol{p}}). \tag{3.88}$$

The product $Y_1^0(\hat{\boldsymbol{p}})Y_\ell^m(\hat{\boldsymbol{p}})$ can be simplified using the recursion relations of the Legendre functions. The spherical harmonics can be written as [48]

$$Y_\ell^m(\vartheta, \varphi) = \sqrt{\frac{(2\ell+1)(\ell-m)!}{4\pi(\ell+m)!}} P_\ell^m(\cos\vartheta) e^{im\varphi}, \tag{3.89}$$

where we take $\mu \equiv \hat{p}^3 = \cos\vartheta$. Thus

$$\sqrt{\frac{4\pi}{3}} Y_1^0 Y_\ell^m = \sqrt{\frac{(2\ell+1)(\ell-m)!}{4\pi(\ell+m)!}} \mu P_\ell^m(\mu) e^{im\varphi}.$$

On the other hand, the Legendre function has the following recursion relation [49]

$$(\alpha - \beta + 1) P_{\alpha+1}^\beta(\mu) - (2\alpha+1)\mu P_\alpha^\beta(\mu) + (\alpha+\beta) P_{\alpha-1}^\beta(\mu) = 0, \tag{3.90}$$

where α and β are complex numbers. Thus the equation above can be used to write $\mu P_\ell^m(\mu)$ in terms of $P_{\ell-1}^m(\mu)$ and $P_{\ell+1}^m(\mu)$. From this equation we get

$$\sqrt{\frac{4\pi}{3}} Y_1^0 Y_\ell^m = \frac{\sqrt{\ell^2 - m^2}}{\sqrt{(2\ell+1)(2\ell-1)}} Y_{\ell-1}^m + \frac{\sqrt{(\ell+1)^2 - m^2}}{\sqrt{(2\ell+1)(2\ell+3)}} Y_{\ell+1}^m. \tag{3.91}$$

Then

$$\hat{p}^i\partial_i\Theta = \int \frac{\mathrm{d}^3\boldsymbol{k}}{(2\pi)^3} k \sum_{\ell=0}^{\infty} \sum_{m=-2}^{2} \left(\frac{\sqrt{(\ell+1)^2 - m^2}}{2\ell+3} \Theta_{\ell+1}^{(m)} - \frac{\sqrt{\ell^2 - m^2}}{2\ell-1} \Theta_{\ell-1}^{(m)} \right) G_\ell^m. \tag{3.92}$$

Substituting everything into the into the Boltzmann equation, we get

$$\frac{\partial\Theta_\ell^{(m)}}{\partial\eta} = k\left(\frac{\sqrt{\ell^2-m^2}}{2\ell-1}\Theta_{\ell-1}^{(m)} - \frac{\sqrt{(\ell+1)^2-m^2}}{2\ell+3}\Theta_{\ell+1}^{(m)}\right) + \tau'\Theta_\ell^{(m)} + \mathcal{G}_\ell^{(m)} + \mathcal{C}_\ell^{(m)}. \tag{3.93}$$

After collecting the results, we get the Boltzmann hierarchy for temperature fluctuations. The derivation of the hierarchy for polarization is similar, and we only give the final expressions (see [46, 50, 51]). The equation for neutrinos follows a collisionless version of the equation for photons. The full hierarchy is

$$\frac{\partial\mathcal{N}_\ell^{(m)}}{\partial\eta} = \left(\frac{{}_0\kappa_\ell^m}{2\ell-1}\mathcal{N}_{\ell-1}^{(m)} - \frac{{}_0\kappa_{\ell+1}^m}{2\ell+3}\mathcal{N}_{\ell+1}^{(m)}\right) + \mathcal{G}_\ell^{(m)} \tag{3.94}$$

$$\frac{\partial\Theta_\ell^{(m)}}{\partial\eta} = \left(\frac{{}_0\kappa_\ell^m}{2\ell-1}\Theta_{\ell-1}^{(m)} - \frac{{}_0\kappa_{\ell+1}^m}{2\ell+3}\Theta_{\ell+1}^{(m)}\right) + \tau'\Theta_\ell^{(m)} + \mathcal{G}_\ell^{(m)} + {}^{\Theta}\mathcal{C}_\ell^{(m)} \tag{3.95}$$

$$\frac{\partial E_\ell^{(m)}}{\partial\eta} = \left(\frac{{}_2\kappa_\ell^m}{2\ell-1}E_{\ell-1}^{(m)} - \frac{{}_2\kappa_{\ell+1}^m}{2\ell+3}E_{\ell+1}^{(m)}\right) - \frac{2m}{\ell(\ell+1)}B_\ell^{(m)} + \tau' E_\ell^{(m)} + {}^{E}\mathcal{C}_\ell^{(m)} \tag{3.96}$$

$$\frac{\partial B_\ell^{(m)}}{\partial\eta} = \left(\frac{{}_2\kappa_\ell^m}{2\ell-1}B_{\ell-1}^{(m)} - \frac{{}_2\kappa_{\ell+1}^m}{2\ell+3}B_{\ell+1}^{(m)}\right) + \frac{2m}{\ell(\ell+1)}E_\ell^{(m)} + \tau' B_\ell^{(m)} \tag{3.97}$$

where we defined

$${}_s\kappa_\ell^m = k\sqrt{\frac{(\ell^2-m^2)(\ell^2-s^2)}{\ell^2}}. \tag{3.98}$$

We have also introduced [51]

$$\begin{aligned}
\mathcal{G}_0^{(0)} &= \phi', \\
\mathcal{G}_1^{(0)} &= 0, \\
\mathcal{G}_2^{(0)} &= -\frac{2}{3}\psi', \\
\mathcal{G}_1^{(1)} &= 0, \\
\mathcal{G}_2^{(1)} &= -\frac{E'_{(1)}}{\sqrt{3}}, \\
\mathcal{G}_2^{(2)} &= -E'_{(2)},
\end{aligned}$$

$$\begin{aligned}
{}^{\Theta}\mathcal{C}_0^{(0)} &= -\tau'\Theta_0^{(0)}, \\
{}^{\Theta}\mathcal{C}_1^{(0)} &= -\tau' v_b, \\
{}^{\Theta}\mathcal{C}_2^{(0)} &= -\tau' P^0 \\
{}^{\Theta}\mathcal{C}_1^{(1)} &= -\tau'\hat{v}_b, \\
{}^{\Theta}\mathcal{C}_2^{(1)} &= -\tau' P^1, \\
{}^{\Theta}\mathcal{C}_2^{(2)} &= -\tau' P^2,
\end{aligned}$$

$$\begin{aligned}
{}^{E}\mathcal{C}_0^{(0)} &= 0, \\
{}^{E}\mathcal{C}_1^{(0)} &= 0, \\
{}^{E}\mathcal{C}_2^{(0)} &= \tau'\sqrt{6}P^0, \\
{}^{E}\mathcal{C}_1^{(1)} &= 0, \\
{}^{E}\mathcal{C}_2^{(1)} &= \tau'\sqrt{6}P^1, \\
{}^{E}\mathcal{C}_2^{(2)} &= \tau'\sqrt{6}P^2,
\end{aligned}$$

where $P^m = (1/10)(\Theta_2^{(m)} - \sqrt{6}E_2^{(m)})$. Equations (3.94) – (3.97) are an infinite system of coupled first order differential equations.

In the temperature hierarchy, the terms within brackets describe the free streaming of photons in the universe. Free streaming suppresses the temperature fluctuations, as photons from hot and cold regions mix. The term $\tau'\Theta_\ell^{(m)}$, due to scattering, also suppresses the temperature fluctuations if τ' is large. While Thomson scattering damps $\ell > 1$ multipoles, it induces a dipole due to the electron bulk velocity.

Regarding polarization, one major difference from temperature is that polarization is a spin-2 field [52, 46], and the free streaming constants are modified to include this. Much like temperature fluctuations, free streaming acts to damp polarization. Thomson scattering, conversely, induces a quadrupole in the E mode — but it does not power the B mode, which are sourced by a "leakage" of E modes. Lastly, another piece of physics we lost in our simplified derivation because we ignored the angular dependency of the Thomson scattering is the temperature fluctuations conversion into E modes, contained in the quadrupole term of ${}^{\Theta}\mathcal{C}$. Note, however, that we did not perform this simplification in the implemented equations.

Generalizing this derivation to curved space is complicated, as there are no plane waves in curved space, so the decomposition described above cannot be performed. Nonetheless, it is still possible to find a basis like G_ℓ^m to decompose the observables [51, 50]. There are, however, more subtleties. As in the flat case, the harmonics themselves can be given in terms of G_ℓ^m, but there is additional freedom of coupling constants ζ_ℓ^m that will be important latter. Another important difference is the fact that the radial functions are given in terms of hyperspherical Bessel functions, generalizations of the spherical Bessel function to spaces with constant curvature. They are defined as the solutions to the equation [50, 53]

$$\frac{1}{r^2(\chi)}\frac{\mathrm{d}}{\mathrm{d}\chi}r^2(\chi)\frac{\mathrm{d}}{\mathrm{d}\chi}\Phi_\ell^\nu + \left[\nu^2 - \mathcal{K} - \frac{\ell(\ell+1)}{r^2(\chi)}\right]\Phi_\ell^\nu = 0, \tag{3.99}$$

where $\nu^2 \equiv k^2 + (1+|m|)K$ is the generalized Fourier mode.

The Boltzmann hierarchy is mostly the same in curved space. The major difference is in the free streaming coefficients. The objects ${}_s\kappa_\ell^m$ become [16]

$${}_s\kappa_\ell^m = \sqrt{\frac{(\ell^2 - m^2)(\ell^2 - s^2)}{\ell^2}}\sqrt{\nu^2 - \mathcal{K}\ell} \tag{3.100}$$

and the freedom to add the coupling constants ζ_ℓ^m, which we exploit to make the connection with Bianchi cosmologies, changes the free streaming coefficients as [50]

$$\begin{aligned} {}_s\kappa_\ell^m &\to {}_s\kappa_\ell^m \frac{\zeta_\ell^m}{\zeta_{\ell-1}^m} \\ {}_s\kappa_{\ell+1}^m &\to {}_s\kappa_{\ell+1}^m \frac{\zeta_\ell^m}{\zeta_{\ell+1}^m}. \end{aligned}$$

Expressions for ζ_ℓ^m depend on the Bianchi model, and will be provided in the next chapter.

3.6.3 Line-of-sight integral solution

Equations (3.94) – (3.97) encompass the major physical processes that affect the CMB fluctuations. Given some initial conditions, one can compute the fluctuations today. However, the fact that the system is not finite adds another layer of complexity. It is necessary to find a method to truncate the hierarchy in some multipole, but this adds an error that propagates back to all lower multipoles. If one wants to study small scale fluctuations — say around $\ell = 2000$ —, one would need to compute the hierarchy for even larger multipoles to minimize the truncation error. This usually demands too much power capacity from computers, so it is not an efficient method. Luckily, the Boltzmann hierarchy has an integral solution [17]. From equation (3.75), we see that

$$\frac{\mathrm{d}\Theta}{\mathrm{d}\eta} = \tau'\Theta + {}^{\Theta}\mathcal{C} + \mathcal{G}. \tag{3.101}$$

This has an integral solution

$$\Theta(\eta_0, \hat{\boldsymbol{p}}) = \int_0^{\eta_0} \mathrm{d}\eta e^{-\tau}({}^{\Theta}\mathcal{C} + \mathcal{G}). \tag{3.102}$$

Expanding both sides in terms of G_ℓ^m,

$$\sum_{\ell m}(-i)^\ell\sqrt{\frac{4\pi}{2\ell+1}}\Theta_\ell^{(m)}Y_\ell^m(\hat{\boldsymbol{p}}) = \int_0^{\eta_0} \mathrm{d}\eta e^{-\tau}\sum_{jm'}({}^{\Theta}\mathcal{C}_j^{(m')}+\mathcal{G}_j^{(m')})\sum_{\ell'}(-i)^{\ell'}\sqrt{4\pi(2\ell'+1)}j_{\ell'}^{(jm')}Y_{\ell'}^{m'}(\hat{\boldsymbol{p}}).$$

Now, using the orthogonality of the spherical harmonics, we find

$$\frac{\Theta_\ell^{(m)}}{2\ell+1} = \int_0^{\eta_0} \mathrm{d}\eta e^{-\tau}\sum_j({}^{\Theta}\mathcal{C}_j^{(m)} + \mathcal{G}_j^{(m)})j_\ell^{(jm)}(k\chi). \tag{3.103}$$

This equation is valid for the flat case. In the curved case, the line-of-sight integrals for the temperature fluctuations and polarization become [16]

$$\frac{\Theta_\ell^{(m)}}{2\ell+1} = \int_0^{\eta_0} \mathrm{d}\eta e^{-\tau}\sum_j({}^{\Theta}\mathcal{C}_j^{(m)} + \mathcal{G}_j^{(m)})\frac{\zeta_\ell^m}{\zeta_j^m}\,{}_0\epsilon_\ell^{(jm)}(k\chi) \tag{3.104}$$

$$\frac{E_\ell^{(m)}}{2\ell+1} = \int_0^{\eta_0} \mathrm{d}\eta e^{-\tau}\sum_j {}^{E}\mathcal{C}_j^{(m)}\frac{\zeta_\ell^m}{\zeta_j^m}\,{}_2\epsilon_\ell^{(jm)}(k\chi) \tag{3.105}$$

$$\frac{B_\ell^{(m)}}{2\ell+1} = \int_0^{\eta_0} \mathrm{d}\eta e^{-\tau}\sum_j {}^{E}\mathcal{C}_j^{(m)}\frac{\zeta_\ell^m}{\zeta_j^m}\,{}_2\beta_\ell^{(jm)}(k\chi). \tag{3.106}$$

The integrands ${}^{\Theta}\mathcal{C}_j^{(m)} + \mathcal{G}_j^{(m)}$ and ${}^{E}\mathcal{C}_j^{(m)}$ are called source terms. They only depend on the monopole, dipole, and quadrupole of the fluctuations. This means that, instead of solving the hierarchy for large multipoles, it is possible to solve it up to a value that leads to a small propagating error in the first few multipoles (around $\ell_{\text{trunc}} = 30$) and then use them as sources to the integral solution. This is a much more efficient method.

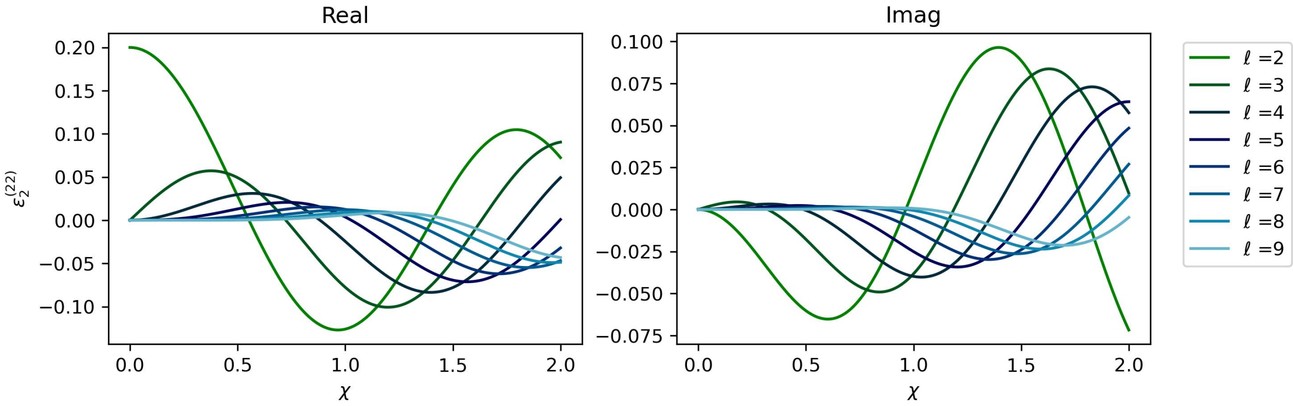

Figure 8: Function ${}_2\epsilon_\ell^{(2,2)}$ calculated using the hyperspherical Bessel function routines for various values of χ and ℓ. We set $\nu = 4 + i$ to create this graphic.

The radial functions ${}_s\epsilon_\ell^{(jm)}$ and ${}_2\beta_\ell^{(jm)}$ are defined in [16]. Explicitly, for vector modes:

$$ {}_0\epsilon_\ell^{(11)} = \sqrt{\frac{\ell(\ell+1)}{2(\nu^2-\mathcal{K})}}\frac{\Phi_\ell^\nu}{r} \tag{3.107}$$

$$ {}_0\epsilon_\ell^{(21)} = \sqrt{\frac{3\ell(\ell+1)}{2(\nu^2-\mathcal{K})(\nu^2-4\mathcal{K})}}\frac{\mathrm{d}}{\mathrm{d}\chi}\left(\frac{\Phi_\ell^\nu}{r}\right) \tag{3.108}$$

$$ {}_2\epsilon_\ell^{(21)} = \sqrt{\frac{(\ell+2)(\ell-1)}{4r^4(\nu^2-\mathcal{K})(\nu^2-4\mathcal{K})}}\frac{\mathrm{d}}{\mathrm{d}\chi}\left(r\Phi_\ell^\nu\right) \tag{3.109}$$

$$ {}_2\beta_\ell^{(21)} = -\sqrt{\frac{(\ell+2)(\ell-1)}{4(\nu^2-\mathcal{K})(\nu^2-4\mathcal{K})}}\frac{\nu\Phi_\ell^\nu}{r}. \tag{3.110}$$

And for tensor modes:

$$ {}_0\epsilon_\ell^{(22)} = \sqrt{\frac{3(\ell+2)!}{8(\nu^2-\mathcal{K})(\nu^2-4\mathcal{K})(\ell-2)!}}\frac{\Phi_\ell^\nu}{r} \tag{3.111}$$

$$ {}_2\epsilon_\ell^{(22)} = \sqrt{\frac{1}{16(\nu^2-\mathcal{K})(\nu^2-4\mathcal{K})}}\left[\frac{\mathrm{d}^2}{\mathrm{d}\chi^2} + 4\mathfrak{cot}(\chi)\frac{\mathrm{d}}{\mathrm{d}\chi} + 2\mathfrak{cot}^2(\chi) - (\mathcal{K}+\nu^2)\right]\Phi_\ell^\nu \tag{3.112}$$

$$ {}_2\beta_\ell^{(21)} = -\frac{\nu}{2r^2}\sqrt{\frac{1}{(\nu^2-\mathcal{K})(\nu^2-4\mathcal{K})}}\frac{\mathrm{d}(r^2\Phi_\ell^\nu)}{\mathrm{d}\chi}, \tag{3.113}$$

where $\mathfrak{cot}(\chi) = \cot(\chi)$ for $\mathcal{K} = +1$ and $\mathfrak{cot}(\chi) = \coth(\chi)$ for $\mathcal{K} = -1$. See Figures 8 for illustrations of the radial functions in an open universe.

Finally, it is usual to expand the observed temperature fluctuations $\Theta(\hat{\boldsymbol{p}})$ into spherical harmonics in the sky,

$$\Theta(\hat{\boldsymbol{p}}) = \sum_{\ell,m} a_{\ell m}^\Theta Y_{\ell m}(\hat{\boldsymbol{p}}). \tag{3.114}$$

From equation (3.79), we see that, in flat space at the origin $\boldsymbol{x} = 0$,

$$Y_\ell^m(\hat{\boldsymbol{p}}) = i^\ell G_\ell^m \sqrt{\frac{2\ell+1}{4\pi}}, \tag{3.115}$$

such that the harmonic coefficients $a_{\ell m}^{\Theta}$ relate with $\Theta_\ell^{(m)}$ by the equation

$$a_{\ell m}^{\Theta} = (-i)^\ell \sqrt{\frac{4\pi}{2\ell+1}} \Theta_\ell^{(m)}. \tag{3.116}$$

The equation above also holds for curved space [16].

The intention of our work is to obtain the multipoles (3.116) in the context of nearly isotropic Bianchi cosmologies for vector and tensor modes. Thus, we must implement numerically the line-of-sight integrals (3.104) – (3.106). These integrals require the source terms ${}^{\Theta}\mathcal{C}_j^{(m)} + \mathcal{G}_j^{(m)}$ and ${}^{E}\mathcal{C}_j^{(m)}$ and the radial functions (3.107) to (3.113).

In summary, this chapter built the theory of linear perturbations in cosmology and the equations that govern the physics of the CMB. In the next chapter, we will relate nearly isotropic Bianchi models with perturbations in FLRW, allowing us to use this framework to evolve anisotropies in Bianchi, and, more importantly, it will offer us a framework to understand how intrinsic anisotropies affect the photons of the CMB.

4 BIANCHI MODELS

This chapter discusses Bianchi models, a class of homogeneous cosmological models. They relax the Cosmological Principle by dropping the isotropy requirement. In these models, the spatial hypersurfaces are isomorphic to three-dimensional simply-connected Lie Groups, which leads to a method for systematically characterizing these cosmologies. A subclass of Bianchi models contains FLRW cosmologies as limiting cases, thus allowing for small anisotropy regimes at any given time. These nearly-isotropic Bianchi models are our major interest in this work, as they offer a simple method to test the Cosmological Principle.

The structure of this chapter is as follows: section 4.1 reviews the theory of Lie Groups and Lie Algebras. Note that we present an informal review of this very abstract subject. This section is based on references [22, 25, 54, 55]. Section 4.2 covers some details about the Bianchi Classification of homogeneous cosmological models. In sections 4.3, 4.4, and 4.5, we focus on nearly isotropic Bianchi models and their matching with homogeneous FLRW perturbations. Finally, in section 4.6, we discuss the non-decaying initial conditions for vector and tensor modes.

4.1 Lie Groups and Lie Algebras

The theory of continuous symmetries plays an important role in describing homogeneous cosmological models. Briefly, the presence of translation symmetries generates isometries in each manifold Σ_t. In general, the set of isometries, $\mathrm{Isom}(\Sigma_t)$, form an isomorphic group to a three-dimensional Lie Group. This introduces a map between points in the manifold and elements of the group, such that a subclass of homogeneous spaces is isomorphic to Lie Groups. In turn, this leads to a major simplification in the description of homogeneous spaces, as Lie Groups are related to Lie Algebras, which are nothing more than vector spaces with a binary operator. Thus, classifying the possible three-dimensional Lie Algebras is equivalent to classifying the majority of homogeneous spaces[12]. In the following, we will detail this process.

We start off with the definitions of Lie Groups and Lie Algebras. A Lie Algebra is a vector space $\mathcal{G}$ armed with a bilinear map $[\cdot,\cdot] : \mathcal{G} \times \mathcal{G} \to \mathcal{G}$ satisfying the following properties

- Antisymetry: Given $\boldsymbol{a}, \boldsymbol{b} \in \mathcal{G}$

$$[\boldsymbol{a}, \boldsymbol{b}] = -[\boldsymbol{b}, \boldsymbol{a}]. \tag{4.1}$$

- Linearity: $\boldsymbol{a}, \boldsymbol{b}, \boldsymbol{c} \in \mathcal{G}$

$$[\boldsymbol{a} + \boldsymbol{b}, \boldsymbol{c}] = [\boldsymbol{a}, \boldsymbol{c}] + [\boldsymbol{b}, \boldsymbol{c}]. \tag{4.2}$$

- Jacobi Identity: $\boldsymbol{a}, \boldsymbol{b}, \boldsymbol{c} \in \mathcal{G}$

$$[\boldsymbol{a}, [\boldsymbol{b}, \boldsymbol{c}]] + [\boldsymbol{c}, [\boldsymbol{a}, \boldsymbol{b}]] + [\boldsymbol{b}, [\boldsymbol{c}, \boldsymbol{a}]] = 0. \tag{4.3}$$

---

[12] The exception is the Kantowski-Sachs model, a homogeneous and anisotropic cosmological model where the isometries form a multiply-transitively acting group.

A Lie Group G is a group which is also a differentiable manifold such that the multiplication and inverse maps

$$\begin{aligned} \mu :& G \times G \to G & \qquad i : G \to G \\ &(g, g') \mapsto gg' & \qquad g \mapsto g^{-1} \end{aligned}$$

are smooth.

Lie Groups possess objects called left-translation maps ℓ_g: given $g, g' \in G$, $\ell_g g' = gg'$. They map elements of the group to other elements of the group by a "left multiplication", meaning that $\ell_g = \mu(g, \cdot)$. Analogously, there are right-translation maps, $r_g g' = g'g$, such that $r_g = \mu(\cdot, g)$. They induce maps — ℓ^*_g and r^*_g — between the tangent spaces at each point in G.

There are vector fields v^μ in G that are invariant under the map ℓ^*_g,

$$(\ell^*_g v)^\mu|_p = v^\mu|_{gp}, \tag{4.4}$$

They are called left-invariant. Their value everywhere is completely characterized by their value in the identity element e,

$$v^\mu|_p = (\ell^*_p v)^\mu|_e. \tag{4.5}$$

Similarly, there are right-invariant vector fields with analogous properties. Given the linearity of the push-forward map, the left-invariant and the right-invariant vector fields form vector spaces $L(G)$ and $R(G)$. Since all left-invariant and right-invariant vector fields are completely characterized by their value at the identity, $L(G)$ and $R(G)$ are isomorphic to T_eG. In particular, this means they have the same dimension as G [25].

The commutator[13] of two left-invariant vector fields is also a left-invariant vector field. That is, given v^μ and $w^\mu \in L(G)$, [55]

$$\ell^*_g[\boldsymbol{v}, \boldsymbol{w}]|_p = [\boldsymbol{v}, \boldsymbol{w}]|_{gp}. \tag{4.6}$$

Since the commutator of two left-invariant fields is also a left-invariant field, given a basis $\{\boldsymbol{E}_i\}$, $i = 1, ..., \dim G$ for $L(G)$, the commutator can be written as

$$[\boldsymbol{E}_i, \boldsymbol{E}_j] = C^k{}_{ij} \boldsymbol{E}_k, \tag{4.7}$$

where $C^k{}_{ij}$ are called structure constants. As commutators are antisymmetric and satisfy the Jacobi Identity, the structure constants satisfy the conditions: $C^k{}_{ij} = C^k{}_{[ij]}$ and $C^b{}_{a[i} C^a{}_{jk]} = 0$. Moreover, due to the linearity of the commutator,

$$[\boldsymbol{v}, \boldsymbol{w}] = v^i w^j C^k{}_{ij} \boldsymbol{E}_k, \tag{4.8}$$

---

[13] For a definition, see [22].

so the commutator of any two left-invariant vector fields will be a linear combination of $C^k{}_{ij}$.

Due to the properties of the commutator, it is clear that $L(G)$ is a Lie Algebra. Since $R(G)$ and $L(G)$ are isomorphic, $R(G)$ is the same Lie Algebra as $L(G)$. The Lie Algebra $L(G)$ is defined as *the* Lie Algebra of the group G, and it is unique. Furthermore, the converse is true: a Lie Algebra generates a unique simply-connected[14] Lie Group [54].

4.2 Bianchi Models

As previously stated, the connection between homogeneous spaces and Lie Groups arises because isometries form a continuous group of transformations in the manifold. In this case, there is a one-to-one map between group elements g and isometries $\gamma_g : \Sigma_t \to \Sigma_t$ such that G and $\mathrm{Isom}(\Sigma_t)$ are homomorphic. The set of isometries must satisfy $\gamma_e(p) = p$ and $\gamma_{g_2}\gamma_{g_1} = \gamma_{g_2 g_1}$. Thus the group is said to *act on the left*[15]. If, for any point $p \in \Sigma_t$, there are isometries that map p to $q, \forall q \in \Sigma_t$, then the action of the group is transitive. By the previous chapter, if the space is homogeneous, then the action of the group is indeed transitive. Moreover, the group action is simply-transitive if, besides being transitive, $\gamma_g(p) = q = \gamma_{g'}(p)$ implies that $g = g'$ (that is, there is a single group element that connects two points in the manifold).

Fixing a reference point p and assuming that the isometry group acts simply-transitively, the map $\gamma_g(p) : G \to \Sigma_t$, $g \mapsto \gamma_g(p)$ is a one-to-one correspondence between the Lie Group and the manifold Σ_t (since the space is homogeneous, the choice of p is arbitrary). See Figure 9. This means that classifying homogeneous spaces is equivalent to classifying three-dimensional simply-connected Lie Groups, which, in turn, can be achieved by determining the independent sets of structure constants. The classification of three-dimensional Lie Algebras (see Table 2) was first performed by Bianchi in 1898, thus justifying the name “Bianchi models”.

The map $\gamma_g(p)$ induces a push-forward such that the right-invariant vector fields[16] are associated with the infinitesimal generators of isometries in Σ_t, the Killing vector fields. Since there is a one-to-one correspondence between KVFs and right-invariant vector fields, the KVFs form a Lie Algebra and, thus, there are sets of three independent KVFs that satisfy the algebra

$$[\boldsymbol{\xi}_a, \boldsymbol{\xi}_b] = C^m{}_{ab}\boldsymbol{\xi}_m. \tag{4.9}$$

The above structure constants are then determined for each Bianchi model.

The Bianchi Classification is achieved by writing the tensor $C^k{}_{ij}$ in (4.9) as

$$C^k{}_{ij} = \epsilon_{ijl}N^{lk} - A_i\delta^k{}_j + A_j\delta^k{}_i, \tag{4.10}$$

---

[14] A simply-connected manifold is a manifold where every closed continuous curve can be deformed into a point. See [22] for a formal definition.

[15] We could have chosen a *right action* as well, in which $\gamma_{g_2}\gamma_{g_1} = \gamma_{g_1 g_2}$.

[16] Right-invariant vector fields generate left-translations in G. For a proof, see [25].

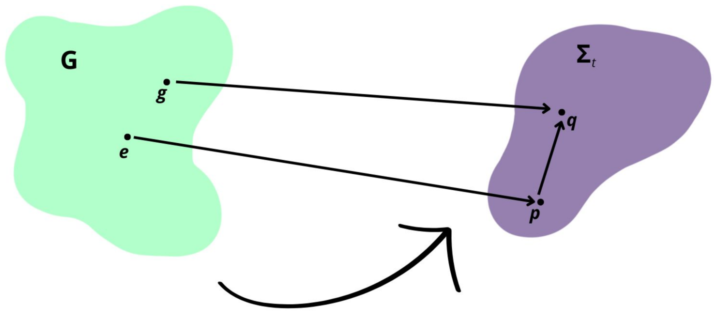

Figure 9: The connection between Lie Groups and homogeneous spaces. The element e is mapped to $\gamma_e(p) = p$ and g is mapped to $\gamma_g(p) = q$.

where N^{lk} is symmetric. From the Jacobi Identity, it follows that

$$N^{ij} A_j = 0. \tag{4.11}$$

By linear transformations of the set $\{\boldsymbol{\xi}_i\}$, $\boldsymbol{\xi}_i \to M_i{}^a \boldsymbol{\xi}_a$, the structure constants transform as $C^k{}_{ij} \to M_i{}^a M_j{}^b (M^{-1})_c{}^k C^c{}_{ab}$. Hence, it is possible to find a set of $M_i{}^a$ such that N^{ij} is diagonal, diag(N^1, N^2, N^3), and, since A^i is either the null-vector or an eigenvector of N^{ij}, it can be set to $(0, 0, A)$ without lost of generality. Bianchi models are usually split into two categories: $A = 0$ and $A \neq 0$. In both cases, the models are determined by the rank of N^{ij} and the relative signs between the eigenvalues. There are 6 combinations in the first case, and 4 in the second, as $N^3 = 0$.

For the two models where N^1, N^2, and A are non-zero, it is not possible to normalize all three parameters. To see this, notice that $C^1_{23} = N^1$, $C^2_{31} = N^2$, and $C^2_{23} = A$. Under a transformation $\boldsymbol{\xi}_i \to \tilde{\boldsymbol{\xi}}_i = S_{(i)} \boldsymbol{\xi}_i$, where $S_{(i)} > 0$ (the parenthesis on the index is to indicate that there is no implicit sum), the structure constants transform as $C^k{}_{ij} \to \tilde{C}^k{}_{ij} = (S_{(i)} S_{(j)} / S_{(k)}) C^k{}_{ij}$. Imposing that $\tilde{N}^1 = \pm 1$ and $\tilde{N}^2 = \pm 1$ fixes $\tilde{A} = |N^1 N^2|^{-1/2} A$. In other words, these models give rise to families of models historically parametrized by h, defined as

$$h \equiv \frac{(A)^2}{N^1 N^2}. \tag{4.12}$$

Table 2 presents all possible Bianchi spaces.

After classifying this class of homogeneous cosmological models, the next step is to exploit the remaining translation symmetry to write down the metric in a convenient way. In principle, we could use the dual of the KVFs as the basis for the spatial part of the metric, but the resulting metric components will in general depend on the point, hiding the translational

Type	A	N^1	N^2	N^3
I	0	0	0	0
II	0	0	0	$+$
IV	$+$	$+$	0	0
V	$+$	0	0	0
VI$_0$	0	$-$	$+$	0
VI$_h$	$+$	$-$	$+$	0
VII$_0$	0	$+$	$+$	0
VII$_h$	$+$	$+$	$+$	0
VIII	0	$-$	$+$	$+$
IX	0	$+$	$+$	$+$

Table 2: Bianchi Classification of homogeneous models. Note that Bianchi III belongs to the family Bianchi VI$_h$ with $h = -1$.

symmetry. A better solution is to build a vector and dual basis field, $\{\boldsymbol{e}_i\}$ and $\{\boldsymbol{\omega}^i\}$, to make the components of the metric in this basis independent of point in the hypersurface. This can be achieved by choosing an arbitrary point p, choosing a vector basis in its tangent space — $(\boldsymbol{e}_i)|_p = (\boldsymbol{\xi}_i)|_p$, for example — and then dragging it everywhere through the Killing vector fields,

$$\mathcal{L}_{\boldsymbol{\xi}_j}\boldsymbol{e}_i = \left[\boldsymbol{e}_i, \boldsymbol{\xi}_j\right] = 0. \tag{4.13}$$

This determines the spatial part of the metric in one slice Σ_t. The metric of the whole spacetime is simply

$$\boldsymbol{g} = -\mathrm{d}t \otimes \mathrm{d}t + g_{ij}(t)\boldsymbol{\omega}^i \otimes \boldsymbol{\omega}^j, \tag{4.14}$$

where $\{\boldsymbol{e}_i\}$ is known as the *invariant basis*, $\boldsymbol{\omega}^i$ must satisfy $[\mathrm{d}t, \boldsymbol{\omega}^i] = 0$, and $g_{ij}(t) = \boldsymbol{g}(\boldsymbol{e}_i, \boldsymbol{e}_j)$.

In the basis $\{\boldsymbol{\omega}^i\}$, the spatial part of the metric has constant components on the hypersurface. It is convenient to decompose the expansion described by the metric into isotropic and anisotropic parts. A global scale factor $a(t)$ describes the isotropic contribution, $g_{ij} = a^2(t)\tilde{g}_{ij}(t)$, such that $\tilde{g}^i{}_i = 3$. It is usual to define $\tilde{g}_{ij}$ in terms of a symmetric, trace-free tensor β_{ij},

$$\tilde{g}_{ij} = [\exp(2\beta)]_{ij}. \tag{4.15}$$

The spatial anisotropies in Bianchi universes can be described in terms of the shear tensor σ_{ij} defined in chapter 1 using the extrinsic curvature tensor — equations (1.21) and (1.22). Recalling that $u_\mu = -(\mathrm{d}t)_\mu$, we see that

$$\nabla_i u_j = \frac{1}{2}\dot{g}_{ij}. \tag{4.16}$$

Taking the STF part of the equation (4.16) leads to the shear,

$$\sigma_{ij} = \frac{a^2}{2}\frac{\partial \tilde{g}_{ij}}{\partial t}, \tag{4.17}$$

or, equivalently, to the conformal shear $\tilde{\sigma}_{ij} \equiv a^{-1}\sigma_{ij}$,

$$\tilde{\sigma}_{ij} = \frac{\tilde{g}'_{ij}}{2}. \tag{4.18}$$

4.3 BIANCHI MODELS WITH ISOTROPIC LIMIT

Not all Bianchi models allow for arbitrarily small perturbations at all times. An intuitive approach to finding the Bianchi models that contain FLRW as a limit and derive their Killing vector fields was developed in [15]. In short, this method consists of explicitly breaking the rotation symmetry in known FLRW geometries. This computation can be understood in a series of steps:

1. We start by identifying, for each FLRW geometry, six independent Killing vectors and placing them into two sets of three vectors each, $\{\boldsymbol{T}_i\}$ and $\{\boldsymbol{R}_i\}$, $i = 1, 2, 3$, based on whether they generate translations or rotations in an arbitrarily chosen reference point p. In general, the translation vectors do not form a closed algebra;
2. Our wish is to find three Killing vector Fields $\{\boldsymbol{\xi}_i\}$ that form a closed algebra $[\boldsymbol{\xi}_i, \boldsymbol{\xi}_j] = C^k{}_{ij}\boldsymbol{\xi}_k$, where $C^k{}_{ij}$ is taken to be a particular structure constant in Table 2. This set will be the KVFs in a particular Bianchi model;
3. Since a linear combination of Killing vector fields is also a Killing vector field, we can write $\boldsymbol{\xi}_i = \boldsymbol{T}_i + \rho_i{}^j\boldsymbol{R}_j$ and find the constants $\rho_i{}^j$ that give the commutation relation we impose.

In what follows, we will perform this process in detail for each curvature $\mathcal{K}$. Table 3 gives the Bianchi models with isotropic limits.

Type	A	N^1	N^2	N^3	$\mathcal{K}$
I	0	0	0	0	0
V	ℓ_c^{-1}	0	0	0	-1
VII$_0$	0	ℓ_s^{-1}	ℓ_s^{-1}	0	0
VII$_h$	ℓ_c^{-1}	ℓ_s^{-1}	ℓ_s^{-1}	0	-1
IX	0	$2\ell_c^{-1}$	$2\ell_c^{-1}$	$2\ell_c^{-1}$	1

Table 3: Bianchi Classification of the homogeneous models that contain FLRW. The last column shows which FLRW model each type has as a limiting case. The parameter ℓ_s is called spiraling length, and its meaning will be made clear in a bit.

4.3.1 Flat space

Let us start with the simple case of Euclidean geometries ($\mathcal{K} = 0$). In this space, the translation and rotation vectors are simply $\boldsymbol{T}_i = \partial_i$ and $\boldsymbol{R}_i = \epsilon_{ijk}x^j\partial_k$. The commutation relations are[17]

$$[\boldsymbol{T}_i, \boldsymbol{T}_j] = 0,$$
$$[\boldsymbol{R}_i, \boldsymbol{R}_j] = -\epsilon_{ijk}\boldsymbol{R}_k,$$
$$[\boldsymbol{R}_i, \boldsymbol{T}_j] = -\epsilon_{ijk}\boldsymbol{T}_k.$$

We immediately see that the translation vectors form a closed algebra with structure constant $C^k{}_{ij} = 0$, which defines Bianchi I. Therefore, the three Killing vector fields in this model are simply $\boldsymbol{\xi}_i = \partial_i$, and, since $[\partial_i, \partial_j] = 0$, the invariant basis vectors are $\boldsymbol{e}_i = \partial_i$.

To obtain the other Bianchi models that contain flat FLRW geometry, we substitute $\boldsymbol{T}_i + \rho_i{}^j\boldsymbol{R}_j$ in (4.9) for each possible algebra and solve for constants $\rho_i{}^j$. That is, we look for solutions to the system of equations

$$C^k{}_{ij} = \rho_j{}^a\epsilon_{iak} - \rho_i{}^a\epsilon_{ajk} \tag{4.19}$$
$$C^n{}_{ij}\rho_n{}^m\epsilon_{mka} = \rho_i{}^a\rho_j{}^k - \rho_i{}^k\rho_j{}^a. \tag{4.20}$$

The first equation can be used to obtain $\rho_i{}^j$ in terms of N^1, N^2, N^3, and A, and the second is a consistency relation. The only Bianchi model (besides Bianchi I) that allow for existing $\rho_i{}^j$ satisfying this system is Bianchi VII$_0$. With the constants $\rho_i{}^j$ in hands, the KVFs of Bianchi VII$_0$ follow imediately:

$$\boldsymbol{\xi}_1 = \partial_1$$
$$\boldsymbol{\xi}_2 = \partial_2$$
$$\boldsymbol{\xi}_3 = \partial_3 - \ell_s^{-1}\boldsymbol{R}_3.$$

This set generates translations that are isometries in Bianchi VII$_0$. We see that the integral curves generated by $\boldsymbol{\xi}_3$ have parametric equation

$$x(s) = A_x \sin\left(\frac{s}{\ell_s}\right) + B_x \cos\left(\frac{s}{\ell_s}\right)$$
$$y(s) = A_y \sin\left(\frac{s}{\ell_s}\right) + B_y \cos\left(\frac{s}{\ell_s}\right)$$
$$z(s) = s + z_0,$$

where $x = x^1$, $y = x^2$ and $z = x^3$. This illustrates why ℓ_s is called spiraling length. If ℓ_s is small, for small variations of s (and hence z), x and y significantly oscillate (see Figure 10).

The invariant basis in this model is obtained by solving the equation $[\boldsymbol{e}_i, \boldsymbol{\xi}_i] = 0$, with

---

[17] Since we are working on $\mathbb{E}^3$, there is no distinction between objects with indices raised or lowered.

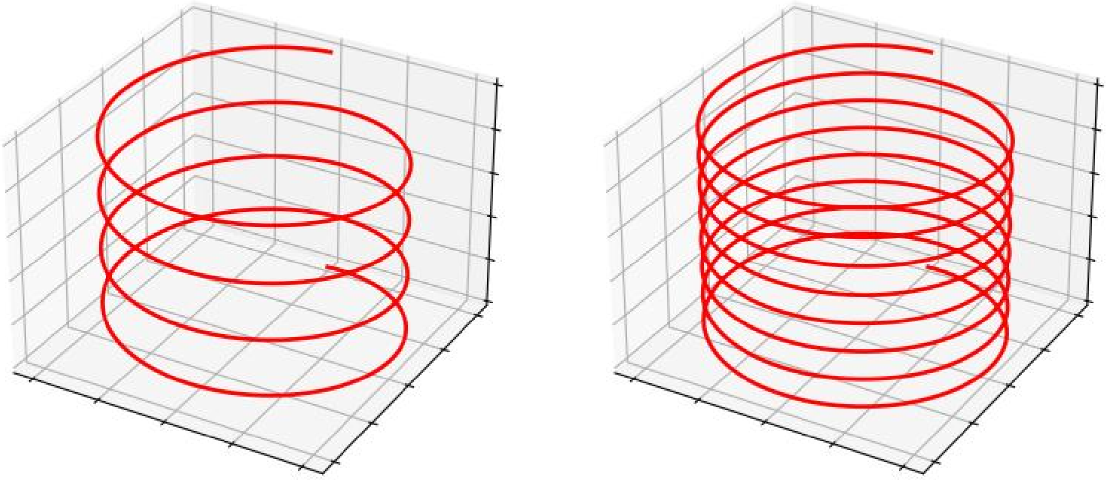

(a) (b)

Figure 10: Integral lines from a Killing vector field in Bianchi VII_0 with $A_x = B_y = 1$, $A_y = B_x = 0$, and a) $\ell_s = 1$ b) $\ell_s = 0.5$.

$\boldsymbol{e}_i|_p = \boldsymbol{\xi}_i|_p$; we have

$$\begin{aligned}\boldsymbol{e}_1 &= \cos(z/\ell_s)\partial_x - \sin(z/\ell_s)\partial_y\\ \boldsymbol{e}_2 &= \sin(z/\ell_s)\partial_x + \cos(z/\ell_s)\partial_y\\ \boldsymbol{e}_3 &= \partial_z.\end{aligned}$$

4.3.2 Closed space

This section is based on reference [56]. Curved space models are treated by considering them as hypersurfaces in a higher-dimension space. For $\mathcal{K} = 1$, the 3-sphere $\mathbb{S}^3$ is embedded in $\mathbb{E}^4$, which has the metric

$$\mathrm{d}s^2 = \mathrm{d}\big(x^0\big)^2 + \mathrm{d}\big(x^1\big)^2 + \mathrm{d}\big(x^2\big)^2 + \mathrm{d}\big(x^3\big)^2 \tag{4.21}$$

and $\mathbb{S}^3$ is defined by the condition

$$\ell_c^2 = (x^0)^2 + (x^1)^2 + (x^2)^2 + (x^3)^2. \tag{4.22}$$

The Euclidean space $\mathbb{E}^4$ has six generators of rotation and four generators of translations about each point, which are the ten independent Killing vector fields of this space. Since rotations preserve distances, the six rotations map points in $\mathbb{S}^3$ into points in $\mathbb{S}^3$. Therefore, the rotation generators in $\mathbb{E}^4$ are the six Killing vector fields at $\mathbb{S}^3$. Rotations in four dimensions are specified

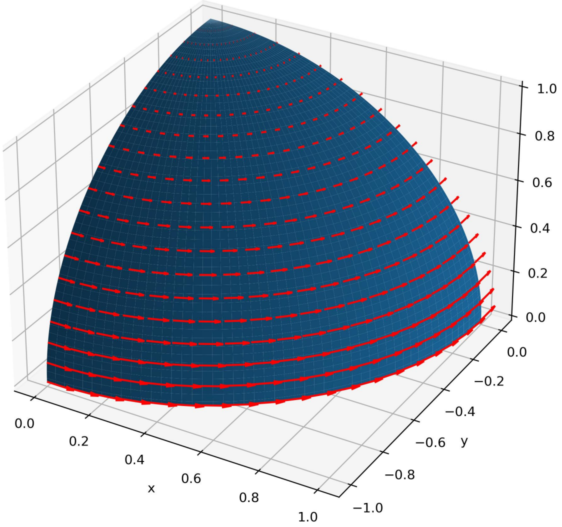

Figure 11: Rotation about the z axis in $\mathbb{S}^2$. The arrows represent the intensity and direction of the transformation at each point. Note that the pole is fixed. Therefore, in $\mathbb{S}^2$, the rotations about the z axis are the generators of rotation about $(0, 0, \ell_c)$, as they leave this point unchanged but act on the others. This is analogous to the discussion on $\mathbb{S}^3$.

by an angle and a plane. The generator of infinitesimal rotations over a plane $x_\mu x_\nu$ is

$$\boldsymbol{\mathcal{R}}_{(\mu\nu)} = \epsilon_{\mu\nu\alpha\beta} x^\alpha \partial_\beta, \tag{4.23}$$

such that the generators of rotation form a set $\{\boldsymbol{\mathcal{R}}_{(01)}, \boldsymbol{\mathcal{R}}_{(02)}, \boldsymbol{\mathcal{R}}_{(03)}, \boldsymbol{\mathcal{R}}_{(12)}, \boldsymbol{\mathcal{R}}_{(13)}, \boldsymbol{\mathcal{R}}_{(23)}\}$. A vector $\boldsymbol{\mathcal{R}}_{(\mu\nu)}$ maps a point with coordinates x^α to x'^α as

$$x'^\alpha = x^\alpha + \delta\theta \mathcal{R}^\alpha_{(\mu\nu)}.$$

Choosing as reference the point p with coordinates $x^0 = \ell_c$, $x^i = 0$, we distinguish translations from rotations based on how $\boldsymbol{\mathcal{R}}_{(\mu\nu)}$ acts in this point (see Figure 11),

$$\boldsymbol{\mathcal{R}}_{(\mu\nu)} = \epsilon_{\mu\nu0\beta} \ell_c \partial_\beta.$$

In this point, $\boldsymbol{\mathcal{R}}_{(i0)} = 0$. Hence, the generators of rotation in $\mathbb{S}^3$ (about p) are $\{\boldsymbol{\mathcal{R}}_{(01)}, \boldsymbol{\mathcal{R}}_{(02)}, \boldsymbol{\mathcal{R}}_{(03)}\}$, and the generators of translation are $\{\boldsymbol{\mathcal{R}}_{(12)}, \boldsymbol{\mathcal{R}}_{(13)}, \boldsymbol{\mathcal{R}}_{(23)}\}$. Thus, we make the following identification,

$$\boldsymbol{T}_i = \frac{1}{2\ell_c} \epsilon_{ijk} \boldsymbol{\mathcal{R}}_{(jk)} = \frac{1}{\ell_c}(x^0 \partial_i - x^i \partial_0) \tag{4.24}$$

and

$$\boldsymbol{R}_i = \boldsymbol{\mathcal{R}}_{(0i)} = \epsilon_{ijk} x^j \partial_k. \tag{4.25}$$

These vectors respect the following commutation relation

$$\begin{aligned}[\boldsymbol{R}_i, \boldsymbol{R}_j] &= -\epsilon_{ijk}\boldsymbol{R}_k,\\ [\boldsymbol{R}_i, \boldsymbol{T}_j] &= -\epsilon_{ijk}\boldsymbol{T}_k,\\ [\boldsymbol{T}_i, \boldsymbol{T}_j] &= -\frac{1}{\ell_c^2}\epsilon_{ijk}\boldsymbol{R}_k.\end{aligned}$$

As we can see, the translation vectors do not form a closed algebra. Following the procedure detailed in the previous section, we find that the only Bianchi model that contains closed FLRW is Bianchi IX. The KVFs in this space are

$$\boldsymbol{\xi}_i^{\pm} = \boldsymbol{T}_i \pm \ell_c^{-1}\boldsymbol{R}_i, \tag{4.26}$$

where the ± depends on the sign of the structure constants in Bianchi IX, $C^i_{jk} = \pm 2\ell_c^{-1}\epsilon_{ijk}$. Since $\left[\boldsymbol{\xi}_i^+, \boldsymbol{\xi}_i^-\right] = 0$, we may take $\boldsymbol{\xi}_i = \boldsymbol{\xi}_i^+$ and $\boldsymbol{e}_i = \boldsymbol{\xi}_i^-$ as invariant basis, subjected to the condition $\boldsymbol{e}_i = \boldsymbol{\xi}_i$ at p.

4.3.3 Open space

The open space model can be treated analogously to the closed case. For $\mathcal{K} = -1$, the maximally symmetric spatial surfaces are treated as hypersurfaces in a Minkowski space, with metric

$$\mathrm{d}s^2 = -\,\mathrm{d}\big(x^0\big)^2 + \mathrm{d}\big(x^1\big)^2 + \mathrm{d}\big(x^2\big)^2 + \mathrm{d}\big(x^3\big)^2, \tag{4.27}$$

where the hypersurface is defined by the condition

$$\ell_c^2 = (x^0)^2 - (x^1)^2 - (x^2)^2 - (x^3)^2. \tag{4.28}$$

Analogous to the closed case, the higher dimension space induces six rotation generators over each point (three rotations and three boosts). Rotations that leave the zeroth direction unchanged, $\boldsymbol{\mathcal{R}}_{(0i)}$, are purely "spatial" rotations, meaning that $\boldsymbol{\mathcal{R}}_{(0i)} = \epsilon_{ijk}x^j\partial_k$. Rotations that mix "time" and "space", on the other hand, are actually boosts. The infinitesimal generators of boosts can be obtained as follows: a boost in the $\hat{x}^1$ direction transforms a point with coordinate x^α as

$$\begin{pmatrix} x'^0 \\ x'^1 \\ x'^2 \\ x'^3 \end{pmatrix} = \begin{pmatrix} \cosh w & \sinh w & 0 & 0 \\ \sinh w & \cosh w & 0 & 0 \\ 0 & 0 & 1 & 0 \\ 0 & 0 & 0 & 1 \end{pmatrix} \begin{pmatrix} x^0 \\ x^1 \\ x^2 \\ x^3 \end{pmatrix}. \tag{4.29}$$

Taylor expanding with respect to the rapidity,

$$x'^\alpha = x^\alpha + \mathcal{R}^\alpha_{(23)}w, \tag{4.30}$$

where

$$\boldsymbol{\mathcal{R}}_{(23)} = x^1\partial_0 + x^0\partial_1 \tag{4.31}$$

is the infinitesimal generator of boosts in the $\hat{x}^1$ direction. Therefore, we have

$$\boldsymbol{\mathcal{R}}_{(ij)} = \epsilon_{ijk}(x^k\partial_0 + x^0\partial_k). \tag{4.32}$$

Taking the point with coordinates $x^0 = \ell_c$ as our reference point, we see that $\boldsymbol{\mathcal{R}}_{(0i)} = 0$ and $\boldsymbol{\mathcal{R}}_{(ij)} = \epsilon_{ijk}\ell_c\partial_k$ at this point. This implies that

$$\boldsymbol{R}_i = \boldsymbol{\mathcal{R}}_{(0i)} \tag{4.33}$$

and

$$\boldsymbol{T}_i = \frac{1}{2\ell_c}\epsilon_{ijk}\boldsymbol{\mathcal{R}}_{(jk)} = \frac{1}{\ell_c}(x^i\partial_0 + x^0\partial_i). \tag{4.34}$$

The commutators of these vectors are

$$\begin{aligned} [\boldsymbol{R}_i, \boldsymbol{R}_j] &= -\epsilon_{ijk}\boldsymbol{R}_k, \\ [\boldsymbol{T}_i, \boldsymbol{T}_j] &= \frac{1}{\ell_c^2}\epsilon_{ijk}\boldsymbol{R}_k, \\ [\boldsymbol{R}_i, \boldsymbol{T}_j] &= -\epsilon_{ijk}\boldsymbol{T}_k. \end{aligned}$$

Again, the translation vectors do not form a closed algebra. Following the prescriptions detailed earlier, we find that the only Bianchi models that contain open FLRW are V and VII$_h$. For these models, the Killing vectors and the invariant vector basis are [16]

- Bianchi V

$$\begin{aligned} \boldsymbol{\xi}_1 &= \boldsymbol{T}_1 + \ell_c^{-1}\boldsymbol{R}_2 \\ \boldsymbol{\xi}_2 &= \boldsymbol{T}_2 - \ell_c^{-1}\boldsymbol{R}_1 \\ \boldsymbol{\xi}_3 &= \boldsymbol{T}_3 \\ \boldsymbol{e}_1 &= e^{(z/\ell_c)}\partial_x \\ \boldsymbol{e}_2 &= e^{(z/\ell_c)}\partial_y \\ \boldsymbol{e}_3 &= \partial_z, \end{aligned}$$

where $x = e^{(z/\ell_c)}x^1$, $y = e^{(z/\ell_c)}x^2$, and $z = -\ell_c \ln(x^0 - x^3)$.

- Bianchi VII$_h$

$$\begin{aligned}
\boldsymbol{\xi}_1 &= \boldsymbol{T}_1 + \ell_c^{-1}\boldsymbol{R}_2\\
\boldsymbol{\xi}_2 &= \boldsymbol{T}_2 - \ell_c^{-1}\boldsymbol{R}_1\\
\boldsymbol{\xi}_3 &= \boldsymbol{T}_3 - \ell_s^{-1}\boldsymbol{R}_3\\
\boldsymbol{e}_1 &= \cos(z/\ell_s)e^{(z/\ell_c)}\partial_x - \sin(z/\ell_s)e^{(z/\ell_c)}\partial_y\\
\boldsymbol{e}_2 &= \sin(z/\ell_s)e^{(z/\ell_c)}\partial_x + \cos(z/\ell_s)e^{(z/\ell_c)}\partial_y\\
\boldsymbol{e}_3 &= \partial_z.
\end{aligned}$$

Given the invariant basis vectors $\{\boldsymbol{e}_i\}$ for each homogenous space, we can set the metric to the convenient form (4.14).

Note that the construction performed in this section is completely general for any Bianchi model with an isotropic limit. We simply identified each set of KVFs associated with some Bianchi models using symmetry considerations.

4.4 Nearly isotropic Bianchi models

Now we will specialize to the "almost isotropic" limit. This regime consists of linearizing the metric over β_{ij} in (4.15),

$$\tilde{g}_{ij} = \delta_{ij} + 2\beta_{ij}. \tag{4.35}$$

Then the conformal shear is

$$\tilde{\sigma}_{ij} = \beta'_{ij} \tag{4.36}$$

and the evolution equation for the shear (equation (1.11)) becomes [16]

$$\beta''_{ij} + 2\mathcal{H}\beta'_{ij} = \mathcal{S}_{ij}, \tag{4.37}$$

where $\mathcal{S}_{ij}$ is the anisotropic contribution to the spatial curvature. This term is linear on β_{ij}, and can be written as [16]

$$\mathcal{S}_{ij} = \mathcal{S}_{ijab}\beta_{ab}. \tag{4.38}$$

Equation (4.37) can be simplified even further. Similar to how perturbations in FLRW are decomposed into SVT modes based on how they transform under rotations around $\boldsymbol{k}$, the shear can also be decomposed in SVT parts. This is because the models have a residual symmetry due to the choice $\boldsymbol{A} \propto \boldsymbol{e}_3$, as the structure constants are preserved under rotations around $\boldsymbol{e}_3$. To illustrate this process, the simplest Bianchi model besides the trivial cases of Bianchi I and IX is model V. In this model, the structure constants are

$$C^k{}_{ij} = -A_i\delta^k_j + A_j\delta^k_i. \tag{4.39}$$

Under a rotation around $\boldsymbol{e}_3$, the vector $\boldsymbol{A}$ does not change, thus the structure constants are invariant in this model.

Recall in the previous chapter that each SVT mode was decomposed into harmonics $\boldsymbol{Q}^{(j,m)}$. Similarly, since the shear decouples into SVT modes, it can also be decomposed into tensor bases $q^{(0)}_{ij}$, $q^{(1)}_{ij}$, and $q^{(2)}_{ij}$. In the previous chapter, we introduced a polarization basis $\boldsymbol{m}^{\pm}$ such that the harmonics have simple components in this basis. Analogously, we introduce

$$e^{\pm}_i = \frac{1}{\sqrt{2}}(e^1_i \mp i e^2_i), \tag{4.40}$$

such that,

$$q^{(0)}_{ij} = -e^3_i e^3_j + \frac{\delta_{ij}}{3} \tag{4.41}$$

$$q^{(\pm 1)}_{ij} = \pm e^3_{(i} e^{\mp}_{j)} \tag{4.42}$$

$$q^{(\pm 2)}_{ij} = -\sqrt{\frac{3}{2}} e^{\mp}_i e^{\mp}_j . \tag{4.43}$$

Compare the equations above with (3.43), (3.42), and (3.78). Thus, the shear can be decomposed as

$$\beta_{ij} = \sum_{m=-2}^{2} \beta_{(m)} q^{(m)}_{ij} . \tag{4.44}$$

Moreover, we mentioned earlier that the anisotropic contribution to the spatial curvature is linear on the shear, which means it can be decomposed as

$$\mathcal{S}_{ij} = \sum_{m=-2}^{2} \mathcal{S}_{(m)} \beta_{(m)} q^{(m)}_{ij} . \tag{4.45}$$

In this context, the evolution equation for the shear decouples into independent modes

$$\beta''_{(m)} + 2\mathcal{H}\beta'_{(m)} = \mathcal{S}_{(m)}\beta_{(m)} . \tag{4.46}$$

The values of $\mathcal{S}_{(m)}$ for each Bianchi model are [16]

$$\mathcal{S}_{(0)} = \mathcal{S}_{(\pm 1)} = \begin{cases} 0, \text{ for types I, V, VII}_0\text{, and VII}_h; \\ -8\ell_c^{-2}, \text{ for type IX;} \end{cases}$$

$$\mathcal{S}_{(\pm 2)} = \begin{cases} 0, \text{ for types I and V;} \\ -4\ell_s^{-2}, \text{ for type VII}_0; \\ -4(\ell_s^{-2} \pm i(\ell_s\ell_c)^{-1}), \text{ for type VII}_h; \\ -8\ell_c^{-2}, \text{ for type IX.} \end{cases}$$

Due to the reality condition on β_{ij}, we only need to consider the positive modes, as the negative ones can be obtained from them.

In summary, the theory of linear perturbations in FLRW inspired us to decompose the shear into its own SVT modes. The vector $\boldsymbol{e}_3$ and the tensors $q_{ij}^{(m)}$ here took the role of $\boldsymbol{k}$ and $Q_{ij}^{(2,m)}$ there. This suggests that there is a deeper connection between nearly isotropic Bianchi models and standard perturbation theory, which we explore in the next section.

4.5 MATCHING PERTURBATIONS

We wish to mathematically identify β_{ij} with linear perturbations in FLRW in the limit where the later becomes homogeneous, as this would allow us to use the theory derived in the previous chapter in the context of Bianchi cosmologies. However, although equation (4.35) resembles the linear theory of metric perturbations developed in chapter 3, there are differences between a general perturbation $h_{\mu\nu}$ and β_{ij}.

First, in the basis that we introduced, the shear only has components in the spatial coordinates. In contrast, $h_{\mu\nu}$ is, in general, non-zero in the time and space-time components. Thus, the identification of β_{ij} with $h_{\mu\nu}$ happens in the synchronous gauge, where $h_{00} = h_{0i} = 0$. However, since β_{ij} is traceless and h_{ij} is not, we must further set $\phi = 0$ in equation (3.9). This means that β_{ij} is "equivalent" to E_{ij}.

Secondly, the usual metric perturbation E_{ij} is both anisotropic and inhomogeneous, while β_{ij} is a homogeneous tensor. Therefore, among all possible perturbations in FLRW, β_{ij} is only matched to the homogeneous ones, satisfying

$$\mathcal{L}_{\boldsymbol{\xi}} E_{ij} = 0. \tag{4.47}$$

This equation fixes the wavelength of the perturbation. This means that, mathematically, nearly isotropic Bianchi models are equivalent to perturbed FLRW universes that contain only homogeneous perturbations in a specific scale yet to be fixed. As a consequence, we can perform the matching:

$$\beta_{ij} = E_{ij} \qquad \Rightarrow \qquad \sum_{m=-2}^{2} \beta_{(m)} q_{ij}^{(m)} = \sum_{m=-2}^{2} E_{(m)} Q_{ij}^{(2,m)}. \tag{4.48}$$

In order to match the SVT modes of the shear with the SVT modes of the metric perturbation, the tensor bases $q_{ij}^{(m)}$ and $Q_{ij}^{(2,m)}$ must also match. This fixes the coupling constants ζ_ℓ^m mentioned in the previous chapter [16]. To illustrate how the matching fixes the scale k, consider tensor modes $m = 2$. Recall that the evolution equation for $E_{(2)}$, equation (3.37), is

$$E''_{(2)} + 2\mathcal{H}E'_{(2)} + (k^2 + 2K)E_{(2)} = 0, \tag{4.49}$$

so, if $\beta_{(2)} = E_{(2)}$, they must have the same evolution equation. Comparing (4.49) with (4.46), we see that they are the same equation if

$$\mathcal{S}_{(2)} = -k^2 - 2K = -\nu^2 + K,$$

recalling call that, for tensor modes, $\nu^2 = k^2 + 3K$.

Other modes can also be matched with similar arguments (see [16]). The full matching is presented in Table 4.

Type	ν_m	ζ_ℓ^m
I	0	δ_ℓ^2
VII$_0$	$m\ell_s^{-1}$	1
IX	$3\ell_c^{-1}$	δ_ℓ^2
V	$i\ell_c^{-1}$	$(-i)^{\ell-m}\sqrt{\dfrac{m(m+1)}{\ell(\ell+1)}}$
VII$_h$	$m\ell_s^{-1} + i\ell_c^{-1}$	$\prod_{p=m+1}^{\ell}(-i)\sqrt{\dfrac{(p-1)\sqrt{h}+mi}{(p+1)\sqrt{h}-mi}}$

Table 4: The matching of Bianchi models with perturbation modes. Note that Bianchi IX is only matched to tensor perturbations.

Bianchi I is matched to a perturbation with infinite wavelength and Bianchi IX is matched to the largest possible perturbation in a closed space, that is, a perturbation with wavelength half the circumference of the universe. The open models are matched to supercurvature modes, that is, modes whose wavelength is larger than the curvature scale of the universe [57].

In open universes, perturbations that decay at infinity may be decomposed into subcurvature modes, that is, modes with $(\nu\ell_c)^2 > 0$. The most general perturbation, though, might depend on supercurvature modes, $(\nu\ell_c)^2 < 0$. The inclusion of such modes requires the radial functions to be complex. As we mentioned earlier, in curved space, the radial functions are written in terms of hyperspherical Bessel functions, which can be generalized to complex order by analytic continuation. Moreover, the coefficients $\beta_{(m)}$ and the other SVT modes expanded into harmonics also become complex, but the original tensors remain real.

A final remark must be made. From a purely mathematical perspective, the matching of Bianchi models and FLRW perturbations is straightforward: we evaluated whether there is a regime where the Einstein's Field Equations for the FLRW perturbations are equal to the EFEs for the shear in nearly isotropic Bianchi. We saw that this regime exists and is achieved on the homogeneous perturbation scale k or ν in Table 4. No assumption beyond standard perturbations is made to obtain this result. A first consequence of this is that, if one is interested in studying nearly isotropic Bianchi models, the EFEs for FLRW perturbations can be employed to understand the evolution of the shear.

However, more importantly, the matching of perturbations implies that Bianchi models are physical, regardless of the perturbations' origin. In general, FLRW perturbations break all spatial symmetries, but we saw that there is a scale where homogeneity is recovered in perturbed FLRW models (see Table 4). Therefore, in this scale, there is symmetry by translations and the perturbations have the same evolution equation as the shear, even if their origin is stochastic.

4.6 INITIAL CONDITIONS

Now that we matched the shear with homogeneous perturbations, we are interested in understanding how the shear evolves. Solutions to the equation (4.46) are divided into two categories: regular and irregular [58]. Regular solutions go to zero as $\eta \to 0$. Irregular modes, conversely, are decaying solutions; in this scenario, the shear becomes larger as $\eta \to 0$, ultimately diverging.

In the previous chapter, we computed how vector and tensor perturbations evolve without a source term. Vector modes decay and thus are irregular. This is also true for the vector part of the shear, as $\mathcal{S}_{(\pm 1)} = 0$. Tensor modes, on the other hand, have both decaying and growing solutions. We saw in equation (3.52) that the regular solution to $E_{(2)}$, and thus $\beta_{(2)}$, during radiation era is

$$\beta_{(2)} = C_1 \frac{\sin(k\eta)}{\eta} \Rightarrow \beta_{(2)} = C_1 k, \tag{4.50}$$

therefore

$$\beta'_{(2)}(\eta) = -\frac{C_1 k^3}{3}\eta. \tag{4.51}$$

If we choose, at some instant η_i, $\beta_{(2)}(\eta_i) = 1$, we have $\beta'_{(2)}(\eta_i) = -k^2\eta_i/3$. These are the regular initial conditions for the tensor part of the shear.

If we consider non-standard scenarios where vector modes are sourced by anisotropic stress, then these modes also present non-decaying solutions. One of such models is presented in [59, 60]. In these works, the authors considered an isocurvature perturbation where photons and neutrinos had, in early times, opposite bulk velocities after neutrino decoupling. Since the total momentum is zero, this solution does not diverge as $\eta \to 0$. In this context, the shear is constant in early times and decays sufficiently later to leave observational imprints. There are, however, other possible neutrino isocurvature initial conditions [61].

Let us explore the neutrino velocity isocurvature initial condition in flat space. The vector gravitational potential in synchronous gauge is $\hat{\Phi}_i = -\hat{E}'_i$, but $\hat{E}_i = -k^{-1}\sum_{a=\pm 1} E_{(a)} Q_i^{(a)}$ such that $\Phi_{(1)} = k^{-1}E'_{(1)} = k^{-1}\hat{\sigma}_{(1)}$. To follow the developments made in reference [60] and obtain the same results, we redefine the vector part of the shear as $\bar{\sigma}_{(1)} \equiv -\Phi_{(1)} = -k^{-1}E'_{(1)}$. Hence, the equations for vector perturbations in terms of the vector part of the shear $\bar{\sigma}$ (we will drop the identifying index (1), as we will be working only with vector modes) are

$$k^2\bar{\sigma} = 16\pi G a^2 q \tag{4.52}$$

$$-k(\bar{\sigma}' + 2\mathcal{H}\bar{\sigma}) = 8\pi G a^2 \bar{P}\Pi. \tag{4.53}$$

Note that the Euler Equation can be obtained from these equations.

In the past, neutrinos and photons were coupled. Hence, it is reasonable to expect that, after neutrino decoupling, their velocities are approximately equal. However, we are going to ignore this consideration and allow them to be different. We are going to show that, if there is a non-zero anisotropic stress at early times, these velocities must have opposite directions. Furthermore, we are going to assume that $\mathcal{N}_\ell = 0$ for $\ell > 2$, so the infinite Boltzmann hierarchy for neutrinos (equation (3.94)) becomes a system of two equations.

During radiation era, photons are tightly coupled with baryons, so they do not source the anisotropic stress tensor. Therefore, the only effect that feeds it is the neutrino free streaming. In the tight coupling regime, the velocity of photons and baryons are the same, so they act as a single fluid with velocity

$$v_b = v_\gamma = \frac{v_0}{1+R}, \tag{4.54}$$

where $R \equiv (3/4)\bar{\rho}_b/\bar{\rho}_\gamma$. Moreover, we can neglect cold dark matter energy density during this era. This implies that $q = (\bar{\rho}_\nu + \bar{P}_\nu)v_\nu + (\bar{\rho}_\gamma + \bar{P}_\gamma)v_\gamma$. In this context, the evolution equations become

$$k^2\bar{\sigma}^2 = 16\pi G a^2[(\bar{\rho}_\nu + \bar{P}_\nu)v_\nu + (\bar{\rho}_\gamma + \bar{P}_\gamma)v_\gamma] \tag{4.55}$$

$$-k(\bar{\sigma}' + 2\mathcal{H}\bar{\sigma}) = \frac{8\pi G a^2}{3}\bar{\rho}_\nu \Pi_\nu \tag{4.56}$$

$$v_\nu' = -\frac{k}{8}\Pi_\nu \tag{4.57}$$

$$\Pi_\nu' = \frac{8k}{5}v_\nu + \frac{8k}{5}\bar{\sigma}, \tag{4.58}$$

where the last two equations are the Boltzmann hierarchy for neutrinos, using $\mathcal{N}_1 = v_\nu$ and $\Pi_\nu = (8\sqrt{3}/5)\mathcal{N}_2$ [46].

We are interested in the evolution of these quantities very early in time, so we can Taylor expand them with respect to η up to second order. As a consequence, the system differential equations above become a system of equations on the expansion coefficients. Explicitly, we write

$$\begin{aligned}
\bar{\sigma} &= s_0 + s_1\eta + s_2\eta^2 \\
v_\gamma &= g_0 + g_1\eta + g_2\eta^2 \\
v_\nu &= n_0 + n_1\eta + n_2\eta^2 \\
\Pi_\nu &= \pi_0 + \pi_1\eta + \pi_2\eta^2.
\end{aligned}$$

The scale factor may also be expanded

$$a = \frac{\Omega_m H_0}{\omega^2}\left(\omega\eta + \frac{\omega^2\eta^2}{4}\right), \tag{4.59}$$

where $\omega \equiv H_0\Omega_m/\sqrt{\Omega_r}$. We are expanding these quantities up to second order because of the derivatives on η, but, here, we are interested only in first order terms. To illustrate this calculation, we substitute the expansions above in equation (4.56),

$$2s_0\eta + 3\left(s_1 + \frac{1}{4}\omega s_0\right)\eta^2 = -\frac{R_\nu}{k}(\pi_0 + \pi_1\eta + \pi_2\eta^2), \tag{4.60}$$

where $R_\nu \equiv \Omega_\nu/\Omega_r$. To zero order, we immediately find $\pi_0 = 0$. To first order,

$$\pi_1 = -\frac{2k}{R_\nu}s_0. \tag{4.61}$$

Moreover, from equation (4.58),

$$\pi_1 + 2\pi_2\eta = \frac{8k}{5}(n_0 + n_1\eta) + \frac{8k}{5}(s_0 + s_1\eta). \tag{4.62}$$

To the first order, we find

$$n_0 = -\frac{5 + 4R_\nu}{4R_\nu}s_0. \tag{4.63}$$

Finally, from equation (4.57)

$$n_1 + n_2\eta = -\frac{k}{8}\pi_1\eta \Rightarrow n_1 = 0. \tag{4.64}$$

Continuing this process, we obtain up to first order

$$\bar{\sigma} = s_0\left(1 - \frac{15}{2}\frac{\omega\eta}{4R_\nu + 15}\right) \tag{4.65}$$

$$v_\gamma = s_0\frac{4R_\nu + 5}{R_\gamma}\left(\frac{1}{4} - \frac{3R_b}{16R_\gamma}\omega\eta\right) \tag{4.66}$$

$$v_\nu = -\frac{s_0}{4}\frac{4R_\nu + 5}{R_\nu} \tag{4.67}$$

$$\Pi_\nu = -2\frac{ks_0}{R_\nu}\eta, \tag{4.68}$$

where $R_\gamma \equiv \Omega_\gamma/\Omega_r$, $R_b \equiv \Omega_b/\Omega_m$, and

$$v_0 = s_0\frac{4R_\nu + 5}{4R_\nu}. \tag{4.69}$$

We see that, in order for the shear to be sourced, the velocities of the photon gas and the neutrino gas must have opposite directions. In `AniLoS` and `AniCLASS`, these initial conditions are implemented to the second order.

As mentioned previously, this is only one of the many possible neutrino isocurvature initial conditions. For example, truncating the Boltzmann hierarchy in $\mathcal{N}_3$ instead of $\mathcal{N}_2$ gives rise to another initial condition. In `AniLoS` and `AniCLASS`, we also implement this initial condition.

Chapters 3 and 4 derived the equations necessary to understand the CMB evolution in nearly isotropic Bianchi models with non-decaying vector and tensor modes. We are now ready to explore how to implement these equations numerically.

5 ANICLASS AND ANILOS

Having derived the theoretical background necessary for our work, we are now in position to explore the numerical implementation of the equations we have encountered so far. To summarize, in chapter 3, we derived the evolution equations for the temperature fluctuations and polarization of the CMB in a perturbed FLRW universe. We saw that the system of differential equations that describe this physics, the Boltzmann hierarchy, is infinite, so solving it numerically for large multipoles may not be efficient. However, the Boltzmann equation has an integral solution whose numerical implementation is more efficient than the differential counterpart. This is because we only need to solve the Boltzmann hierarchy for the first few multipoles, which are the source terms of the Line-of-sight integral.

In chapter 4, we connected nearly isotropic Bianchi models with the homogeneous limit of linear perturbation theory in FLRW, which corresponds to the maximal wavelength allowed by the geometry of the model. To work with a specific nearly isotropic Bianchi model, we only need to keep one perturbation scale in FLRW. Thus, the observational imprints these cosmologies leave on the CMB are computed by the usual Boltzmann equation in FLRW limited to a single perturbation scale. However, open Bianchi models are matched with supercurvature modes, perturbations larger than the curvature scale [57]. This causes the radial functions and the SVT modes to be complex. Until now, none of the CMB software worried about supercurvature modes, so the hyperspherical Bessel functions were never implemented for complex order. Thus, one of the steps in the development of `AniLoS` and `AniCLASS` was to modify existing implementations to include complex numbers.

In this context, our goal is to implement numerically the Line-of-sight integral in nearly isotropic Bianchi models. To this end, we developed two programs, `AniLoS` and `AniCLASS`, that compute this solution of the Boltzmann equation. In this chapter, we present some details and outputs of our codes.

5.1 OVERVIEW

`AniLoS` (*Anisotropic Line-of-Sight*) and `AniCLASS` (Anisotropic CLASS) [18] are integrators that solve equations (3.104), (3.105), and (3.106) in the context of nearly isotropic Bianchi models. `AniLoS` is a simple `Python` package that is easy to understand and modify. `AniCLASS` is a modification of `CLASS`[19], inheriting several features from its parent software. Despite both programs performing the same calculations, they have different goals.

First, `Python` offers a high-level interface that simplifies the coding process. The libraries `NumPy` and `SciPy`, used for numerical and scientific computation, provide stable solvers for differential equations and efficiently handle array operations if the code is vectorized. Nonethe-

---

[18] `https://github.com/jgvicente/AniLoS`

[19] `CLASS` is a popular code in cosmology. The acronym stands for "Cosmic Linear Anisotropy Solving System". See the code repository in `https://github.com/lesgourg/class_public` and reference [62] for more details.

less, in situations where vectorization is not possible, there are tools like Numba and `Cython` to improve performance. Dealing with complex algebra is straightforward. Hence, new initial conditions or exotic physics are easily implemented in `AniLoS`. On the other hand, it is limited by `Python`'s performance.

In contrast to `AniLoS`, `AniCLASS` is a more low-level code since it is written in `C`. `AniCLASS` is a minimal modification of `CLASS`. On the one hand, this is beneficial because `CLASS` has a native implementation of the Boltzmann hierarchy and the Line-of-sight integral, so rewriting these complicated equations in `C` was not necessary. On the other hand, `CLASS` is a very intertwined code, meaning that all modules are connected in such a way that local changes cannot be made without affecting the whole software. The major change from "standard" `CLASS` is the inclusion of complex numbers, needed to deal with supercurvature modes. The `C` language has a native complex type, which we use to perform this modification. The complexity of `AniCLASS` makes it challenging to be modified by the end user, but `C`'s performance is unmatched, making it an unparalleled tool for statistical analyses.

`AniLoS` and `AniCLASS` contain the Bianchi models VII$_h$, VII$_0$, V, and IX for vector modes (non-decaying modes, as described in section 4.6) and regular (unsourced) tensor modes. In fact, the only Bianchi models implemented are VII$_h$ and IX because the other two models are limiting cases of Bianchi VII$_h$. Bianchi VII$_0$ belongs to the family of Bianchi VII$_h$. Recall the definition of h, equation (4.12), and the structure constants in Table 3,

$$\sqrt{h} = \frac{\ell_s}{\ell_c}.$$

Thus, in Bianchi VII$_0$, $h = 0$ ($\ell_c \to \infty$). Similarly, Bianchi V is obtained from Bianchi VII$_h$ when the curvature radius ℓ_c is kept constant but $\ell_s \to \infty$. Bianchi I does not need to be implemented because, as we saw in Table 4, it does not change the Boltzmann hierarchy, so its effects are already implemented in standard codes as a quadrupolar contribution.

In this section, we will provide an overview of the programs. We will mainly focus on `AniLoS` since it is the easiest to understand. Figure 12 provides a flowchart of the algorithm. `AniLoS` is divided into two modules and a `C`-extension: `anilos.py`, `hierarchy.py`, and `hybess.pyx`. The main module, `anilos.py`, contains a `Python` class, `Anilos`, which stores the main functions and coordinates the whole process. The module `hierarchy.py` keeps the numerical implementation of the Boltzmann hierarchy for the source terms. Finally, the goal of module `hybess.pyx` is to compute the radial functions.

The first box, **INPUT**, refers to the input parameters necessary for the code. The input parameters can be divided into four categories:

- Bianchi parameters

  Only two parameters are needed to determine a Bianchi model[20]. In `AniLoS`, these pa-

---

[20] We recall to the reader that we only consider Bianchi models with FlRW limits.

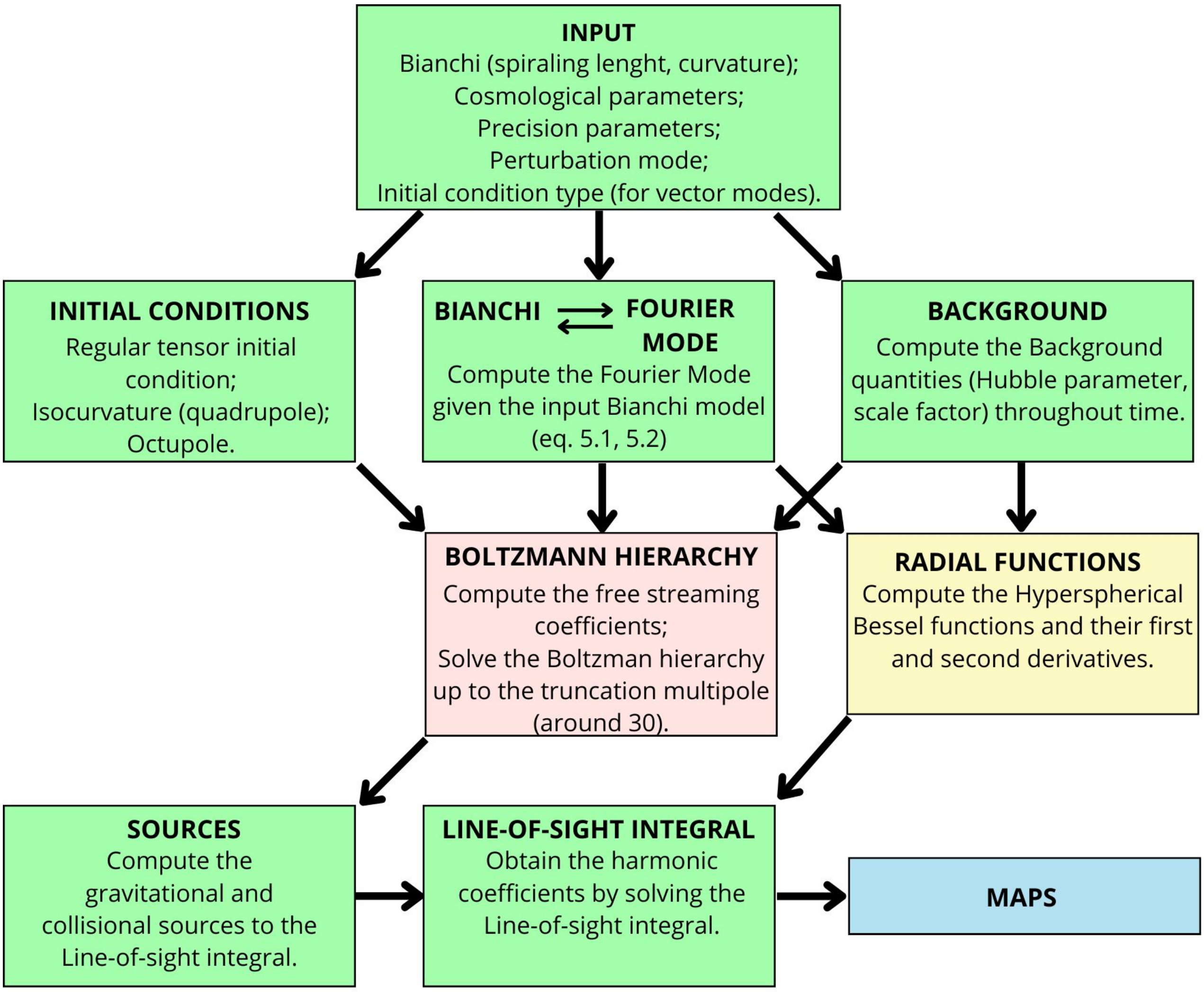

Figure 12: Flowchart for `AniLoS` and `AniCLASS`. The colors refer to the module in which each step is found. Functions in the green boxes are in the `anilos.py` module, the pink box is in `hierarchy.py`, and the yellow box is in `hybess.pyx`. The blue box is the output of the algorithm.

rameters are $\sqrt{h}$ and Ω_K. The curvature parameter yields ℓ_c and, once the curvature scale is fixed, $\sqrt{h}$ fixes ℓ_s. In `AniCLASS`, the input parameters are $m\ell_s^{-1}$, which is simply the Fourier mode k, and Ω_K. By trial and error, we find that Bianchi VII_0 is obtained by setting $\Omega_K \sim 10^{-5}$ and Bianchi V is achieved with $\sqrt{h} \sim 10^4$. Bianchi IX only needs one parameter, Ω_K, to be defined. As we saw in section 4.5, Bianchi IX is matched to the largest possible gravitational wave in a closed universe.

- Cosmology

  The usual cosmological parameters, such as H_0 and the fractional energy density parameters, can be used as input by the user. Moreover, the user may specify the conditions that set the tight-coupling regime, an approximation used for some values of η during the computation of the Boltzmann hierarchy.

- Perturbation type and initial conditions

  The user can also specify the perturbation type (tensor, vector, or both) and the initial conditions for vector modes.

- Precision parameters

  `AniLoS` also allows the user to specify the Boltzmann hierarchy truncation multipole ℓ_{trunc} and the maximum multipole ℓ_{max} computed by the Line-of-sight integral. Additionally, the user may also choose precision targets for the ODE solver in `AniLoS`. In `AniCLASS`, the code inherits optimization options from `CLASS`.

The **BIANCHI** $\rightleftarrows$ **FOURIER MODE** box contemplates the matching of the input parameters with the generalized Fourier mode, as in Table 4. Explicitly,

$$\nu_m = \frac{m}{\ell_s} + \frac{i}{\ell_c} \qquad \text{if } \mathcal{K} = -1, \tag{5.1}$$

$$\nu_m = \frac{3}{\ell_c} \qquad \text{if } \mathcal{K} = 1. \tag{5.2}$$

BACKGROUND refers to the calculation of background quantities. These quantities — η, $\mathcal{H}(\eta)$, $a(\eta)$, etc — are calculated using `CLASS`' routines. In `AniLoS`, we use `CLASS`' `Python` wrapper, `classy`. The outputs are arrays of background quantities computed at several values of η:

$$\begin{aligned} \eta &\to \text{array}[\eta_i, \ldots, \eta_0] \\ \mathcal{H} &\to \text{array}[\mathcal{H}(\eta_i), \ldots \mathcal{H}(\eta_0)] \\ \tau' &\to \text{array}[\tau'(\eta_i), \ldots \tau'(\eta_0)], \end{aligned}$$

starting from $\eta_i = 4 \times 10^{-9}$ Mpc — which corresponds to $a_i = 2 \times 10^{-7}$ and $z_i = 9 \times 10^{13}$ — up to today, $\eta_0 = 13828$ Mpc. Recall that we use CLASS' native limits [62].

The initial conditions, in box **INITIAL CONDITIONS**, are described in section 4.6. For tensor modes, we saw that

$$\beta_{(2)}(\eta_i) = 1 \qquad \text{and} \qquad \beta'_{(2)} = -\frac{k^2}{3}\eta_i. \tag{5.3}$$

All other variables, $\mathcal{N}_2^{(2)}(\eta_i)$, $\Theta_2^{(2)}(\eta_i)$, $E_2^{(2)}(\eta_i)$, $B_2^{(2)}(\eta_i)$, ..., $\mathcal{N}_{\ell_{\text{trunc}}}^{(2)}(\eta_i)$, $\Theta_{\ell_{\text{trunc}}}^{(2)}(\eta_i)$, $E_{\ell_{\text{trunc}}}^{(2)}(\eta_i)$, $B_{\ell_{\text{trunc}}}^{(2)}(\eta_i)$ are set to zero initially.

For vector modes, we derived the isocurvature initial condition in which $\mathcal{N}_\ell^{(1)} \neq 0$ for $\ell = 1, 2$ initially. In our derivation, we assumed a flat universe and retained only first-order terms in η. Using `Mathematica`[21], we extended this calculation to curved universes, including terms up to second order in η. Within the programs, this initial condition is labeled as “isocurvature”. Additionally, we implemented an alternative initial condition, referred to as “octopole”, where $\mathcal{N}_3^{(1)} \neq 0$ initially as well.

Figure 13 shows the evolution of $\beta_{(1)}$. The anisotropic stress is initially non-zero, feeding the shear and keeping it almost constant until $a \sim 10^{-4}$. Figure 14 shows the regular initial condition for tensor modes. Even though the anisotropic stress is small in the past, the shear is almost constant until $a \sim 10^{-4}$. These graphics were computed using our implementation of the Boltzmann hierarchy, truncating the system at $\ell_{\text{trunc}} = 30$. The input parameters for these graphics are:

- Bianchi VII$_h$: $\Omega_K = 0.1$, $\sqrt{h} = 0.01$;
- Bianchi VII$_0$: $\Omega_K = 10^{-5}$, $\sqrt{h} = 10^{-3}$;
- Bianchi V: $\Omega_K = 0.1$, $\sqrt{h} = 10^4$;
- Bianchi IX: $\Omega_K = -0.1$.

The next box is **BOLTZMANN HIERARHCY**. We implement the equations (3.94), (3.95), (3.96), and (3.97) for vector and tensor modes which are solved up to the multipole ℓ_{trunc}. The numerical implementation of these equations is straightforward in `Python`, as they follow a structure

$$y' = Ay, \tag{5.4}$$

where $y^\top$, the transpose of y, is

$$y^\top = \begin{pmatrix} \beta_{(m)} & \beta'_{(m)} & \mathcal{N}_1^{(m)} & \Theta_1^{(m)} & E_1^{(m)} & B_1^{(m)} & \ldots & \mathcal{N}_{\ell_{\text{trunc}}}^{(m)} & \Theta_{\ell_{\text{trunc}}}^{(m)} & E_{\ell_{\text{trunc}}}^{(m)} & B_{\ell_{\text{trunc}}}^{(m)} \end{pmatrix},$$

and the matrix A contains the free streaming, gravitational, and collision terms. We employ the function `solve_ivp`[22] from `Scipy` to solve this system using the Runge-Kutta method of order 5(4), which is the default solver. To compute the product (5.4), we tested implementations based on sparse matrices and conventional `for` loops. We found that a `for` loop decorated with Numba is the most efficient method to compute this system if $\ell_{\text{trunc}} \lesssim 100$. The truncation method employed can be found in [63].

Numba transforms `Python` code into machine code at run time. This is achieved by simply placing the decorator `@jit` on top of the function we want to “numbanize”. A disadvantage of Numba is that, during the first call of a function, the compiler takes more time than usual to perform the computation. This is because, during this first call, Numba is figuring out each function’s argument type. Once it knows this information, the subsequent calls are optimized.

---

[21] `https://www.wolfram.com/mathematica/`

[22] Documentaion: `https://docs.scipy.org/doc/scipy-1.15.0/reference/generated/scipy.integrate.solve_ivp.html`.

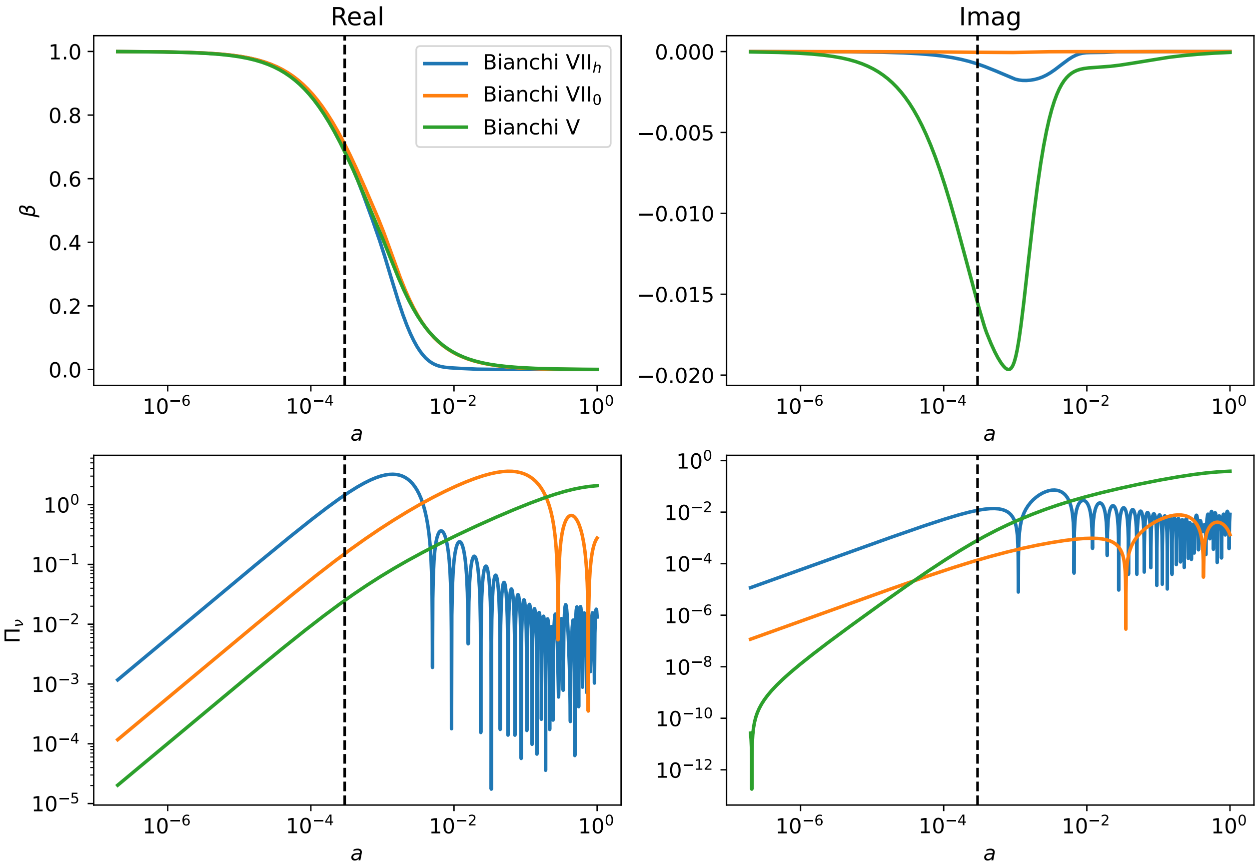

Figure 13: Evolution of the vector part of the shear (first row), and the neutrino anisotropic stress (second row) for isocurvature initial conditions. The dashed line marks the end of the tight-coupling regime.

This disadvantage can be overcome if we inform Numba beforehand about the types, as we do in `AniLoS`. Figures 13, 14, and 15 are outputs of our implementation of the Boltzmann hierarchy.

With the multipoles $\Theta_2^{(2)}$, $E_2^{(2)}$, and $B_2^{(2)}$ for tensor modes, or $\Theta_1^{(1)}$, $E_1^{(1)}$, $B_1^{(1)}$, $\Theta_2^{(1)}$, $E_2^{(1)}$, and $B_2^{(1)}$ for vector modes, we compute the sources terms ${}^{\Theta}\mathcal{C}_\ell^{(m)} + \mathcal{G}_\ell^{(m)}$ and ${}^{E}\mathcal{C}_\ell^{(m)}$ following their definitions in section 3.6.2. We compute them for each η in the conformal time array and interpolate them to create functions of η. This step is in the box **SOURCES**.

Before solving the Line-of-sight integral, the last piece of code we require is in the box **RADIAL FUNCTIONS**. These functions are defined in section 3.6.3. For each coefficient $\Theta_\ell^{(m)}$, $E_\ell^{(m)}$, and $B_\ell^{(m)}$ we must compute an integral on η, so the radial functions must be stored in arrays containing their values calculated at several instants of time. Moreover, we wish to obtain the coefficients up to $\ell_{\max} \sim 1000$, so the radial functions have to be calculated for thousands of values of η and thousands of multipoles. Hence, the computation of these functions is numerically intensive. `CLASS`' implementation is based on the fact that hyperspherical Bessel functions follow recurrence relations

$$\Phi_\ell^\nu(\chi) = \frac{1}{\sqrt{\nu^2+\ell^2}}\left[(2\ell-1)\coth\chi\,\Phi_{\ell-1}^\nu - \sqrt{\nu^2+(\ell-1)^2}\,\Phi_{\ell-2}^\nu\right] \tag{5.5}$$

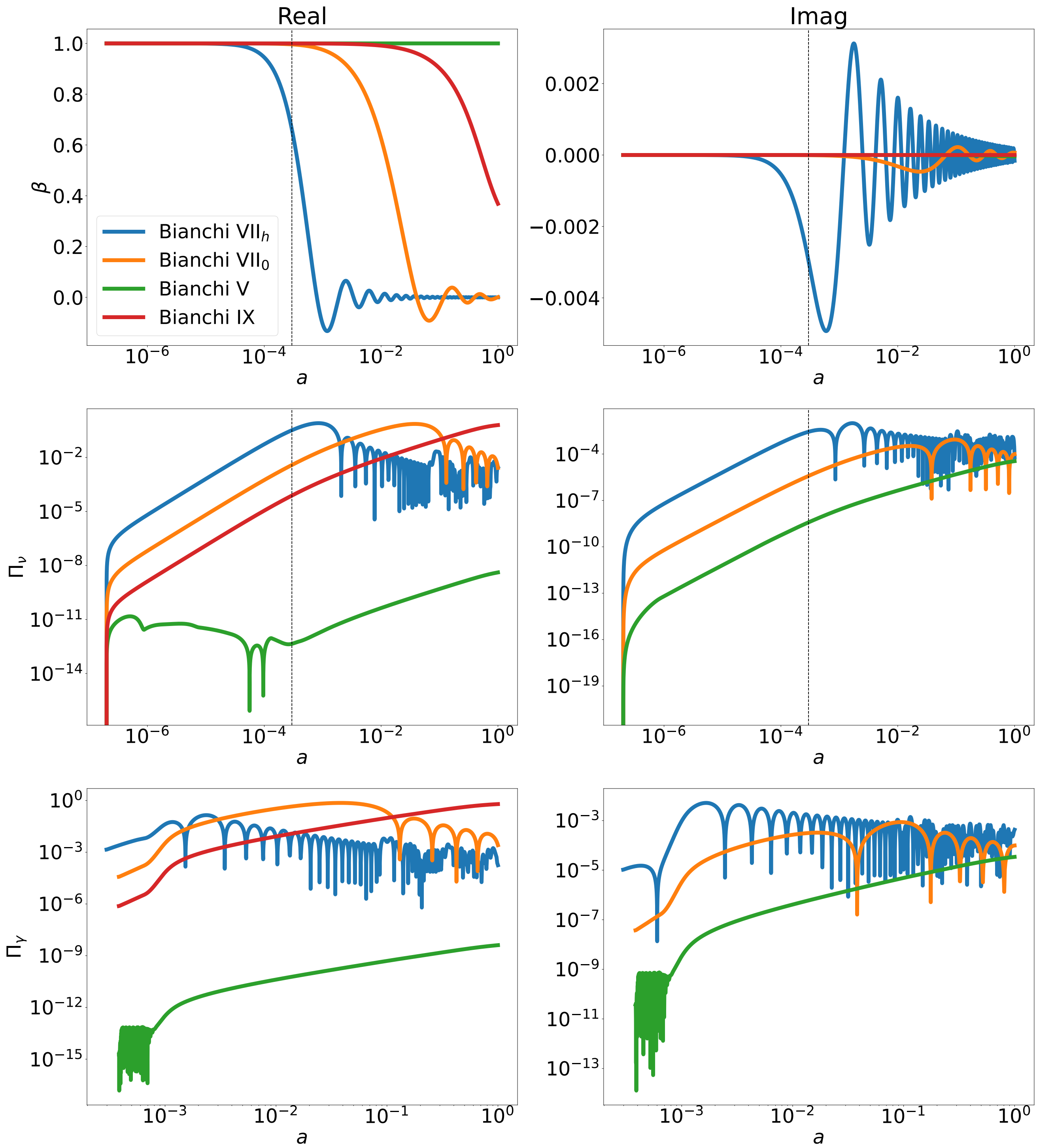

Figure 14: Evolution of the shear (first row), the neutrino anisotropic stress (second row), and the photon anisotropic stress for regular tensor modes. Note that the graphics in the last row start at later times. The dashed line marks the end of the tight-coupling regime.

and

$$\frac{\mathrm{d}\Phi_\ell^\nu}{\mathrm{d}\chi} = \ell \coth \chi \Phi_\ell^\nu(\chi) - \sqrt{\nu^2 + (l+1)^2}\Phi_{\ell+1}^\nu(\chi), \tag{5.6}$$

which provides a very fast method. Luckily, these recurrence relations also hold for complex ν, so we can use them in our code. The details of this implementation are found in the Appendix.

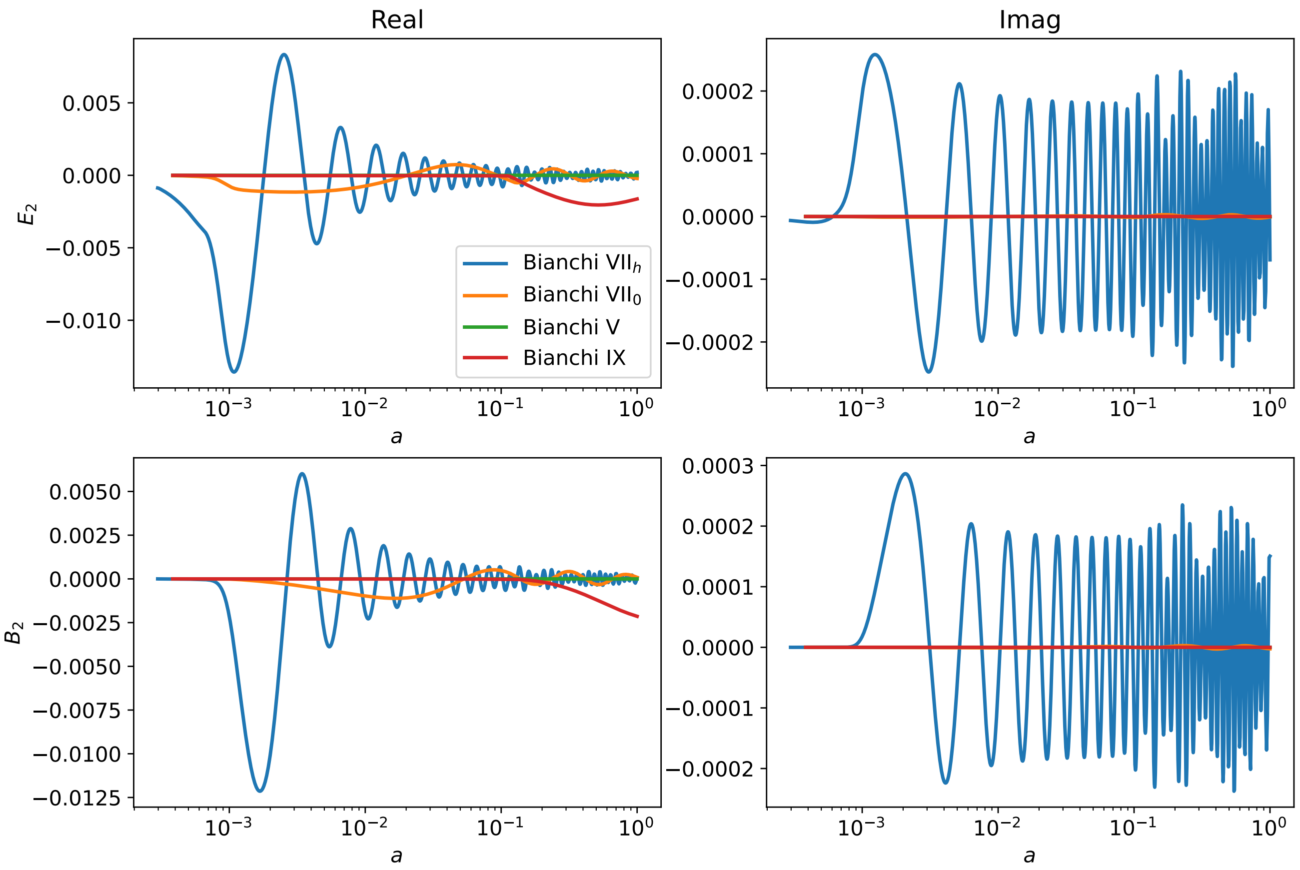

Figure 15: Tensor mode of the polarization quadrupole.

In `AniLoS`, the routines that compute the radial functions are written in `Cython`.

With the source terms and the radial functions, we have everything to compute the Line-of-sight integral. The Line-of-sight integral implementation is straightforward in `Python`. Schematically, we have

$$\frac{M_\ell^{(m)}}{2\ell+1} = \int \mathrm{d}\eta \sum_{j=1}^{2} S_j^{(m)} R_\ell^{(jm)}, \tag{5.7}$$

where $M_\ell^{(m)}$ stands for the temperature fluctuations or polarization, $S_j^{(m)}$ represents the source term, and $R_\ell^{(jm)}$ represents the radial functions ${}_0\epsilon_\ell^{(jm)}$, ${}_2\epsilon_\ell^{(jm)}$, or ${}_2\beta_\ell^{(jm)}$. The source terms do not depend on ℓ, so they are stored in an array like

$$S_j \rightarrow \text{array}[S_j(\eta_i), ..., S_j(\eta_0)]. \tag{5.8}$$

Conversely, the radial functions depend on ℓ, so they are stored as

$$R_\ell^{(jm)} \rightarrow \text{array}\begin{bmatrix} R_1^{(jm)}(\eta_i) & \dots & R_1^{(jm)}(\eta_0) \\ R_2^{(jm)}(\eta_i) & \dots & R_2^{(jm)}(\eta_0) \\ \vdots & \ddots & \vdots \\ R_{\ell_{\max}}^{(jm)}(\eta_i) & \dots & R_{\ell_{\max}}^{(jm)}(\eta_0) \end{bmatrix}. \tag{5.9}$$

We found that the most efficient method to compute the integrand is to use `Numpy`'s function `tile`, such that we create an array

$$S_j \to \text{array} \begin{bmatrix} S_j(\eta_i) & \dots & S_j(\eta_0) \\ S_j(\eta_i) & \dots & S_j(\eta_0) \\ \vdots & \ddots & \vdots \\ S_j(\eta_i) & \dots & S_j(\eta_0) \end{bmatrix} \tag{5.10}$$

and vectorize the product of the source terms with the radial functions.

We use the function `trapezoid` from `Scipy` to perform the numerical integration. The outputs are arrays $\Theta_\ell^{(m)}$, $E_\ell^{(m)}$, and $B_\ell^{(m)}$ for $\ell = m, \dots, \ell_{\text{max}}$. We connect these multipoles with $a_{\ell m}^{\Theta}$, $a_{\ell m}^{E}$, and $a_{\ell m}^{B}$ following equation (3.116). With the harmonic coefficients, we can produce maps using the library `Healpy` that show the observational effects of these models on the CMB.

Before showcasing the results, a few remarks about the efficiency of our programs are at hand. Figure 16 compares the Line-of-sight integral computation time for several values of ℓ_{max} using `AniLoS` and `AniCLASS`. `AniCLASS` is much faster than `AniLoS`, which is expected since it is written in `C`. This also shows the power capacity of `AniCLASS` and the reason it is suitable for statistical analysis. `AniLoS` would take about 100 hours to complete an MCMC run with 500,000 elements, whereas `AniCLASS` would only take 1 hour.

Table 5 shows the time performance at each box in Figure 12 for `AniLoS`. The most demanding code piece in this run is the Boltzmann hierarchy but, as ℓ_{max} increases, the time spent at the computation of the Radial functions and the Line-of-sight integral increases while it remains the same at the Boltzmann hierarchy.

Step	Time (s)	Percentage %
Hierarchy	0.40	36
Radial	0.23	22
Line-of-sight	0.21	18
Others	0.26	24

Table 5: Time performance at each "step" in `AniLoS`. Input parameters are $\Omega_K = 0.1$, $\sqrt{h} = 0.1$, and $\ell_{\text{max}} = 1000$.

5.2 MAPS

In this section, we present graphical outputs from `AniLoS` and `AniCLASS`. Figures 17a to 19c illustrate the harmonic coefficients $a_{\ell,2}^{\Theta}$, $a_{\ell,2}^{E}$, and $a_{\ell,2}^{B}$ in several scenarios. In all cases, the intensity of $a_{\ell,2}$ falls with ℓ, indicating that only the first few multipoles contribute significantly to observational effects. For instance, Figure 17a shows:

$$\frac{|a_{15,2}^{\Theta}|}{|a_{2,2}^{\Theta}|} \sim 0.01, \tag{5.11}$$

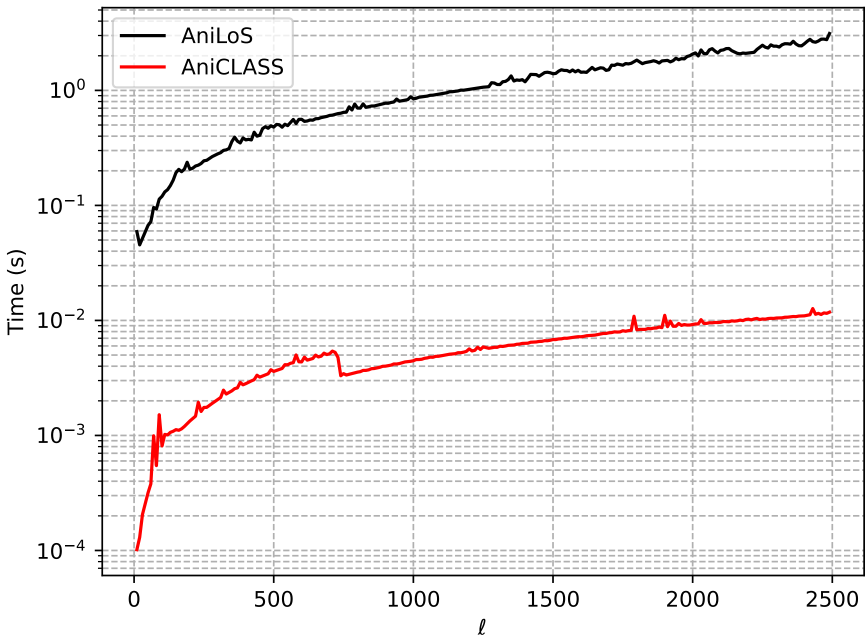

Figure 16: The Line-of-sight integral computation time for increasing values of ℓ in a conventional Laptop (Processor: Intel Core I5-8250U, RAM: 8GB). `AniCLASS` is 100 to 1000 faster than `AniLoS` because it is written in `C`.

implying that multipoles beyond $\ell \sim 15$ have a less than 1% contribution to the fluctuations. However, in Figure 18, multipoles up to $\ell \sim 30$ remain relevant. In Bianchi V, the signal rapidly declines after the first few multipoles. Thus, in Bianchi V, the power is predominantly concentrated in the quadrupole, leading to a quadrupolar pattern in the maps. Conversely, higher multipoles remain significant in Bianchi VII$_h$ and VII$_0$, resulting in more complex, higher-order patterns. Bianchi IX, similar to Bianchi V, produces only a quadrupolar structure.

Using these harmonic coefficients, we generate temperature fluctuation and polarization maps. Figures 20 to 23 showcase these maps, created using our Line-of-sight integrators under different Bianchi models, perturbation modes, and initial conditions.

Figures 20 and 21 highlight the spiral patterns characteristic of Bianchi VII$_h$ and VII$_0$ models. These patterns arise both from the significance of multipoles beyond the quadrupole and the spiral behavior of integral curves generated by the Killing Vector Fields, as illustrated in Figure 10. Figures 22 and 23, by contrast, demonstrate the purely quadrupolar patterns typical of Bianchi V and IX cosmologies.

To conclude, we are going to briefly comment on the numerical differences between `AniLoS` and `AniCLASS`. In the physically motivated Bianchi VII$_h$ cases, e.g, $\ell_s/\ell_c \gtrsim 10^{-2}$, the codes agree with a $\lesssim 1\%$ precision (see Figure 24). Numerical instability appears in non-physical scenarios where ℓ_s is much smaller than the curvature radius ($\ell_s \sim 100$ Mpc when $\ell_c \sim 10^6$ Mpc). In Bianchi VII$_0$, relative errors of order 10% also appear when the spiraling length is unphysically small, e.g, $\ell_s \sim 100$ Mpc. The Bianchi V model, as we see in Figure 19, presents some differences between `AniLoS` and `AniCLASS` at higher multiples, but they agree at

1% on the quadrupole, which is the dominant effect.

With this, we have addressed all components outlined in Figure 12. This chapter has provided a qualitative overview of our Line-of-sight integral implementation, detailing the process from input to output.

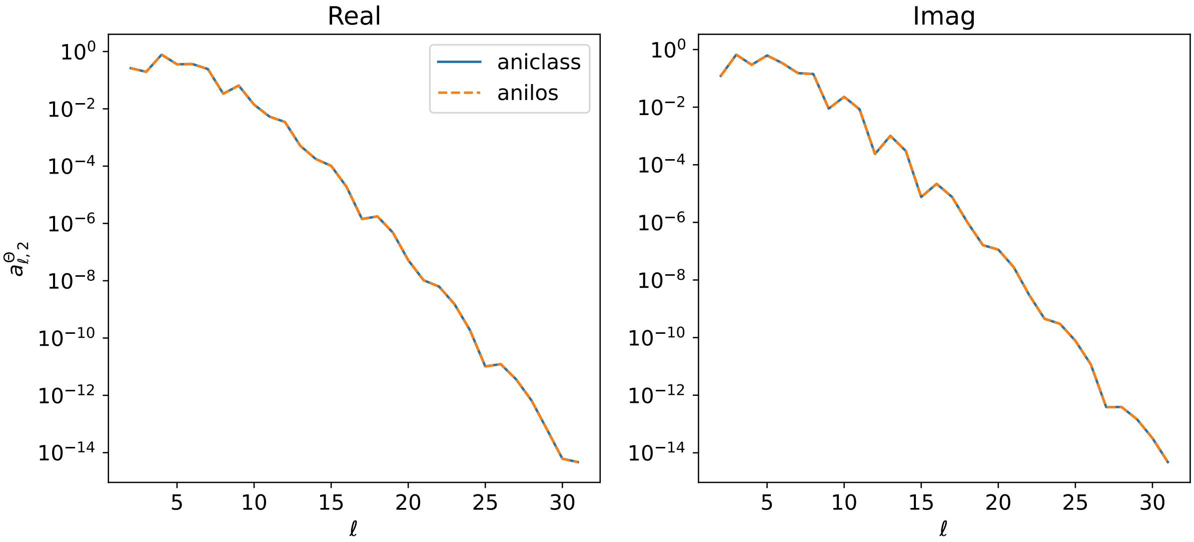

(a) Temperature

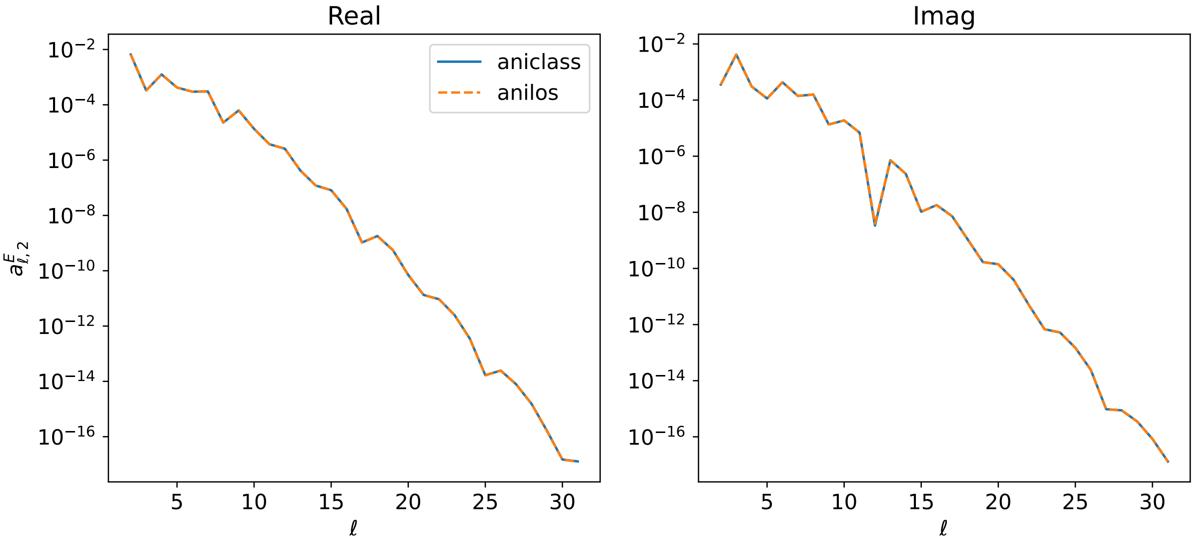

(b) E-mode

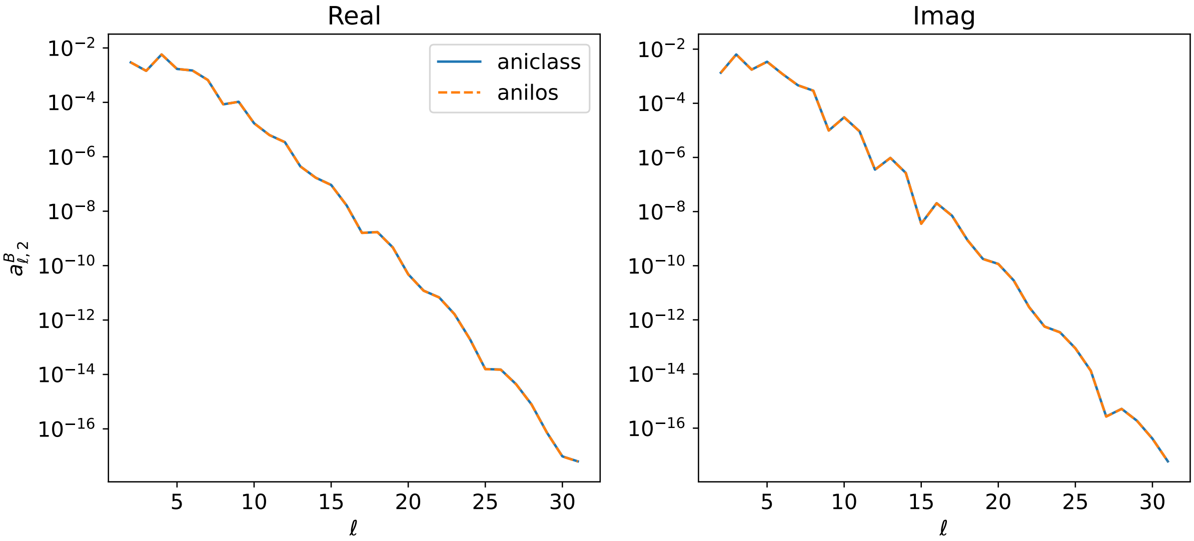

(c) B-mode

Figure 17: Tensor harmonic coefficients in Bianchi VII$_h$ with $\Omega_b = 0.04$, $\Omega_{\text{CDM}} = 0.20$, $\Omega_K = 0.01$, $\sqrt{h} = 0.1$, and $\ell_s = 4421$ Mpc.

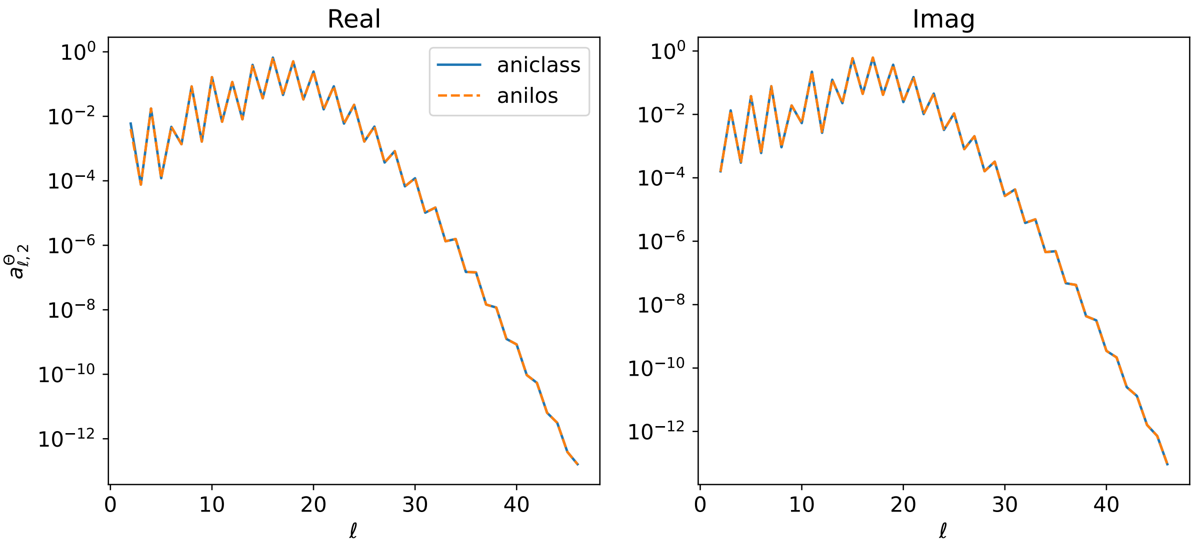

(a) Temperature

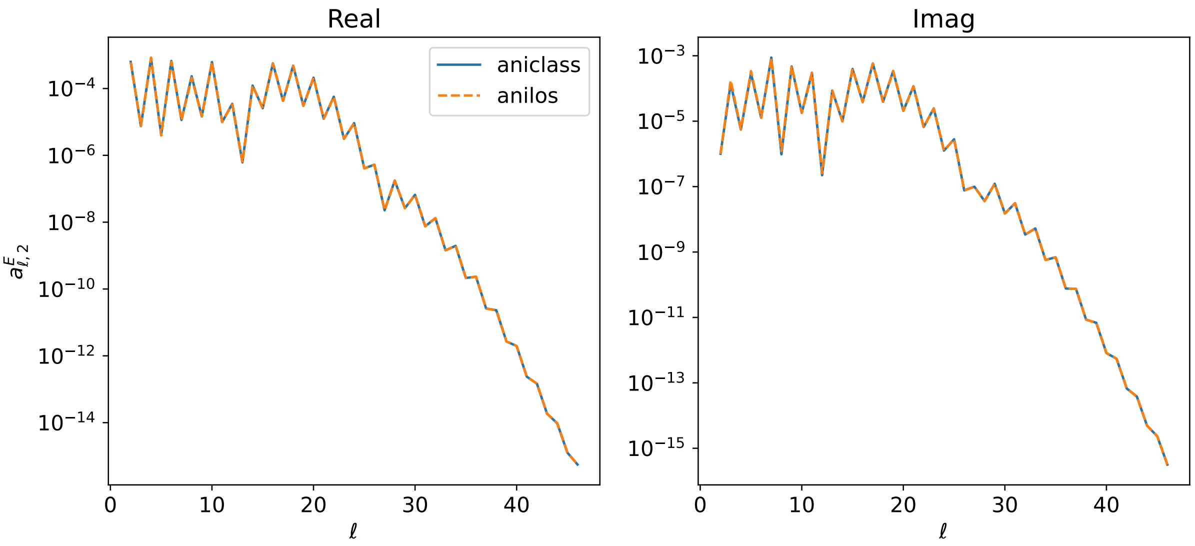

(b) E-mode

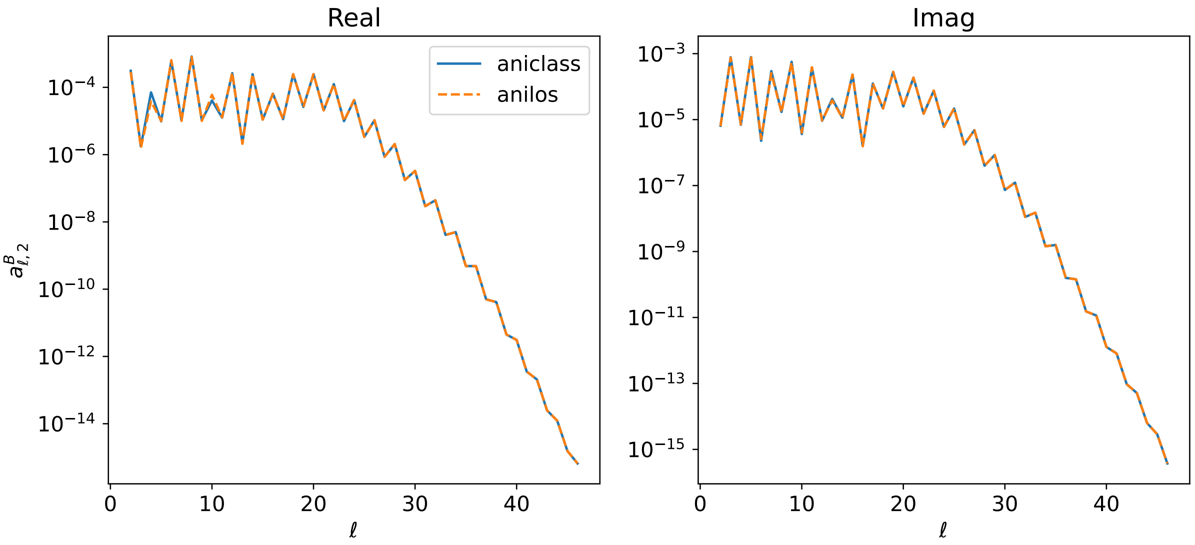

(c) B-mode

Figure 18: Tensor harmonic coefficients in Bianchi VII$_0$ with $\Omega_b = 0.04$, $\Omega_{\text{CDM}} = 0.26$, $\Omega_K = 10^{-5}$ (concordance model), $\sqrt{h} = 10^{-3}$, and $\ell_s = 1398$ Mpc.

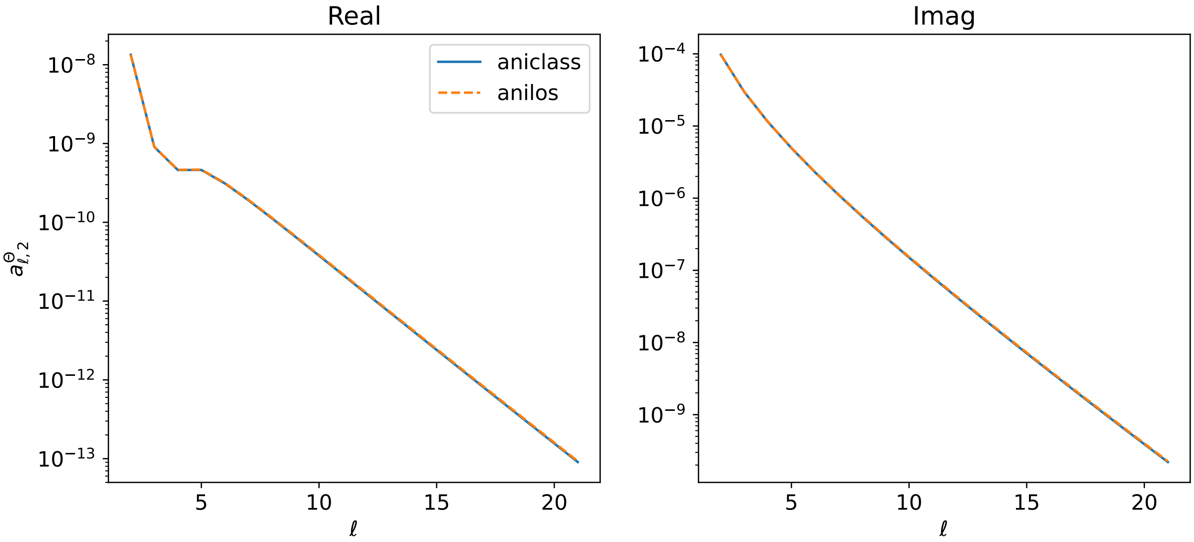

(a) Temperature

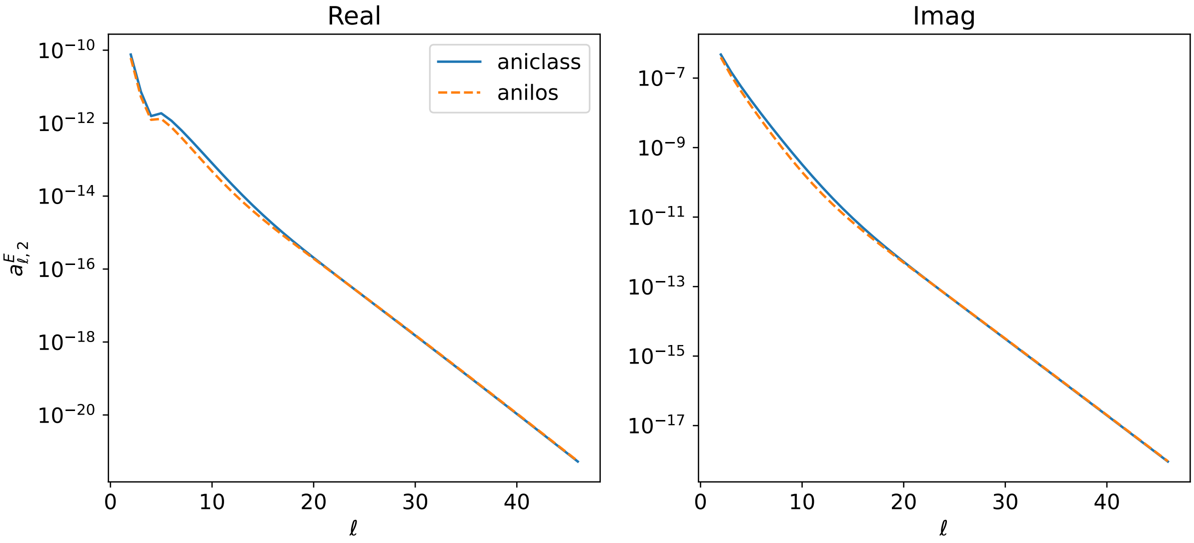

(b) E-mode

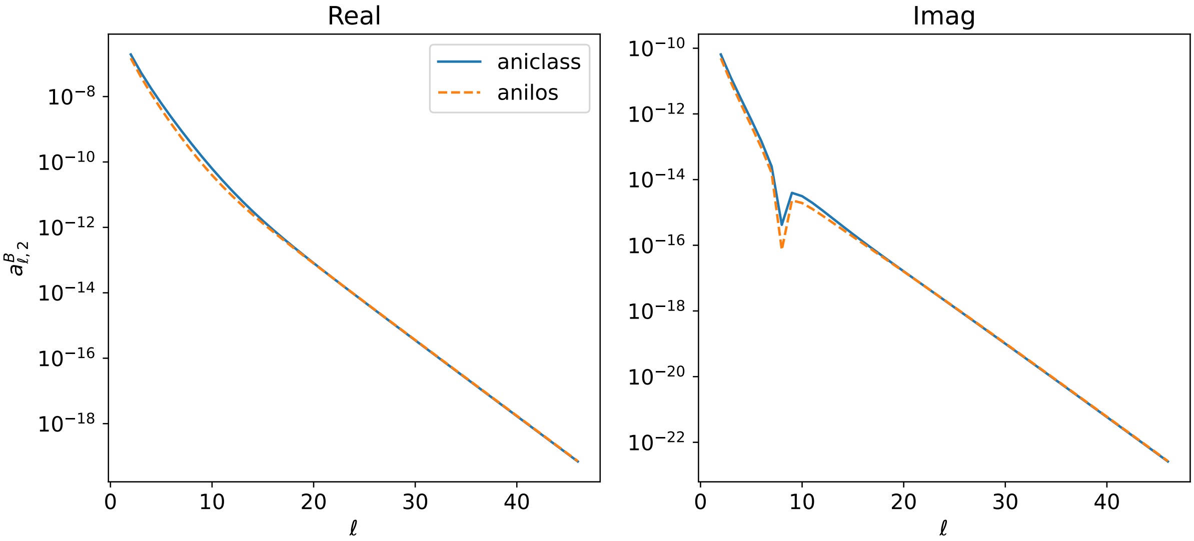

(c) B-mode

Figure 19: Tensor harmonic coefficients in Bianchi V with $\Omega_K = 0.1$ and $\sqrt{h} = 10^4$.

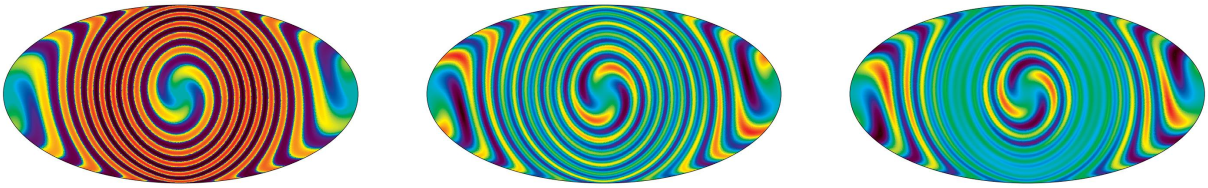

(a) Temperature (tensor) **(b)** E mode (tensor) **(c)** B mode (tensor)

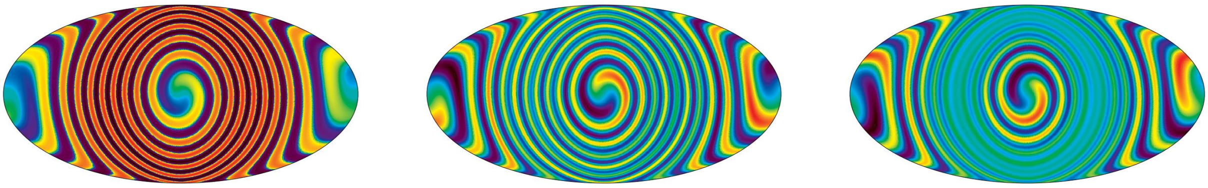

(d) Temperature (velocity isocurvature) **(e)** E mode (velocity isocurvature) **(f)** B mode (velocity isocurvature)

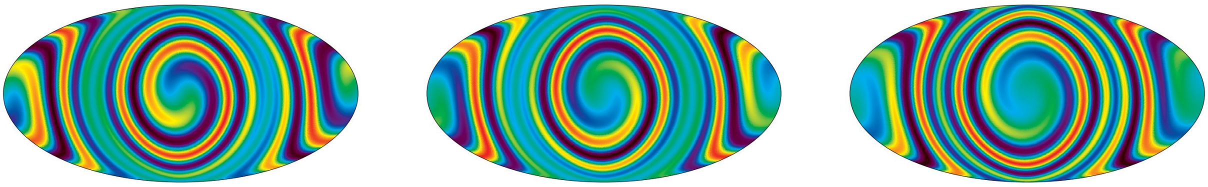

(g) Temperature (octupole isocurvature) **(h)** E mode (octupole isocurvature) **(i)** B mode (octupole isocurvature)

Figure 20: Patterns in the CMB in Bianchi VII$_0$ with parameters $\Omega_m = 0.24$, $\Omega_\Lambda = 0.76$, $\Omega_K = 10^{-5}$ and $\ell_s = 884$ Mpc. Maps (a) and (d) are on a symlog scale.

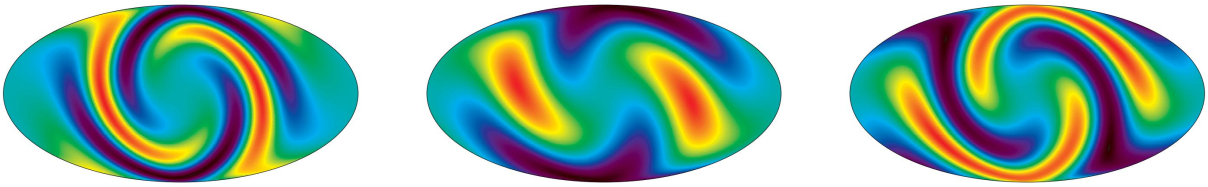

(a) Temperature (tensor) **(b)** E mode (tensor) **(c)** B mode (tensor)

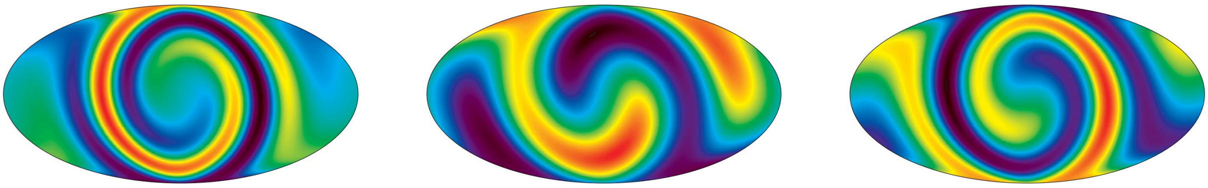

(d) Temperature (velocity isocurvature) **(e)** E mode (velocity isocurvature) **(f)** B mode (velocity isocurvature)

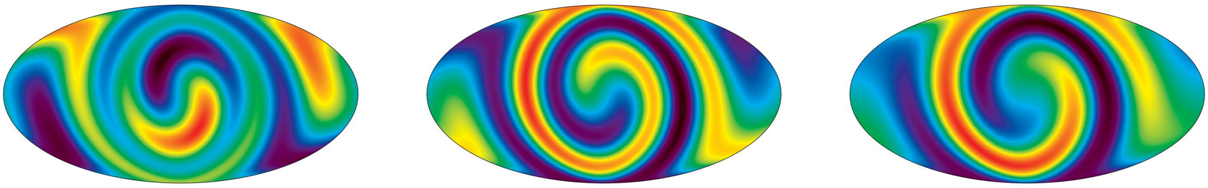

(g) Temperature (octupole isocurvature) **(h)** E mode (octupole isocurvature) **(i)** B mode (octupole isocurvature)

Figure 21: Patterns in the CMB in Bianchi VII$_h$ with $\Omega_m = 0.3$, $\Omega_\Lambda = 0$, and $\sqrt{h} = 0.5$.

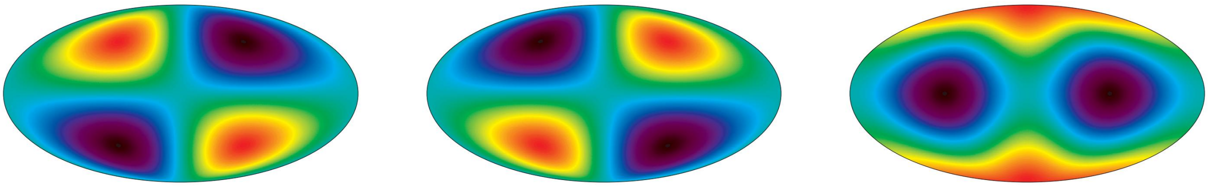

(a) Temperature (tensor)

(b) E mode (tensor)

(c) B mode (tensor)

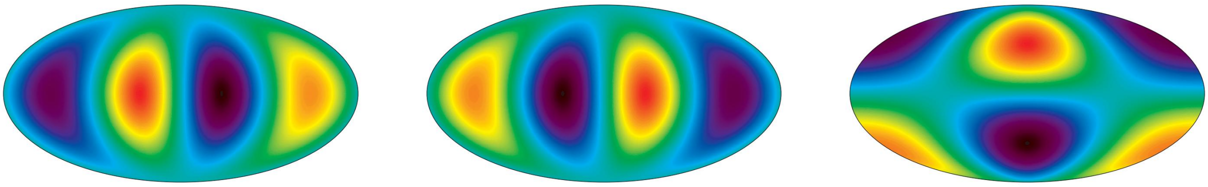

(d) Temperature (velocity isocurvature)

(e) E mode (velocity isocurvature)

(f) B mode (velocity isocurvature)

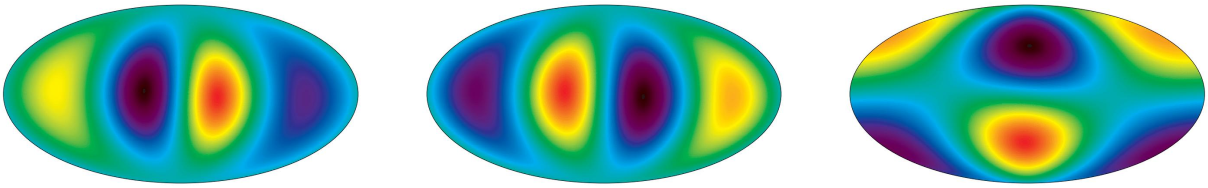

(g) Temperature (octupole isocurvature)

(h) E mode (octupole isocurvature)

(i) B mode (octupole isocurvature)

Figure 22: Patterns in the CMB in Bianchi V with $\Omega_K = 0.01$.

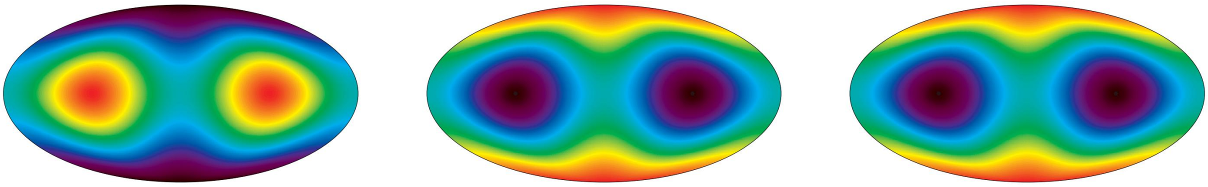

(a) Temperature

(b) E mode

(c) B mode

Figure 23: Patterns in the CMB in Bianchi IX – only tensor modes. The curvature parameter is $\Omega_K = -0.01$.

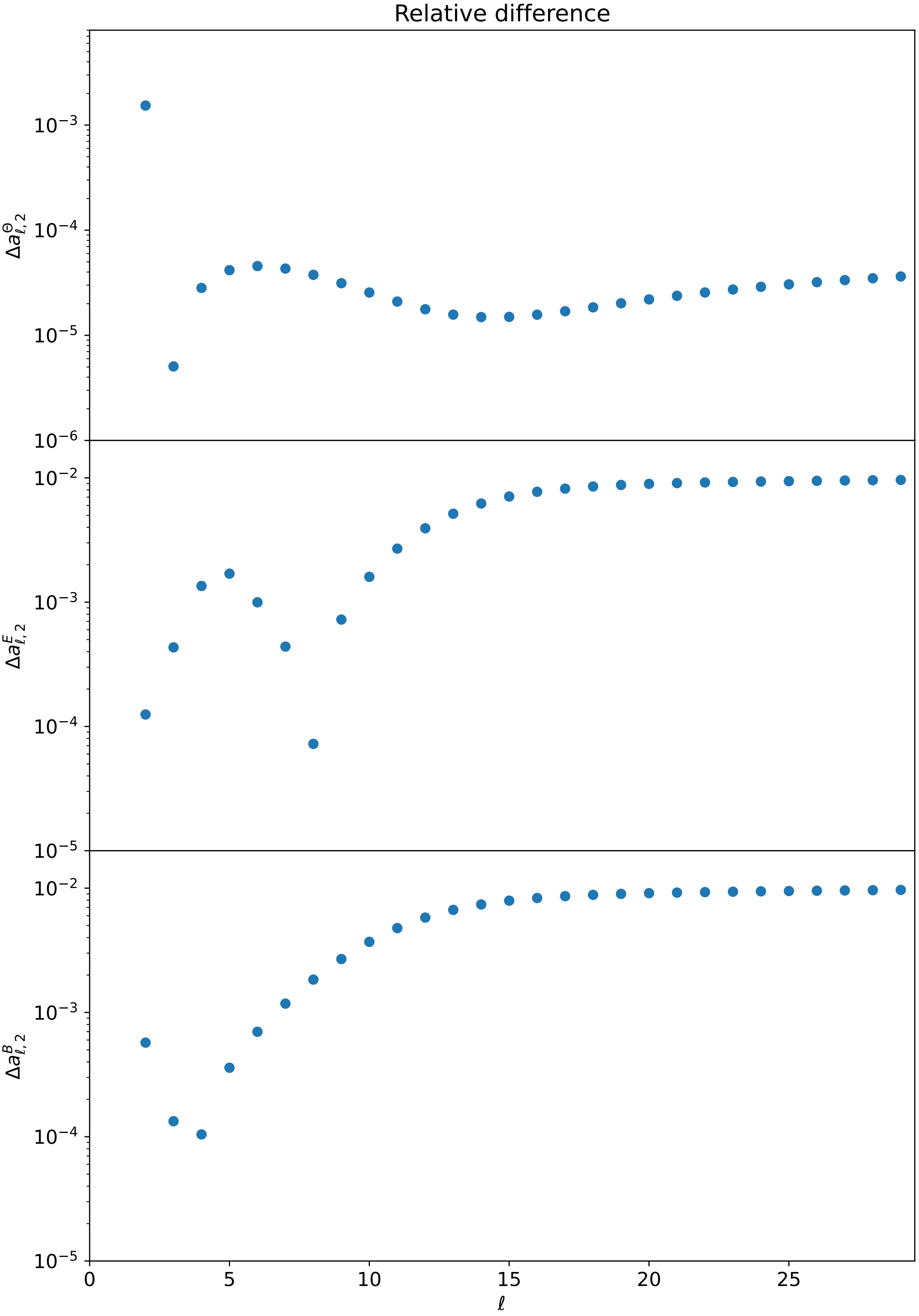

Figure 24: Relative difference between the multipoles computed by `AniLoS` and `AniCLASS` in Bianchi VII$_h$ with $\Omega_K = 0.01$, $\Omega_m = 0.24$, $\Omega_\Lambda = 0.75$, and $\sqrt{h} = 0.01$.

CONCLUSION AND PROSPECTS

In this dissertation, we reviewed the theoretical and numerical framework of AniLoS and AniCLASS. The theoretical basis is standard cosmology, plus the theory of homogeneous spatial sections and the connection between Bianchi models and perturbations in FLRW. One of the goal of this dissertation was to derive the equations (under simplifying conditions) that are numerically implemented. The Boltzmann equation, hierarchy, and Line-of-sight integral were derived for temperature fluctuations in a flat universe, but we pointed out how they differ in curved spaces. We derived the neutrino isocurvature velocity initial condition in a flat universe and briefly commented on the family of infinite neutrino isocurvature initial conditions that exist. We showed how Bianchi models are matched with homogeneous FLRW perturbations and illustrated this process for tensor modes. Finally, we presented a summary of the AniLoS structure.

To summarize the key points, the approach employed to describe nearly isotropic Bianchi cosmologies introduces a simple method for studying their effects on the CMB. They are mathematically equivalent to homogeneous perturbations. As a result, AniLos and AniCLASS do not diverge much from existing Line-of-sight integrators. The only difference, and the major difficulty, is the inclusion of supercurvature modes.

AniLoS and AniCLASS are useful codes for isotropy testing. Any modification is easily performed in AniLoS, so it offers a ground zero to add exotic physics in the context of Bianchi models and CMB. Figure 16 shows the efficiency of AniCLASS, proving that this code is well-suited for statistical analysis. Figures 20 to 23 are the showcases of our codes. They demonstrate the observational imprints that Bianchi cosmologies leave on the CMB. We saw that Bianchi IX and Bianchi V only present a quadrupolar pattern on the CMB, which makes these models difficult to probe statistically, as we would not be able to distinguish between them and the quadrupole from standard perturbations. In contrast, Bianchi VII_h and Bianchi VII_0 have more complex patterns spread through higher multipoles.

This work focused on creating the programs. Our initial intention was to produce these programs and perform statistical analysis with them, but the first step was more difficult than we anticipated. Now, we are ready to pursue the second step. We also did not anticipate how many possibilities these codes offer for future analyses. Bianchi models with isocurvature initial conditions are a combination that has not been tested yet, but it provides interesting scenarios to evaluate.

Particularly, in the next years CMB probes such as CMB-S4 [64] and LiteBird [65] will provide invaluable data on polarization. With access to more precise data than we currently have, `AniLoS` and `AniCLASS` will be able to improve the bounds on the shear obtained in [9]. Moreover, several observables in cosmology are based on Line-of-sight integrals, such as weak lensing. This means that the methods and framework we employed here can be extended for a greater variety of phenomena, introducing new threads to isotropy testing.

However, AniLoS and AniCLASS are more than simple Line-of-sight integrators. Because they contain an implementation of the Boltzmann equation for supercurvature modes, they also offer a numerical foundation for studies focusing on these modes. In principle, it is possible to test whether supercurvature modes affect the CMB, regardless of Bianchi models. This avenue has not been followed yet.

REFERENCES

References

[1] AGHANIM, N. et al. Planck 2018 results-i. overview and the cosmological legacy of planck. *Astronomy & Astrophysics*, EDP sciences, v. 641, p. A1, 2020.

[2] CLARKSON, C.; MAARTENS, R. Inhomogeneity and the foundations of concordance cosmology. *Classical and Quantum Gravity*, IOP Publishing, v. 27, n. 12, p. 124008, 2010.

[3] MAARTENS, R. Is the universe homogeneous? *Philosophical Transactions of the Royal Society A: Mathematical, Physical and Engineering Sciences*, The Royal Society Publishing, v. 369, n. 1957, p. 5115–5137, 2011.

[4] ELLIS, G. The bianchi models: Then and now. *General Relativity and Gravitation*, Kluwer Academic Publishers-Plenum Publishers, New York, v. 38, n. 6, p. 1003–1015, 2006.

[5] ELLIS, G. F.; MACCALLUM, M. A. A class of homogeneous cosmological models. *Communications in Mathematical Physics*, Springer, v. 12, p. 108–141, 1969.

[6] MCEWEN, J. D. et al. Bayesian analysis of anisotropic cosmologies: Bianchi VIIh and WMAP. *Monthly Notices of the Royal Astronomical Society*, v. 436, n. 4, p. 3680–3694, 10 2013. ISSN 0035-8711.

[7] ADE, P. et al. Planck 2015 results-xviii. background geometry and topology of the universe. *Astronomy & Astrophysics*, EDP sciences, v. 594, p. A18, 2016.

[8] SAADEH, D. et al. A framework for testing isotropy with the cosmic microwave background. *Monthly Notices of the Royal Astronomical Society*, Oxford University Press, v. 462, n. 2, p. 1802–1811, 2016.

[9] SAADEH, D. et al. How isotropic is the universe? *Physical review letters*, APS, v. 117, n. 13, p. 131302, 2016.

[10] BARROW, J. Light Elements and the Isotropy of the Universe. *Monthly Notices of the Royal Astronomical Society*, v. 175, n. 2, p. 359–370, 05 1976. ISSN 0035-8711.

[11] ALURI, P. K. et al. Is the observable universe consistent with the cosmological principle? *Classical and Quantum Gravity*, IOP Publishing, v. 40, n. 9, p. 094001, 2023.

[12] PEEBLES, P. J. E. Anomalies in physical cosmology. *Annals of Physics*, Elsevier, v. 447, p. 169159, 2022.

[13] ABDALLA, E. et al. Cosmology intertwined: A review of the particle physics, astrophysics, and cosmology associated with the cosmological tensions and anomalies. *Journal of High Energy Astrophysics*, v. 34, p. 49–211, 2022. ISSN 2214-4048.

[14] VALENTINO, E. D.; MELCHIORRI, A.; SILK, J. Planck evidence for a closed universe and a possible crisis for cosmology. *Nature Astronomy*, Nature Publishing Group, v. 4, n. 2, p. 196–203, 2020.

[15] PONTZEN, A.; CHALLINOR, A. Linearization of homogeneous, nearly-isotropic cosmological models. *Classical and Quantum Gravity*, IOP Publishing, v. 28, n. 18, p. 185007, 2011.

[16] PEREIRA, T. S.; PITROU, C. Bianchi spacetimes as supercurvature modes around isotropic cosmologies. *Physical Review D*, APS, v. 100, n. 12, p. 123534, 2019.

[17] SELJAK, U.; ZALDARRIAGA, M. A Line-of-Sight Integration Approach to Cosmic Microwave Background Anisotropies. *ApJ*, v. 469, p. 437, out. 1996.

[18] ELLIS, G. F. R.; MAARTENS, R.; MACCALLUM, M. A. H. *Kinematics of cosmological models*. [S.l.]: Cambridge University Press, 2012. 73–88 p.

[19] STEWART, J.; STEWART, J. M. *Advanced general relativity*. [S.l.]: Cambridge university press, 1993.

[20] THORNE, K. S. Multipole expansions of gravitational radiation. *Reviews of Modern Physics*, APS, v. 52, n. 2, p. 299, 1980.

[21] HAWKING, S. On the rotation of the universe. *Monthly Notices of the Royal Astronomical Society*, Oxford University Press, v. 142, n. 2, p. 129–141, 1969.

[22] WALD, R. M. *General relativity*. [S.l.]: University of Chicago press, 2010.

[23] LINEWEAVER, C. H. et al. The dipole observed in the cobe dmr four-year data. *arXiv preprint astro-ph/9601151*, 1996.

[24] GOURGOULHON, É. *3+1 Formalism in General Relativity: Bases of Numerical Relativity*. Berlin, Heidelberg: Springer Berlin Heidelberg, 2012. 29–54 p. ISBN 978-3-642-24525-1.

[25] ISHAM, C. J. *Modern differential geometry for physicists*. [S.l.: s.n.], 1999.

[26] WEINBERG, S. *Gravitation and Cosmology: Principles and Applications of the General Theory of Relativity*. New York: John Wiley and Sons, 1972. ISBN 978-0-471-92567-5, 978-0-471-92567-5.

[27] PEEBLES, P. J. E. *The large-scale structure of the universe*. [S.l.: s.n.], 1980.

[28] SCRIMGEOUR, M. I. et al. The wigglez dark energy survey: the transition to large-scale cosmic homogeneity. *Monthly Notices of the Royal Astronomical Society*, Blackwell Science Ltd Oxford, UK, v. 425, n. 1, p. 116–134, 2012.

[29] YADAV, J. et al. Testing homogeneity on large scales in the sloan digital sky survey data release one. *Monthly Notices of the Royal Astronomical Society*, The Royal Astronomical Society, v. 364, n. 2, p. 601–606, 2005.

[30] SPRINGEL, V. et al. Simulations of the formation, evolution and clustering of galaxies and quasars. *nature*, Nature Publishing Group UK London, v. 435, n. 7042, p. 629–636, 2005.

[31] RIESS, A. G. et al. Observational evidence from supernovae for an accelerating universe and a cosmological constant. *The astronomical journal*, IOP Publishing, v. 116, n. 3, p. 1009, 1998.

[32] PERLMUTTER, S. et al. Measurements of ω and λ from 42 high-redshift supernovae. *The Astrophysical Journal*, IOP Publishing, v. 517, n. 2, p. 565, 1999.

[33] SALINAS, S. R. *Introdução à física estatística*. [S.l.]: Edusp, 1999.

[34] KOLB, E. *The early universe*. [S.l.]: CRC press, 2018.

[35] DODELSON, S.; SCHMIDT, F. *Modern cosmology*. [S.l.]: Elsevier, 2024.

[36] AGHANIM, N. et al. Planck 2018 results-vi. cosmological parameters. *Astronomy & Astrophysics*, EDP sciences, v. 641, p. A6, 2020.

[37] RIESS, A. G. et al. A comprehensive measurement of the local value of the hubble constant with 1 km s- 1 mpc- 1 uncertainty from the hubble space telescope and the sh0es team. *The Astrophysical journal letters*, IOP Publishing, v. 934, n. 1, p. L7, 2022.

[38] COLLABORATION, L. D. E. S. et al. Large synoptic survey telescope: dark energy science collaboration. *arXiv preprint arXiv:1211.0310*, 2012.

[39] MELLIER, Y. et al. Euclid. i. overview of the euclid mission. *Astronomy & Astrophysics*, EDP Sciences, 2024.

[40] MAARTENS, R. et al. Overview of cosmology with the ska. In: SISSA MEDIALAB. *Advancing Astrophysics with the Square Kilometre Array*. [S.l.], 2015. v. 215, p. 016.

[41] STEWART, J. M. Perturbations of friedmann-robertson-walker cosmological models. *Classical and Quantum Gravity*, v. 7, n. 7, p. 1169, jul 1990.

[42] KODAMA, H.; SASAKI, M. Cosmological Perturbation Theory. *Progress of Theoretical Physics Supplement*, v. 78, p. 1–166, 01 1984. ISSN 0375-9687.

[43] MALIK, K. A.; WANDS, D. Cosmological perturbations. *Physics Reports*, Elsevier, v. 475, n. 1-4, p. 1–51, 2009.

[44] MUKHANOV, V. *Physical foundations of cosmology*. [S.l.]: Cambridge university press, 2005.

[45] BAUMANN, D. *Cosmology*. [S.l.]: Cambridge University Press, 2022.

[46] HU, W.; WHITE, M. Cmb anisotropies: Total angular momentum method. *Physical Review D*, APS, v. 56, n. 2, p. 596, 1997.

[47] ABRAMOWITZ, M.; STEGUN, I. A. *Handbook of mathematical functions with formulas, graphs, and mathematical tables*. [S.l.]: US Government printing office, 1968. v. 55.

[48] ARFKEN, G. B.; WEBER, H.-J. *Mathematical methods for physicists*. [S.l.]: Academic Press Orlando, FL, 1972.

[49] MAGNUS, W.; OBERHETTINGER, F.; SONI, R. P. *Formulas and Theorems for the Special Functions of Mathematical Physics*. Berlin, Heidelberg: Springer Berlin Heidelberg, 1966. 151–203 p. ISBN 978-3-662-11761-3.

[50] PITROU, C.; PEREIRA, T. S. Beyond scalar, vector, and tensor harmonics in maximally symmetric three-dimensional spaces. *Phys. Rev. D*, American Physical Society, v. 100, p. 123535, Dec 2019.

[51] HU, W. et al. Complete treatment of cmb anisotropies in a frw universe. *Phys. Rev. D*, American Physical Society, v. 57, p. 3290–3301, Mar 1998.

[52] SELJAK, U.; ZALDARRIAGA, M. Signature of gravity waves in the polarization of the microwave background. *Physical Review Letters*, APS, v. 78, n. 11, p. 2054, 1997.

[53] HARRISON, E. R. Normal modes of vibrations of the universe. *Rev. Mod. Phys.*, American Physical Society, v. 39, p. 862–882, Oct 1967.

[54] STEPHANI, H. et al. *Exact solutions of Einstein's field equations*. Cambridge: Cambridge Univ. Press, 2003. (Cambridge Monographs on Mathematical Physics). ISBN 978-0-521-46702-5, 978-0-511-05917-9.

[55] MACCALLUM, M. A. Cosmological models from a geometric point of view. *arXiv preprint arXiv:2001.11387*, 2020.

[56] KING, D. H. Gravity-wave insights to bianchi type-ix universes. *Phys. Rev. D*, American Physical Society, v. 44, p. 2356–2368, Oct 1991.

[57] LYTH, D. H.; WOSZCZYNA, A. Large scale perturbations in the open universe. *Physical Review D*, APS, v. 52, n. 6, p. 3338, 1995.

[58] PONTZEN, A. Rogues' gallery: the full freedom of the bianchi cmb anomalies. *Physical Review D—Particles, Fields, Gravitation, and Cosmology*, APS, v. 79, n. 10, p. 103518, 2009.

[59] BUCHER, M.; MOODLEY, K.; TUROK, N. General primordial cosmic perturbation. *Phys. Rev. D*, American Physical Society, v. 62, p. 083508, Sep 2000.

[60] LEWIS, A. Observable primordial vector modes. *Physical Review D*, APS, v. 70, n. 4, p. 043518, 2004.

[61] REBHAN, A. K.; SCHWARZ, D. J. Kinetic versus thermal-field-theory approach to cosmological perturbations. *Physical Review D*, APS, v. 50, n. 4, p. 2541, 1994.

[62] LESGOURGUES, J. The cosmic linear anisotropy solving system (class) i: overview. *arXiv preprint arXiv:1104.2932*, 2011.

[63] PITROU, C.; PEREIRA, T. S.; LESGOURGUES, J. Optimal boltzmann hierarchies with nonvanishing spatial curvature. *Physical Review D*, APS, v. 102, n. 2, p. 023511, 2020.

[64] ABAZAJIAN, K. et al. Snowmass 2021 cmb-s4 white paper. *arXiv preprint arXiv:2203.08024*, 2022.

[65] HAZUMI, M. et al. Litebird satellite: Jaxa's new strategic l-class mission for all-sky surveys of cosmic microwave background polarization. In: SPIE. *Space Telescopes and Instrumentation 2020: Optical, Infrared, and Millimeter Wave*. [S.l.], 2020. v. 11443, p. 431–450.

[66] LESGOURGUES, J.; TRAM, T. Fast and accurate cmb computations in non-flat flrw universes. *Journal of Cosmology and Astroparticle Physics*, v. 2014, n. 09, p. 032, sep 2014.

[67] ABBOTT, L. F.; SCHAEFER, R. K. A General, Gauge-invariant Analysis of the Cosmic Microwave Anisotropy. *ApJ*, v. 308, p. 546, set. 1986.

[68] TRAM, T. Computation of hyperspherical Bessel functions. *arXiv e-prints*, p. arXiv:1311.0839, nov. 2013.

[69] GAUTSCHI, W. Computational aspects of three-term recurrence relations. *SIAM review*, SIAM, v. 9, n. 1, p. 24–82, 1967.

[70] TEUKOLSKY, S. A. et al. Numerical recipes in c. *SMR*, v. 693, n. 1, p. 59–70, 1992.

[71] WEISSTEIN, E. W. e continued fraction. *https://mathworld. wolfram. com/*, Wolfram Research, Inc., 2013.

APPENDIX

Appendix A — Hyperspherical Bessel functions

In this section, we present the algorithm that computes the radial functions employed in `AniLoS` and `AniCLASS`. To efficiently calculate the Line-of-sight integral, the hyperspherical Bessel functions must be computed by a fast and reliable algorithm. `CLASS` implements these functions using recurrence relations for real order [66]. Since open Bianchi models have complex Fourier modes, it is necessary to extend `CLASS`'s implementation to the complex domain. Luckily, recurrence relations methods can be easily extended to include complex order, as we show below.

Spherical Bessel functions are the radial part of functions that satisfy the Helmholtz equation in flat space. In curved space, we have

$$(D^2 + k^2) f(\boldsymbol{x}) = 0. \tag{A.1}$$

In maximally symmetric spaces, we may use the metric (2.20) or (2.23) to write the Laplacian operator D^2 in terms of derivatives of χ, ϑ, and φ. Then, by separation of variables, the functions that satisfy the equation above have the form $f^{\nu}_{\ell m}(\chi, \theta, \varphi) = \Phi^{\nu}_{\ell}(\chi) Y^{m}_{\ell}(\theta, \varphi)$, where we recall that $\nu^2 = k^2 + (1 + |m|)K$ and that $\Phi^{\nu}_{\ell}(\chi)$ is the hyperspherical Bessel function, which satisfies the equation

$$\frac{1}{r^2(\chi)} \frac{\mathrm{d}}{\mathrm{d}\chi} \left(r^2(\chi) \frac{\mathrm{d}}{\mathrm{d}\chi} \Phi^{\nu}_{\ell} \right) + \left[\nu^2 - \mathcal{K} - \frac{\ell(\ell+1)}{r^2(\chi)} \right] \Phi^{\nu}_{\ell} = 0. \tag{A.2}$$

In the closed case, the periodicity condition makes ν discreet, $\nu K^{-1/2} = 3, 4, 5, ...$ [67]. In the open case, the wavenumber k^2 continuously varies from 0 to ∞. Therefore, for values $k^2 < (1 + |m|)|K|$, ν^2 is negative. Note that modes with $\nu^2 > 0$ provide a complete basis for square-integrable functions [57], and thus, the modes $\nu^2 < 0$ are usually ignored. But we are particularly interested in them.

It is possible to show that these functions can be written in terms of Legendre functions [53] (we follow the normalization convention in [67], [68])

$$\Phi^{\nu}_{\ell}(\chi) = \begin{cases} \sqrt{\dfrac{\pi N^{\nu}_{\ell}}{2\sinh\chi}} P^{-1/2-\ell}_{-1/2+i\nu}(\cosh\chi) & \mathcal{K} = -1, \\ j_{\ell}(\nu\chi) & \mathcal{K} = 0, \\ \sqrt{\dfrac{\pi M^{\nu}_{\ell}}{2\sin\chi}} P^{-1/2-\ell}_{-1/2+\nu}(\cos\chi) & \mathcal{K} = 1, \end{cases} \tag{A.3}$$

where N^{ν}_{ℓ} and M^{ν}_{ℓ} are given by

$$N^{\nu}_{\ell} = \prod_{n=1}^{\ell} (\nu^2 + n^2), \qquad M^{\nu}_{\ell} = \prod_{n=1}^{\ell} (\nu^2 - n^2). \tag{A.4}$$

There is a distinction between the Legendre function for $\mathcal{K} = -1$ and $\mathcal{K} = 1$. The former is defined in the complex domain except in the real line from $+1$ to ∞, whereas the latter is defined in $(-1, 1)$. Following [49], we call the former "Legendre functions of the first kind".

We can exploit this relation with Legendre functions to find recurrence formulas for the hyperspherical Bessel functions. This development is made in great details in [68] for each curvature with real ν, and now we show that it is also valid for complex ν. From now on we will focus on the open case, as it is the only case with complex ν. Legendre functions of the first kind satisfy the following recurrence relations [49]

$$P_\beta^{\alpha+2}(z) + 2(\alpha+1)z(z^2-1)^{-\frac{1}{2}}P_\beta^{\alpha+1}(z) = (\beta-\alpha)(\beta+\alpha+1)P_\beta^\alpha(z) \tag{A.5}$$

and

$$\frac{\mathrm{d}P_\beta^\alpha}{dz} = (\beta+\alpha)(z^2-1)^{-\frac{1}{2}}P_\beta^{\alpha-1}(z) - \frac{\alpha z}{z^2-1}P_\beta^\alpha(z), \tag{A.6}$$

where α, β and z are complex numbers. From these equations, we get

$$\Phi_\ell^\nu(\chi) = \frac{1}{\sqrt{\nu^2+\ell^2}}\left[(2\ell-1)\coth\chi\Phi_{\ell-1}^\nu - \sqrt{\nu^2+(\ell-1)^2}\Phi_{\ell-2}^\nu\right] \tag{A.7}$$

and

$$\frac{\mathrm{d}\Phi_\ell^\nu}{\mathrm{d}\chi} = \ell\coth\chi\Phi_\ell^\nu(\chi) - \sqrt{\nu^2+(l+1)^2}\Phi_{\ell+1}^\nu(\chi). \tag{A.8}$$

The second derivative on χ follows immediately

$$\frac{\mathrm{d}^2\Phi_\ell^\nu}{\mathrm{d}\chi^2} = -\ell\frac{\Phi_\ell^\nu}{\sinh^2\chi} + \ell\coth\chi\frac{\mathrm{d}\Phi_\ell^\nu}{\mathrm{d}\chi} - \sqrt{\nu^2+(l+1)^2}\frac{\mathrm{d}\Phi_{\ell+1}^\nu}{\mathrm{d}\chi}. \tag{A.9}$$

We intend to compute the equations (3.107) – (3.113) for several values of conformal time and multipoles. These equations depend on the Φ_ℓ^ν and its first and second derivatives. In principle, we could use these recurrence relations to efficiently obtain these functions for several values of ℓ. Indeed, for $\ell = 0$, the hyperspherical Bessel function has a simple form [68]:

$$\Phi_0^\nu(\chi) = \frac{\sin(\nu\chi)}{\nu\sinh(\chi)}, \tag{A.10}$$

so the other multipoles could be built upon $\ell = 0$. However, Legendre functions of the second kind, Q_β^α, satisfy the same recurrence relations (A.5) and (A.6), which means that we could introduce another function,

$$\tilde{\Phi}_\ell^\nu = \sqrt{\frac{\pi N_\ell^\nu}{2\sinh\chi}}Q_{-1/2+i\nu}^{-1/2-\ell}(\cosh\chi), \tag{A.11}$$

which would satisfy the same recurrence relations as Φ_ℓ^ν. As a consequence, the recurrence from $\ell = 0$ to ℓ_{max} may not be stable, diverging from the desired function Φ_ℓ^ν at high multipoles.

Luckily, three-terms recurrence relations, such as the one Φ_ℓ^ν satisfies,

$$y_{\ell+1} = a_\ell y_\ell + b_\ell y_{\ell-1}, \tag{A.12}$$

with

$$a_\ell = \frac{2\ell - 1}{\sqrt{\nu^2 + \ell^2}} \qquad \text{and} \qquad b_\ell = \sqrt{\frac{\nu^2 + (\ell-1)^2}{\nu^2 + \ell^2}}, \tag{A.13}$$

have been widely studied in the past (see [69]). Now, we provide a very brief review of this theory following reference [70]: in short, there are two linearly independent functions f_ℓ and g_ℓ that satisfy recurrence (A.12). The function f_ℓ is defined as the *minimal solution* to the equation (A.12) if

$$\lim_{\ell\to\infty} \frac{f_\ell}{g_\ell} = 0. \tag{A.14}$$

If f_ℓ is the minimal solution then it is unique and all the other solutions (linear combinations of f_ℓ and g_ℓ) are called *dominant solutions*. In general, for some values of the function argument, the minimal solution decays too fast in the forward direction[23], or the dominant solutions present an exponential grow in ℓ. In such a case, the forward recurrence converges to the linearly independent dominant solution g_ℓ. However, this means that, in the backward direction, the dominant solution exponentially decays. Thus, in regions where forward recurrence does not output f_ℓ, we can use backward recurrence to obtain a sequence $f_{\ell_{\text{max}}}$, $f_{\ell_{\text{max}}-1}$, $f_{\ell_{\text{max}}-2}$, ... In this scenario, the only problem is finding $f_{\ell_{\text{max}}}$ and $f_{\ell_{\text{max}}-1}$.

The hyperspherical Bessel function is the minimal solution to the equation (A.12) [68]. For $\chi > \chi_{\text{tp}}$, $\chi_{\text{tp}} \equiv \sinh^{-1}(\sqrt{\ell(\ell+1)/|\nu|})$, where tp refers to "turning-point", forward recursion is stable. In regions $\chi < \chi_{\text{tp}}$, the forward recurrence is unstable, so we must employ backward recurrence for these values of χ. Figure 25 shows the hyperspherical Bessel function for several values of ℓ in the two regions. Note how it exponentially falls outside the stability region of the forward recurrence.

Implementing the forward recurrence is straightforward. We simply compute Φ_0^ν and use the recurrence relation to obtain higher multipoles. Background recurrence is more complex. The algorithm provided in [68] offers an efficient method to compute the hyperspherical Bessel function and its first derivative through backward recurrence. We will present the details here.

In principle, we could use the series expression for the Legendre function to obtain $\Phi_{\ell_{\text{max}}}^\nu$ and $\Phi_{\ell_{\text{max}}-1}^\nu$, starting the backward recurrence. However, we will show that we can obtain $\kappa\Phi_{\ell_{\text{max}}}^\nu$ and $\kappa\Phi_{\ell_{\text{max}+1}}^\nu$, where κ is a complex multiplicative constant, from a continued fraction, which numerically converges faster than series. Dividing equation (A.8) by Φ_ℓ^ν leads to

$$\frac{1}{\Phi_\ell^\nu}\frac{\mathrm{d}\Phi_\ell^\nu}{\mathrm{d}\chi} = \ell\coth\chi - \sqrt{\nu^2 + (l+1)^2}\,\frac{\Phi_{\ell+1}^\nu}{\Phi_\ell^\nu}. \tag{A.15}$$

---

[23] Forward recurrences are recurrences where higher ℓ is obtained in terms of lower ℓ, that is, we use Φ_0^ν to compute Φ_1^ν, Φ_2^ν, Φ_3^ν, ..., $\Phi_{\ell_{\text{max}}}^\nu$. Backward recurrences are the opposite, that is, we use $\Phi_{\ell_{\text{max}}}^\nu$ and $\Phi_{\ell_{\text{max}}-1}^\nu$ to calculate all the lower ℓ, $\Phi_{\ell_{\text{max}}-2}^\nu$, $\Phi_{\ell_{\text{max}}-3}^\nu$, ..., Φ_1^ν.

From equation (A.7) and (A.12),

$$\frac{\Phi^\nu_{\ell+1}}{\Phi^\nu_\ell} = a_\ell + b_\ell \frac{\Phi^\nu_{\ell-1}}{\Phi^\nu_\ell} \Rightarrow \frac{\Phi^\nu_\ell}{\Phi^\nu_{\ell-1}} = \frac{b_\ell}{\frac{\Phi^\nu_{\ell+1}}{\Phi^\nu_\ell} - a_\ell}, \tag{A.16}$$

but

$$\frac{\Phi^\nu_\ell}{\Phi^\nu_{\ell-1}} = \frac{b_\ell}{\frac{b_{\ell+1}}{\frac{\Phi^\nu_{\ell+2}}{\Phi^\nu_{\ell+1}} - a_{\ell+1}} - a_\ell} = \frac{b_\ell}{\frac{b_{\ell+1}}{\frac{b_{\ell+2}}{\frac{b_{\ell+3}}{\cdots - a_{\ell+3}} - a_{\ell+2}} - a_{\ell+1}} - a_\ell}. \tag{A.17}$$

Hence, the ratio $\Phi^\nu_\ell/\Phi^\nu_{\ell-1}$ is a continued fraction. Following the usual notation for continued fractions [71], we write

$$\frac{\Phi^\nu_\ell}{\Phi^\nu_{\ell-1}} = \mathop{\mathbf{K}}_{m=0}^{\infty} \frac{b_{\ell+m}}{-a_{\ell+m}} \equiv \frac{b_\ell}{\frac{b_{\ell+1}}{\frac{b_{\ell+2}}{\frac{b_{\ell+3}}{\cdots - a_{\ell+3}} - a_{\ell+2}} - a_{\ell+1}} - a_\ell}. \tag{A.18}$$

Equation (A.15) thus become

$$\frac{1}{\Phi^\nu_\ell}\frac{\mathrm{d}\Phi^\nu_\ell}{\mathrm{d}\chi} = \ell \coth\chi - \sqrt{\nu^2 + (l+1)^2} \mathop{\mathbf{K}}_{m=0}^{\infty} \frac{b_{\ell+m}}{-a_{\ell+m}}. \tag{A.19}$$

The left side of the equation above can be computed with Lentz's modified algorithm. See [70] for details. Computing this ratio for ℓ_{max}, the highest multipole we are interested in the Line-of-sight integral, we get

$$\frac{1}{\Phi^\nu_{\ell_{\text{max}}}}\frac{\mathrm{d}\Phi^\nu_{\ell_{\text{max}}}}{\mathrm{d}\chi} = C, \tag{A.20}$$

where C is the output from Lentz's algorithm. Although Lentz's algorithm does not provide the value of $\Phi^\nu_{\ell_{\text{max}}}$, it provides its sign. This is because the output of Lentz's algorithm is actually of the form A/B, with known A and B. Upon convergence, the signs of Real(B) and Imag(B) are the same as Real$(\Phi^\nu_{\ell_{\text{max}}})$ and Imag$(\Phi^\nu_{\ell_{\text{max}}})$, but we stress that $B \neq \Phi^\nu_{\ell_{\text{max}}}$. We can use this information plus (equation (A.15))

$$\Phi^\nu_{\ell_{\text{max}}+1} = \Phi^\nu_{\ell_{\text{max}}}(\ell \coth\chi + C) \tag{A.21}$$

to start the backward recurrence. Since we do not know the value of $\Phi^\nu_{\ell_{\text{max}}}$, we follow the recurrence of $y_{\ell_{\text{max}}} = \kappa\Phi^\nu_{\ell_{\text{max}}} = \text{sign}(\text{Real}(\Phi^\nu_{\ell_{\text{max}}})) + i \times \text{sign}(\text{Imag}(\Phi^\nu_{\ell_{\text{max}}}))$. All the function's values from ℓ_{max} to 0 will be obtained up to a multiplicative factor κ. Finally, we can compare y_0 with the analytic expression of Φ^ν_0 to find the constant κ. With the values of the hyperspherical Bessel function, the values of its derivative and second derivative are easy to get using equations (A.8) and (A.9).

This algorithm is implemented in `CLASS`. In `AniCLASS`, we simply modified it to include complex numbers. In the module `hybess.pyx`, we implemented it in `Cython`. Figure 8 shows the radial function ${}_2\epsilon_\ell^{(2,2)}$ for several values of ℓ and χ compute using `hybess.pyx`. Figure 26 shows the relative error between the implementation we employ, using recurrence methods with complex numbers, and the results from the arbitrary precision `Python` library `MPmath`[24].

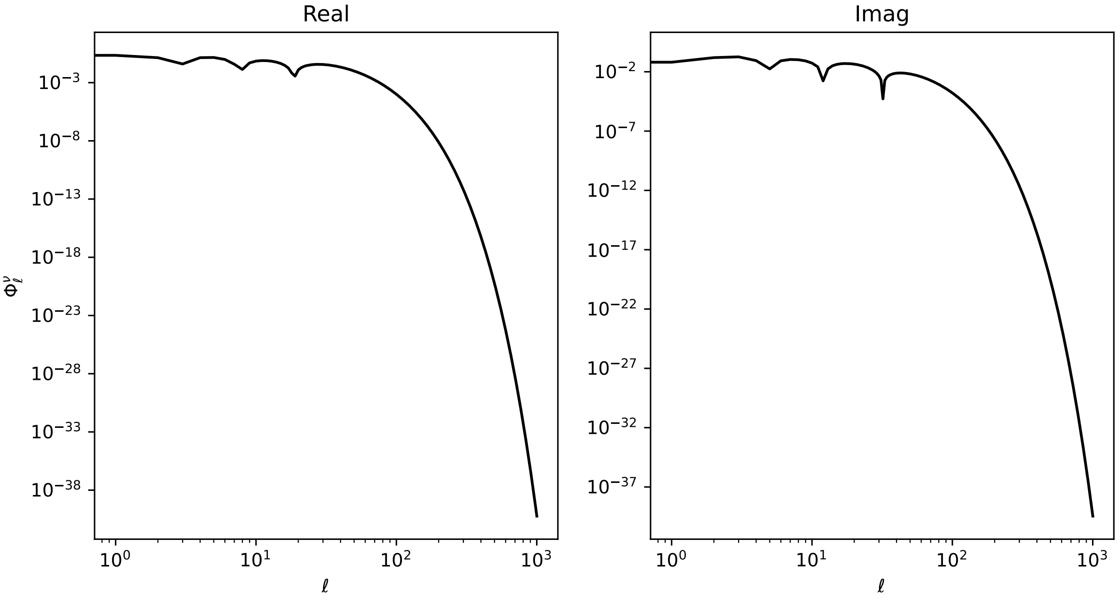

(a) Hyperpherical Bessel function at $\chi = \chi_{\rm tp}/2$ for several values of ℓ. Note the exponential decay.

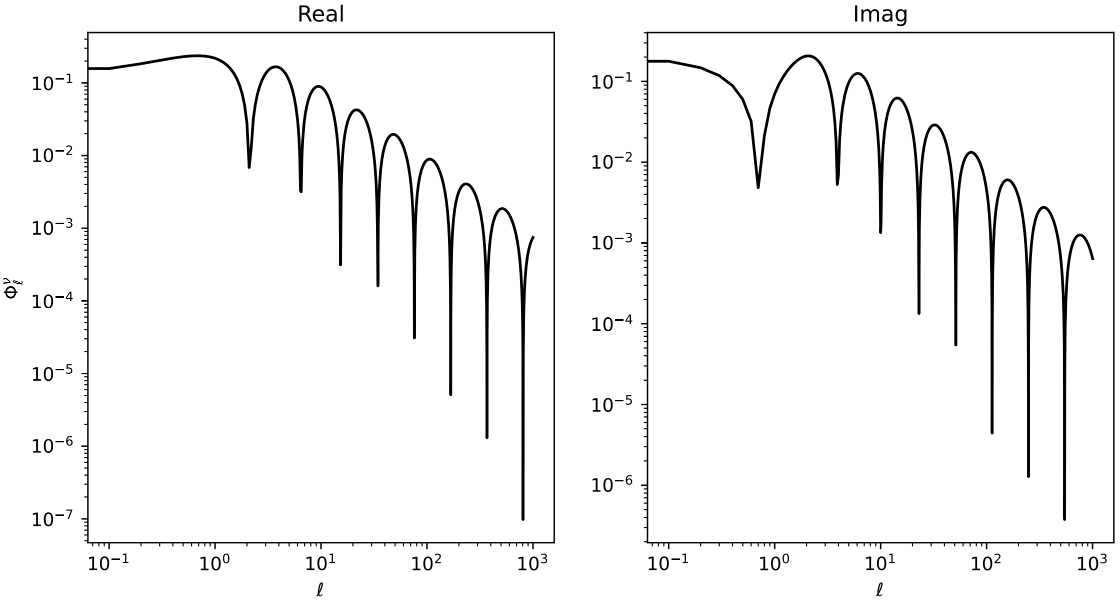

(b) Hyperpherical Bessel function at $\chi = 2\chi_{\rm tp}$ for several values of ℓ.

Figure 25: Hyperspherical Bessel functions inside and outside the forward recurrence stability region. Parameters are $\nu = 4 + i$ such that $\chi_{\rm tp} \approx 6.18$.

---

[24] `https://mpmath.org/`.

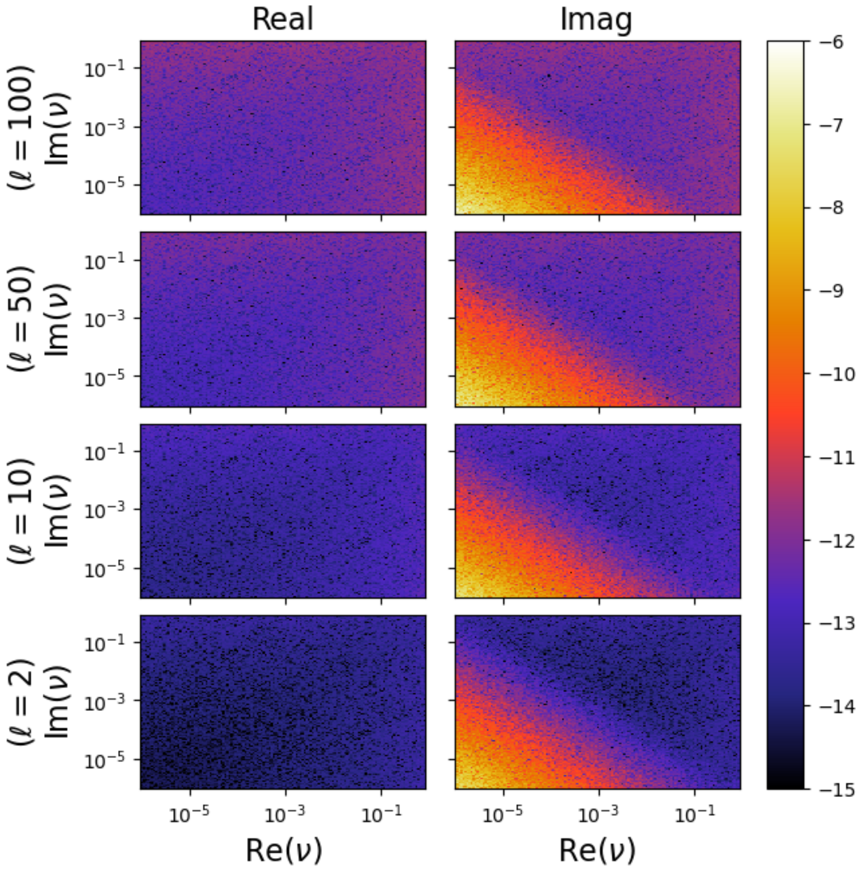

Figure 26: Relative error between hyperspherical Bessel functions calculated using the algorithm based on recurrence relations and `mpmath`. In this plot, $\chi = \chi_{\text{tp}}/100$; note that χ_{tp} depends on ℓ and ν. This is a reproduction of the figures in [68].